Universal Control and Management Strategies for Micro-Grid-Based Smart Grids Using Synchronous Converters

by

Seyed Mahdi Ashabani

A thesis submitted in partial fulfillment of the requirements for the degree of

Doctor of Philosophy
in

Power Engineering and Power Electronics

Department of Electrical and Computer Engineering
University of Alberta

Abstract

The energy sector is moving into the era of distributed generation (DG) and micro-grids (MGs). This research focuses on development of a new family of control and management strategies for integration of micro-grids with numerous voltage source converters and synchronous generators in smart power grids by introducing the new concepts of Synchronous Converters and Synchronous-VSC. The stability and operation aspects of converter-dominated MGs are faced by many challenges. Important among these are: 1) the absence of physical inertia; 2) power quality issues due to permanent frequency offset and voltage and current regulation; 3) mutual interactions among synchronous generators and voltage source converters; 4) transitions to islanding and its detection delays; 5) large sudden disturbances associated with grid restoration, transition to islanding and DG out-of-phase re-closing; and 6) development of high impedance weak MGs because of installation of renewable energy resources in areas which are geographically remote from the load centers.

This dissertation presents a new family of comprehensive control and management strategies for MGs in smart distribution grids. The thesis also provides a general and computationally-efficient framework for the modeling and analysis of the management strategies in a multiple-DG MGs; the framework facilities MG dynamic studies and controller parameters in large micro-grids with multiple DG units. Three different approaches for real and reactive power management are proposed. The controllers offer the following advantages: 1) the proposed topologies can be applied to both voltage-controlled (VC) and current controlled (CC) voltage source converters (VSCs). 2) The controllers are universal and realize requirements of both grid-connected and islanded modes, i.e. share real and reactive power during islanding and act as grid supporting VSCs in grid connected mode. 3) The controller emulates the behaviour of conventional synchronous generators (SGs) which in turn results in better integration of electronically-interfaced DG units into the power system and prevents instabilities due to interaction of fast response DGs and SGs. 4) The controllers realize

seamless and robust transition to islanding mode. 5) The controllers are equipped with a nonlinear supplementary controller to mitigate large power angle swings associated with large-signal disturbances. 6) The controllers can be easily adapted to conventional synchronous machines. 7) The controller provides seamless self-synchronization operation under out-of-phase reclosing. 8) The controllers provide stable operation and superior current decoupling in very weak grids and MGs.

Preface

This thesis is an original work by Mahdi Ashabani. The research project, of which this thesis is a part, received research ethics approval from the University of Alberta Research Ethics Board, Project Name "Universal Control and Management Strategies for Micro-Grids in Smart Grids Using Synchronous Converters".

Chapter 2 of this thesis has been published as M. Ashabani and Y. A. –R. I. Mohamed, "New family of microgrid control and management strategies in smart distributed grids- analysis, comparison and testing," accepted for publication in IEEE Trans. Power Syst., 2014. I was responsible for the idea development, analysis and data collection as well as the manuscript composition. Dr. Mohamed assisted with analysis and contributed to manuscript edits.

Chapter 3 of this thesis has been published as M. Ashabani and Y. A. –R. I. Mohamed, "Novel comprehensive control framework for incorporating VSCs to smart power grids using bidirectional synchronous VSC," *IEEE Trans. Power Sys*., vol. 29, no. 2, pp. 943-957, March 2014. I was responsible for the idea, development, analysis and data collection as well as the manuscript composition. Dr. Mohamed assisted with analysis and contributed to manuscript edits.

Chapter 4 of this thesis has been published as S. M. Ashabani and Y. A. –R. Mohamed, "General interface for power management of micro-grids using cooperative droop control," *IEEE Trans. Power Syst*., vol. 28, no. 3, pp. 2929-2941, Aug. 2013. I was responsible for the idea, development, analysis and data collection as well as the manuscript composition. Dr. Mohamed assisted with analysis and simulation and contributed to manuscript edits.

Chapter 5 of this thesis has been published as S. M. Ashabani and Y. A. -R. I. Mohamed, "A flexible control strategy for grid-connected and islanded microgrids with enhanced stability using nonlinear microgrid stabilizer," *IEEE Trans. Smart Grid*, vol. 3, no. 3, pp. 1291-1301, Sep. 2012. I was responsible for the development, analysis and data collection as well as the manuscript composition. Dr. Mohamed assisted with analysis and simulation and contributed to manuscript edits.

Chapter 6 of this thesis has been published as M. Ashabani and Y. A. –R. I. Mohamed, "Integrating VSCs to weak grids by nonlinear power damping controller with self-synchronization capability," *IEEE Trans. Power Syst*., vol. 29, no. 2, pp. 805-814, March, 2014. I was responsible for the development, analysis and data collection as well as the manuscript composition. Dr. Mohamed assisted with analysis and simulation and contributed to manuscript edits.

Acknowledgements

First and foremost I would like to express my wholehearted gratitude to Allah, the Almighty, for enlightening my path and guiding me through each and every success I have or may reach.

My long tenure in the fields of smart grids, control and power electronics have been enriched by the help of many people. Here I would like to take this opportunity to thank the people who have in no small way made the research in this thesis possible.

I owe my deepest gratitude to Dr. Yasser Abdel-Rady I. Mohamed guidance, support and encouragement. I am forever indebted to my advisor for shaping my academic life. I have profoundly enjoyed from my collaboration with him. His enthusiasm for pursuing serious problems in power engineering at the highest levels of integrity has been a consistent origin of inspiration and guidance throughout my study. I would like to thank him for the extensive freedom he offered to explore my intellectual curiosity in our research, and for fostering my capacity critically as an independent researcher. I would like to thank him for motivating me to work on the cutting edge technology of combining control, power electronics and electrical machines theories and presenting a universal control-management strategy.

I would like to express my thanks to the examiners committee for their valued time and interests in my thesis.

Finally, I would like to pay my extreme tribute to my mom and my deceased dad. See Mom, the time you spent helping me paid off. Although my family were thousands of kilometres away when I was working on this thesis, their love and support were always here. I would also like to express my gratitude to my mom, prayers and support from my sister and brothers.

Table of Contents

List of Tables

List of Figures

Nomenclature

$P = P_e$	Real power
$Q = Q_e$	Reactive power
P_{set}	Real power preset
Q_{set}	Reactive power preset
i_{d-set}	d-axis preset current
i_{q-set}	q-axis preset current
E	Voltage amplitude of VSC
V_L	Local load bus voltage amplitude
V_g	Grid voltage amplitude
E_{fb}	Feedback voltage amplitude
$E_{set} = E_{F-ref}$	Voltage reference
E_{nom}	Nominal (rated) voltage
E_0	Voltage drooping preset value
ω	Voltage frequency
ω_0	Frequency drooping preset value
δ_{DG}	DG load angle
δ_L	Local-load-bus voltage angle
δ	DG voltage angle
ω_{set}	Frequency loop preset value
e_d, e_q	d-q voltage components of VSC
e_{abc}	Three-phase voltages of the output filter
v_d, v_q	d-q voltage components of VSC's filter
v_d^*, v_q^*	Controller commands for d-q voltage components
i_d, i_q	d-q current components of VSC
i_d^*, i_q^*	Controller commands of d-q current components
m	Frequency vs. power drooping slope
$n = K_q$	Voltage drooping slope
R_F	DG connecting filter resistance
X_F	DG connecting filter reactance
K_v	Reactive power vs. voltage slope constant
X_L	Line reactance
R_L	Line resistance
X	Total connecting reactance
R	Total connecting resistance
K_d	Power vs. angle slope constant
K_f	Power vs. frequency slope constant
K_e	Voltage regulation loop integrator gain

N	The number of units in an MG
Z_L	Total reflected local load impedance
G_{ij}	Conductance between DGs *i* and *j*
B_{ij}	Suseptance between DGs *i* and *j*
P_{SG}^{*}	Power set-point of synchronous generator droop characteristic
P^{*}	Power set-point of VSC droop characteristic
δ_{set}	Set angle in droop control
R_T	Transformer resistance
X_T	Transformer reactance
Z_T	Transformer impedance
R_L	Line resistance
X_L	Line reactance
$\omega = \omega_v$	VSC frequency
ω_{rotor}	Synchronous generator rotor speed
ω_L	Local load bus frequency
ω_{set}	Set frequency (rated frequency)
ω_0	Set frequency of droop control
ω_v	Cut-off frequency of the voltage loop low-pass filter
d	Angle versus real power slope constant
K_f	Power-frequency characteristics slope
K_d	Power-angle characteristics slope
K_p	Power loop integrator gain
k_i	The nonlinear control law gains , $k_i > 0$
J	Rotor momentum of inertia
$\Delta\omega_{\max}$	Maximum acceptable frequency drop
$\Delta E_{\max}$	Maximum acceptable voltage drop
$\Delta i_{q-\max}$	Maximum acceptable q-axis current drop
P_{damp}	Damping power
P_{synch}	Synchronizing power
γ	System augmented uncertainty
$\hat{\gamma}$	Estimation of system uncertainty
ρ	Adaptation law gain
u	Control input
u_f	Mapped control input
P_{prim}	Primary source reference power command
P_m	Input mechanical power of synchronous generator
τ_p	Primary source time constant
$\theta_r = \theta_{rotor}$	Rotor angle of a synchronous generator
$\omega_r = \omega_{rotor}$	Rotor speed of a synchronous generator

$T = T_e$	Virtual torque
T_{avg}	Average virtual torque
ψ_{ds}	d-axis flux component of a synchronous generator
ψ_{qs}	q-axis flux component of a synchronous generator
W_{SM}	Stored energy in the synchronous generator
W_C	Stored energy in a dc-link capacitor
S_{SM}	Rated power capacity of a synchronous generator
S_{VSC}	Rated power capacity of a VSC
H	Inertia constant
H_{VSC}	Equivalent emulated inertia of a VSC
P_m	Input mechanical power to a generator
P_{load}	Load power
P_{in}	Input power
P_{source}	Output source power
V_{DC}	DC-link voltage
ΔV_{DC}	Maximum dc-link voltage deviation
V_{DC-avg}	Average dc-link voltage
Δf	Maximum frequency deviation
ω_s	Switching frequency
ω_n	Controller bandwidth of synchronous-VSC
ξ	Damping ratio
τ_v	Low-pass filter time constant
T_i	Integrator time-constant
ω_v	Voltage frequency
ψ_f	Virtual rotor flux
θ	Voltage angle
ϑ	Power angle of the overall reflected load
ω_i	Current frequency
α	Power angle
φ	Current angle
i	Amplitude of phase current
S_{SC}	Short circuit capacity of grid
E_{F-ref}	Filter voltage command

Acronyms

AC	Alternating Current
DC	Direct Current
HVDC	High Voltage Direct Current
IGBT	Insulated Gate Bipolar Transistor
PWM	Pulse Width Modulation
PLL	Phase-Locking Loop
VSC	Voltage Source Converter
PV	Photovoltaic
SG	Synchronous Generator
SM	Synchronous Machine
PI	Proportional Integral
SISO	Single Input Single Output
DG	Distributed Generation
MG	Microgrid
CC	Current Controlled
VC	Voltage Controlled
EI	Electronically-Interfaced
CI	Communication Infrastructure
PQ	Constant Real Power Constant Reactive Power Bus
PV	Constant Real Power Constant Voltage Bus
AB	Adaptive Back-stepping
EMF	Electro Magnetive Force
ST	Smart Transformer
NDZ	Non-Detection Zones
SCR	Short Circuit Ratio

Chapter 1 Introduction

1.1 Forward

Due to fast development of renewable energy resources the distributed generation (DG) concept has changed the paradigm of energy generation and transfer under the smart grid vision [1]-[3]. DG has many advantages such as closeness to customers, increased efficiency and reduced transmission loss, better reliability, and improved energy management [4]–[8]. The majority of DG resources are interfaced to grid/loads via power electronic converters. A cluster of DG units, loads and energy storage devices connected in series or parallel together form a microgrid (MG) [2] which can operate in three modes of operation, namely1) grid connected mode, 2) the islanded mode and 3) transition between the two modes [2]. Fig. 1.1 shows a typical MG. Based on IEEE Standard 1547.4-2011 [9], an effective approach to control and manage smart distribution grids is to divide them into a set of MGs. The IEEE 1547 recommends that MGs should be disconnected from the main grid when the grid voltage is lower than 0.85 p.u. or higher than 1.1 p.u. to prevent islanding operation [9]. The concept of MG has been expanded to overcome the common interconnection issues resulted from individual DGs in the conventional power system. The main benefits of MGs are better customer satisfaction, local reliability improvement, enhanced voltage profile and increased efficiency due to loss minimization.

One approach to control and manage a smart power system is to split it to several MGs as shown in Fig. 1.2. These MGs act like some power islands connected to each other to form the total smart power system. MGs can be connected to the grid or work in autonomous mode. In each case, the adopted controller-management strategy is different and affects system behavior in terms of its stability, performance and power quality. In islanding mode, DGs must supply local loads power and provide satisfactory frequency and voltage stability and quality. This approach eases hierarchical control and management of smart grids by coordination of MGs such that smart grid management objectives are

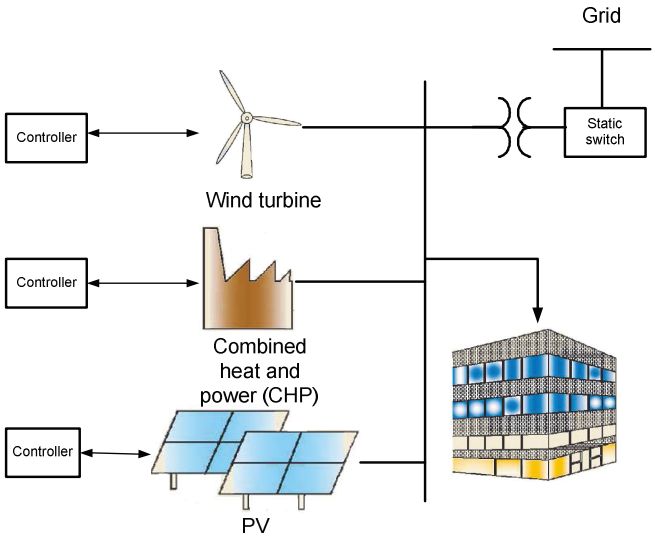

Figure 1-1. A schematic view of a typical MG.

achieved. Also, when a fault occurs in the transmission system, adjacent MGs can be decoupled from the fault location to prevent propagation of instability thorough the adjacent MGs. It also enables development of small power units in various geographical areas and connecting to the utility grid after they are expanded enough. It is also beneficial to eliminate communication infrastructure (CI) in some lower levels of the smart to improve system reliability. The general sequential control and management of an MG-based smart grid is summarized as follows:

- Superior management and policies of the whole smart grid based on economical and operational constraints of energy management of the total smart power system.
- MG/area level control involving coordination and management of MGs and areas to realize enterprise manager requirements. Simply speaking, based on enterprise level policies, long and short term condition of renewable energy resources and load demand, the power set points of each MG/area is adjusted.
- Unit level involves control of individual generation units within an MG including conventional SGs and EI-DGs within MGs. These units are responsible to supply local load demands during islanding and during grid connection they inject the preset active and reactive powers to the utility grid.

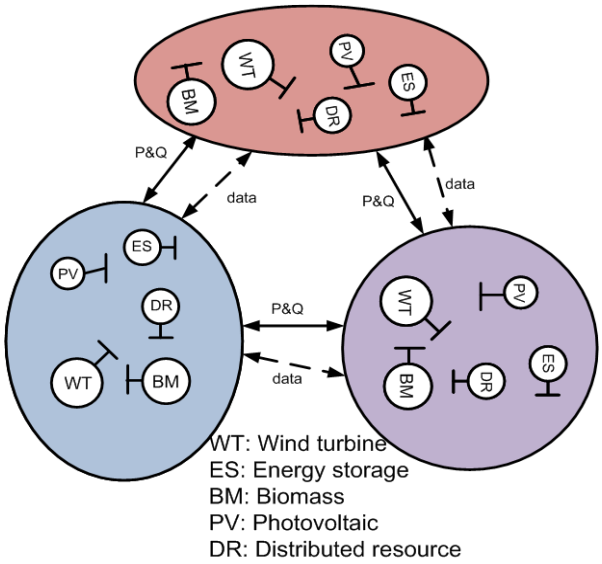

Figure 1-2. Construction of a smart grid by coordination of individual MGs.

Each level supervises and coordinates the lower level systems and the stability and satisfactory performance of each level is influenced by upper level controllers. For an islanded MG, frequency and voltage droop control is widely adopted to share active and reactive powers among units proportionally and eliminate CI and as a matter of fact the droop control is a method for coordination of DGs.

By optimal coordination and management of MGs, superior management strategy of the smart grid can be realized. Instabilities due to interaction among various electronically-interfaced (EI) DG units, synchronous generators and the grid, steady state constant frequency operation, accurate load sharing, smooth switching between modes and robustness against parameter variations are main concerns of MG operation. The stability issues related to MG operation are mainly because of lack of dominant energy resource in autonomous mode, different response time constants of EI-DG and conventional generators due to lack of inertia for frequency dynamics in EI-DG which may lead to angle/voltage instability [10] and instabilities due to change of mode of operation.

The main goal of a grid-connected MG is to supply real and reactive powers under high power quality injection constraints. In the islanded mode, DG units are required to supply “regulated power” under controllable voltage and frequency

while maintaining accurate power sharing among different DG units [2], [5]. Driven by these requirements two main control strategies- namely communication based centralized [10]-[14], and decentralized [5], [15]-[28] have been proposed in the literature. Between these two methods, due to reliability issues, the droop-based decentralized controller has been widely adopted for power sharing and control of MGs.

The dominant control method for a grid-connected DG interface is based on a current-controlled voltage source converter (CC-VSC), to inject the required real and reactive powers via current control [12], [29]. However, when the MG works in the islanding mode, the absence of a stiff grid to regulate voltage may lead to voltage and frequency distortion [12], [29] or even instability with this control method. Therefore, DG needs to switch to voltage controlled mode and so an islanding detection technique is required. Furthermore, this transition to islanding mode may result in very severe transients in power, frequency and angle, and instability is expected. One approach is to shed loads intelligently to damp power oscillations subsequent to islanding [30]. Katiraei studied system behaviour after islanding and used a control reconfiguration to stabilize the system [31]. Robust control of DG units subsequent to islanding is also proposed in [32]. Some methods for smooth transition to islanding mode are investigated in [10, 33]. A hierarchical control for seamless transition to islanding is proposed in [34]. However, all these methods need islanding detection; a delay in this process makes system unstable. Moreover, almost all grid-connected VSCs need a phase-locked loop to detect voltage phase angle for synchronization with the grid voltage during start-up and grid restoration. Thus, in situations that the connecting line of a DG is long, communication infrastructure (CI) is unavoidable. Even the dynamic of the PLL may deteriorate performance of the VSC in transients [35], [36].

Grid connected converters are categorized as three main groups, namely, grid-forming, grid feeding and grid-supporting VSCs [37]. Grid forming VSCs act like ac voltage sources to generate the voltage reference with low equivalent output impedance. There are serious drawbacks related to the grid forming VSCs such as

lack of inherent current limitation, considerable coupling between real and reactive powers, and poor synchronization process with the grid due to low output impedance [37]; thus, they are usually not good candidates for grid-connected mode. Grid-feeding VSCs inject the d- and q-axis preset currents and shows current source behaviour with high parallel impedance. Since, grid-connected DG units are usually required to supply their preset currents and the grid feeding VSCs operate well in parallel with other grid-feeding converters most of grid-connected VSCs are of this type. However, since the grid-feeding strategy causes voltage and frequency distortion and even instability [29], it is not an acceptable choice for islanding operation. An alternative is to use hybrid CC-VSC and VC-VSC by switching between these two strategies subsequent to change of mode of operation. Nevertheless, it is essential to embed fast and accurate islanding detection techniques to guarantee smooth mode transition. Grid-supporting VSCs are controlled as either voltage source or current source converters; the only difference is that in the first the voltage reference and in the latter current reference are adjusted by an outer drooping characteristics, therefore they can participate in grid voltage and frequency regulation.

Since considerable portion of renewable energy resources, such as wind turbines, photovoltaic (PV), fuel cells and energy storage systems and many modern loads such as communication technology facilities, data centers and motor drives are dc type, dynamics and controls of rectifiers and dc MGs are gaining high interest [38]. However, in dc grids, many generation units such as wind turbines must be interfaced to the utility grid via electronically-interfaced (EI) rectifiers. Besides, several modern ac loads are coupled to the ac grid through back-to-back rectifier-inverter to provide variable frequency operation. Based on predictions given in [39], the resistive load share will be significantly reduced whereas the EI loads share will increase to 60%-80% of the total load by year 2015.

Conventional droop controls suffer from some serious drawbacks. Important among them are poor frequency and voltage regulation due to their permanent offset, inaccurate power sharing, low stability margin, dependency on line

impedance and slow dynamic response [5]. As an alternative, since in fact real power is proportional to the load angle it is also possible to use the load angle as the drooping variable [28][40-41] to fulfill constant-frequency operation. Hierarchical control strategy is also available to compensate frequency variation via a secondary level [42]. Furthermore, in the conventional current-controlled VSCs and also droop methods it is assumed that the connecting line is mainly inductive and the load angle is considered to be small. In these scenarios, the real power and reactive powers are independent and the first is controllable through the load angle whereas the latter is adjusted by the voltage amplitude. However, the operation is further complicated when considering weak grids, where load angle is large, and also resistive lines, such as directly-coupled VSCs [43]. In these cases, traditional control strategies fall short to guarantee system satisfactory performance and decoupled control. Toward this, virtual impedance is the most adopted approach [44] to fulfill a mainly resistive or inductive line. Nevertheless, it drastically degrades system performance and voltage regulation. The concepts of virtual power [45] and virtual frequency [43] have been addressed in the literature for better decoupling. The first, suffers from inaccurate power sharing and the latter needs complex mapping.

One of the major challenges facing future power systems is significant reduction in grid equivalent rotational inertia due to the expected high penetration level of EI units; which in turn may lead to frequency-stability degradation. To overcome this difficulty, controlling VSCs as virtual synchronous machines is proposed for power system frequency stabilization [46] by embedding a short-term energy storage to the VSC facilitating power flow to and from to the energy storage device proportional to the variation in grid frequency. Usually, the virtual inertia refers to a short-term energy storage which is added to a VSC [46]–[48]. In [49], the virtual inertia is emulated by proper dc-link control. In [50], the idea of '*synchronverter*' was addressed to emulate the mechanical behaviour of a synchronous generator (SG) in the inverters. However, the dc-link is considered as an ideal one with infinite energy and the dynamics of dc-link voltage is not considered. Moreover, its application to rectifiers has not been addressed. In [48-49], [51], methods to

emulate virtual inertia in VSCs interfacing wind turbines and HVDC systems, are presented; however, the embedded inertia does not emulate the behaviour of an SG. The analogy between voltage-source inverters and SG-based MGs has also been addressed in [52]-[53]. The aforementioned survey indicates the interest in developing new and improved control algorithms for VSCs to emulate the dynamic behaviour of SGs.

Beside overall low inertia, future power systems and MGs will suffer from interactions between fast responding VSCs and slower SMs which may contribute to angle, frequency and voltage instability [10]. With the expected high penetration level of power converters in future power grids; the system may face severe difficulty in terms of frequency regulation because of lack of rotational inertia in converter-interfaced generators. Another challenge is that frequency dynamics is not known in the conventional control techniques of VSCs (e.g. voltage-oriented control and direct-power control) which makes it difficult to analyze the angle and frequency stability of a system containing several EI units and conventional synchronous machines (SMs) and line-start motors. Therefore, the development of VSCs with well-defined angle, frequency and dc-link voltage characteristics (similar to SMs with extension to dc-link dynamics) are of high interest for future smart power systems with high penetration of VSCs. Moreover, a general control scheme which is suitable for both rectification and inversion modes without reconfiguration is very attractive in power system applications since bidirectional VSCs can work in generative and motoring modes similar to SMs.

Weak MGs are gaining considerable attention in the context of smart grids vision [54-56]. This is due to the fact that increasingly large number of wind turbines and photovoltaic (PV) units are installed in geographic areas, with best wind and solar power resource, which are usually located far from load centers (e.g., offshore wind farms). This is a major concern all over the world and raises serious questions in terms of system stability and regulation. To gauge grid capacity to transfer power, grid ‘strength’ measure is usually used [57]. Strong low-impedance grids have higher power exchange capacity and limited impact on the grid stability. On the contrary, weak interfaces with high impedance have

critical effect on power stability and voltage regulation. Short-circuit-ratio (SCR) is defined as a criterion to show grid strength. Application of VSCs to weak grids is faced by challenging interconnection issues in terms of stability, steady-state performance and power transfer capacity. The main challenging phenomena are as follows; first, the vector control has very limited capability to transfer the rated power in weak grids. For example, in [58], it has been shown that in a weak grid with SCR=1, only 40% of the maximum power capacity of a VSC can be utilized. With significant tuning effort of the vector controller parameters and the PLL, this percentage can be increased to 60% [58]. Second, in weak grids the load angle deeply drifts the system dynamics to the nonlinear region; thus real and reactive powers are highly coupled which in turn causes large steady-state error and poor transient performance and even instability. Third, in weak grids, the phase-locked loop (PLL) has a negative effect on overall system performance and may lead to instability [59].

As an alternative, the concept of power synchronization control proposed in [58-59] is also applicable to enable more power transmission by a VSC by emulating SGs. Basically, SGs do not have any limitations for connection to weak systems, consequently control methods, such as power synchronization which mimic SG's characteristics can effectively enable VSCs integration in very weak grids. However, the developed techniques for weak grid integration are based on linearized models and lack the self-synchronization and plug-and-play ability. Furthermore, islanded operation of DG units can be allowed to enhance service reliability [60]. The frequency drop method causes a permanent frequency offset during islanding. Thus, when self-synchronization control is applied, frequency and angle mismatch between a VSC and grid at the moment of connection may cause severe transients. Another major concern related to VSC operation in weak grids is the lack of physical inertia in conventional VSCs resulting in poor overall frequency and load angle regulation; thus, islanded operation of microgrids with high penetration of VSCs can be prone to frequency instability.

1.2 Problem Definition and Motivation

There are two possibilities to manage a grid connected MG; in the first method, a back to back rectifier-inverter is installed at the PCC and regulates the power transfer between MG [61] and the utility grid according to the command given by level 2. Instead of a back to back inverter a smart transformer (ST) can be used at the PCC to control direction and amount of power flow between the MG and the grid [62].This unit controls the active power exchange between an MG and the utility grid dependent on the state of both networks and other information communicated to the ST. The power transfer between MG and the grid is controlled by change of tap. Hence, the total power generation of each MG is adjusted by its ST and is shared among DG units using power sharing technique. The converter and transformer decouple the MG from the rest of grid. Actually, the common point acts like a variable load whose power varies based on its reference power determined by level 2 and can be either positive or negative load depending whether MG injects or absorbs active and reactive power from the grid. In this scenario, even during grid connection MGs behave like island ones with a variable load connected at its PCC, so adopted techniques for an islanded MG like droop control can be applied during grid connection to share active and reactive powers among DG units. As a result there is no need for change the control strategy subsequent to operational switching and the synchronization with the grid can also be done by the PCC converter. Although this method eliminates the CI in a grid connected MG to adjust set points of DGs, it needs a large power converter at PCC with power capacity of the MG which can be easily overloaded during transients and consequently the reliability of this method is degraded.

Another approach to control and manage a grid connected MG is to eliminate the PCC converter and allocate set points of various DG units using CI within the MG individually via a CI. In other words, after the preset powers of various MGs are determined by MG coordinator at level 2, at level 3 or DG coordinator level, the preset powers of DGs inside the MG are tuned in such a way that finally the desirable power flow between MG and the utility grid or MG power set point is achieved. Whether an MG with a converter at PCC and elimination of CI is more

reliable or an MG with CI and without PCC converter is an open question for future works.

Considering basic features of MG based smart grid like frequent switching between islanded and grid connected mode, the basic requirements of MG operations are summarized as follows:

1) The preset powers of various MGs are allocated by the smart distribution system manager and MGs are required to generate this power.

2) DG units are required to either generate the preset real power and or maintain DG bus voltage constant (PV bus) or generate the pre-specified reactive power (PQ bus).

3) When islanding occurs, transition to islanded mode must be seamless to avoid severe transients in voltage, frequency and power angle.

4) Large signal stability of the MG should be guaranteed even during sudden large contingencies to avoid any poor performance or even instability. The linear controllers are not capable to provide and ensure seamless operation subsequent to severe transients.

5) Subsequent to islanding, DG units must share the total real and reactive power demand according to their power capacities minimize circulating current, and benefit from maximum power capacity of the MG.

6) After fault is cleared in the main grid, the MG must be reconnected to the grid. A synchronization process is necessary to avoid flowing large current and severe overvoltage at the moment of grid connection.

7) System stability and robust performance should be guaranteed in all situations and after large contingencies. This issue is more pronounced in MGs where fast response and lack of inertia for electronically-coupled DG units reduce stability margin of voltage/angle.

8) It is recommended that VSCs mimic dynamic performance of the conventional synchronous generators to minimize their interactions resulting in better integration of VSC based DG units into a power system with high number of SGs.

9) From the power quality perspective, it is important that MG frequency is kept constant in steady state; large frequency drop may deteriorate sensitive loads

operation.

10) Frequent load power variations results in frequency chattering in the conventional droop controllers. The existence of inertia for frequency mitigates this issue.

11) Since many renewable energy resources are located in areas with rich wind and solar power which are far away from the load centers, weak high impedance MGs will be significant part of the future smart power grids, will face challenging issues in terms of stability, power transfer capacity, and high coupling between real and reactive powers.

12) To realize a true plug-and-play MG, it is essential to provide the self-synchronization capability for VSCs enabling autonomous grid restoration subsequent to reclosing without a need for grid information.

13) Coordinated optimal control and power management of buffered MGs in smart grids and DG units within each MG using a multi-objective intelligent power management. In this case, a multi-objective function is defined aiming at minimizing MG and smart grid losses, maximizing large signal stability of the total smart grid including separate MG units, and maximum utilization and penetration of renewable energy resources and energy storage devices.

This project aims at introducing a new family of universal control topologies which can fulfill MG operation requirements in the smart grid environment. The controller structures do not need to be reconfigured subsequent to change mode. This helps to overcome problems such as non-detection zones (NDZ) and islanding detection delays. The system is stable and robust during harsh transients such as transition to islanding and sudden load power changes. It also provides accurate real and reactive power sharing even with impedance mismatches and is robust against controller parameters uncertainties drifts which allows higher frequency and voltage drooping coefficients with better power sharing. The proposed topologies can adopt either voltage controlled or current controlled schemes. Load sharing can be applied using either power or quadrature component currents. The VC-VSC has the advantage of voltage regulation within acceptable limits which is an important factor for an autonomous MG.

Nevertheless, since there is no current loop, current quality may be deteriorated. Therefore, a CC-VSC can be adopted to improve current regulation. The proposed controllers employ cooperative angle-frequency drooping for active power sharing during islanding while the drooping constants act as power damper and synchronizer in the grid connected mode. A nonlinear controller is proposed to enhance the DG stability during severe disturbances and guarantee large signal stability of the MG while the main motivation is the highly-nonlinear behaviour of power sharing dynamics and the wide-band of operating conditions in a typical MG system. The adaptive back-stepping (AB) method is employed to design the nonlinear controller which is one of the most rigorous nonlinear control design tools. The proposed nonlinear controller accounts for nonlinearities of power, frequency and angle.

1.3 The Proposed Control Strategies and Literature Review

VSCs are finding expanded use in various applications in modern power systems ranging from connecting renewable resources, integrating DG units, and high voltage dc (HVDC) transmission systems. However, still the major portion of generation units are the conventional synchronous generators and with the current trends and the expected high-penetration level of VSC-based systems and HVDC serious concerns are raised in terms of renewable energy resources and also interactions between SGs and VSCs and deep penetration of DG. Moreover, the future smart power grids are modeled and managed as interconnection of several MGs; therefore control, management and coordination of MGs are increasingly becoming important. Accordingly, the developing a universal family of controllers-managers for VSCs in MG-based smart grids which can fulfill requirements of both operational modes with plug-and-play capability is of high interest. Also, it is desirable that the controllers behave similar to SGs, thus grid fells them as virtual machines which reduces the analysis and control of smart grids similar to the mature and well-known SG-based power systems and attenuates the impact of such devices on system stability. Among the stability topics, the interactions between VSCs with nearby synchronous generators and

large-signal stability are important research topics. In this section, an overview of the proposed controller-managers strategies and their comparison with the previous works in the literature is presented.

1.3.1 New Family of Control and Management of VSCs in MG-Based Smart Distribution Grids

Several control topologies are developed for switch-mode VSCs. The conventional control topologies for three phase converters are voltage-oriented vector control and direct-power control [63]. Fig. 1.3 shows these two control variants for rectifying and inverting modes. As shown in Fig. 1.3, the dq components of the current vector are regulated by a controller generating appropriate values for the converter dq voltage components. A PLL is required to transform current and voltage variables from the abc frame to the dq frame. It is also feasible to implement the controller in the $\alpha-\beta$ or the abc frame using a proportional-resonant (PR) controller. An alternative control strategy is to use direct power control in which voltage components are adjusted based on real and reactive power errors. None of these methods, however, can directly control the frequency and load angle. Although the vector control technology has reached a high level of maturity, serious questions have been raised about its operability and effective integration into future power grids. These concerns are worldwide and are in terms of their capability to transfer power to the grid, instabilities due to PLL and its interaction with the controller during contingencies and grid synchronization [35], interaction with conventional SGs due to their different characteristics and response speed, instability in weak grids [54-56], low band-width and unknown frequency and angle dynamics. To overcome these difficulties, novel control strategies have been recently developed for control of VSCs in polar coordinates mainly to mimic SGs behaviour in VSCs [35], [50]. Although the '*synchronverter*' strategy proposed in [50], it is just for a grid-connected VSC and its characteristics in islanding have not been investigated. Moreover, the current limitation and regulation, and dc-link dynamics are not

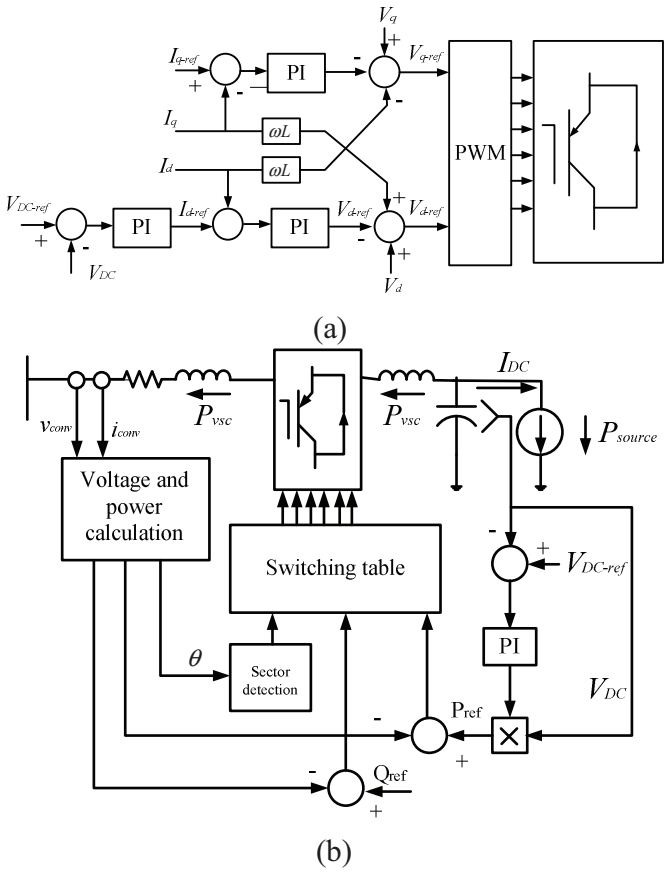

Figure 1-3. Various control topologies for the rectifiers, (a) vector control and (b) direct power control.

taken into account during controller design. The back-EMF generations of SGs are emulated in [64] by redesign of PLL and virtual impedance loop is employed to mimic the SG's equivalent impedance. However, a PLL is necessary during steady state which may deteriorate system stability and does not allow the controller to benefit the self-synchronization ability similar to [35, 50]. The virtual inertia of an SG's rotor and power sharing are simultaneously achieved in [65] by a modified droop control with an adding an extra derivative term to the conventional droop. In [66] the dynamic behaviour of an SG's rotor is emulated by proper dc-link voltage regulation and in fact grid feels the dc-link capacitor as a virtual rotor. One major advantage of control of VSCs similar to SGs is elimination of the PLL during steady state because of existence of damping power which provides self-synchronization ability [35], [50]. Other techniques have been reported in [52-53] to make the conventional vector control react similar to

SGs. Obviously, the converters with SGs characteristics are the keys for the development of future smart grid with high penetration of EI- interfaced DG units and renewable energy resource. Although both vector and polar controllers show some advantages and drawbacks, the question is that how we can exploit the benefits of both in one unified controller.

Many works have been reported in the literature for MG operation in either grid connected or islanded mode. As mentioned earlier, the most adopted approach for power management of an islanded MG is the frequency and voltage drooping to realize accurate real and reactive sharing to deploy the maximum capacity of the DG units and avoid the circulating current among them without communication links. VPD/FQB droop method [67], adjustable load sharing [68], adaptive droop gain [69], virtual frame transformation [21],[70] and virtual output impedance [71-72] are various variants. Feeder-flow strategy has been developed in [24] to enhance power sharing accuracy. Reference [73] introduces a unified control structure appropriate for both operational modes. Robust droop control method has been expressed in [74] to compensate uncertainties in the system and parameters. In all the droop control methods frequency-dependent operation of droop control causes a deviation between the output frequency of the DG and the grid, thus this method, in its original version, can be only applied to an islanded MG [23]. Moreover, the droop control is effective for mainly inductive lines with equal per unit impedances [43]. Therefore, in low-voltage resistive lines poor power sharing is expected.

To eliminate frequency drop the angle droop method has been proposed in [40-41]. However, there are some serious questions regarding this technique. First, it needs a common clock in the MG to synchronize various units which in turn necessitates communication infrastructure [75]. Furthermore, it is not clear how to adjust the angle reference of various units and the practicability of the angle drooping in the grid connected mode has not been addressed. Droop control is considered as part of a more comprehensive framework for power management. In [10] the theory of power management of MGs has been extensively discussed. However, there are some questions about its operation and practicability. First,

since the proposed controller is a current-controlled one and cannot guarantee voltage regulation it is mainly applicable to a grid-connected MG in its primary vision. Also, its performance and operation in both modes have not been clearly addressed. Reference [67] extends the technique of [10] using concept of current sharing but it is still a current-controlled strategy and cannot ensure voltage regulation in the islanded mode which may lead to poor performance and instability [29]. The MG hierarchical management structure was proposed in [23] in which the droop control and inner current regulation loops are implemented in the primary level and frequency and voltage restoration are embedded in the second level. The aforementioned survey, confirms the extensive need for a universal management policy which augments all the requirements in one topology.

This dissertation aims at introducing a new family of universal control topologies which can fulfill most of the MG operational requirements in the smart grid environment by developing the new concept of *synchronous converter*. The proposed new family offers the following advantages: 1) it is a comprehensive and universal family which gives the designer a wide variety of options to select the desirable controllers combination to achieve the required performance. 2) The controllers can operate as current-controlled and voltage-controlled. Moreover, hybrid voltage- and current-source based operation is also possible which is presented for the first time in this thesis. 3) The concept of hybrid vector and polar control is proposed in this thesis which allows exploiting the advantages of both controllers. 4) Both VC-VSC and CC-VSC strategies are available. 5) The controllers are applicable to both modes without a need for controller topology reconfiguration which realize universal controllers and smooth transition to islanding. This helps to overcome problems such as NDZ and islanding detection delays. 6) The controllers provide steady state constant frequency operation during islanding mode. 7) The controllers emulate the behaviour of SGs which enables them to be easily integrated to power systems with conventional SGs without loss of stability and dynamic interference. 8) Drooping variables can be either current dq-components or real and reactive power, thus either power or

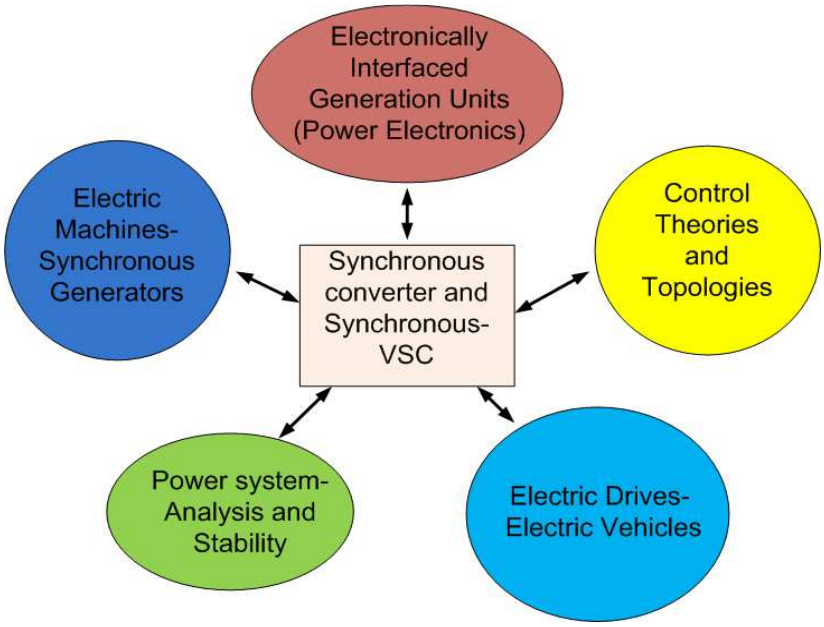

Figure 1-4. Synchronous converter as the intersection of control, electric machines, power electronics and power systems.

current management strategies can be realized. The voltage controlled current-source based strategy augments the current regulation, current limitation and current management in one compact and neat controller. Fig. 1.4 shows the basic concept of *synchronous converter* which is the intersection of control theories, power electronics, power systems analysis, and electric machines. In other words, control theories integrate the power electronics, electric machines and power systems concepts into one unified and universal structure. In this case, numerous VSCs and SGs can be easily integrated to smart grids since they show similar behaviour. This eases power system analysis and significantly improves overall system stability in the presence of EI-interfaced generation and load units.

It is worth comparing *synchronous converter* and *synchronverter* to show the superiorities of synchronous converters. Generally speaking, synchronous converters are comprehensive families of controllers and managers for management of both real and reactive powers and also control and regulation of frequency, voltage and current in a compact structure. The main drawbacks related to *synchronverter* are lack of current regulation and limitation, lack of voltage regulation and control, simple structure and low degree of freedom to

choice controller parameters, and permanent frequency offset. Moreover, the authors didn't discuss its performance in islanding mode, therefore its behaviour and characteristics in islanding is unknown. Also, in the grid connected mode it cannot realize either a constant voltage bus or a constant reactive bus. The stability and small signal analysis were not addressed. The controller is only implemented in polar coordinate, so control and decoupling of d- and q-axis currents are missed. Despite, generally speaking, synchronous converters are comprehensive families of controllers and managers for management of both real and reactive powers and also control and regulation of frequency, voltage and current in a compact structure. As discussed earlier, it is emphasised that they are applicable to both operational modes without reconfiguration with emulated behaviour of SGs. Both current-source and power-source based operation and also power drooping and current drooping are available. The controller inherently provides current and voltage regulation and limitation and can generate either voltage or reactive power reference. No permanent frequency drop occurs and because of existence of an extra power damping (angle) loop, stability is improved.

1.3.2 Bidirectional Synchronous-VSC Control Strategy for Incorporating VSCs to Smart Power Grids

Instabilities due to dc-link dynamics are one of major sources of instabilities in VSCs [76]. Most of previous works on virtual SGs and/or self-synchronization of VSCs consider the dc-link as an ideal battery with infinite energy [15]-[50]. However, it is obvious that this is not the case and in most of transient scenarios, dc-link voltage varies; also its energy and power are limited. Moreover, if dc-link voltage dynamics is slow and the voltage passes some thresholds for a relatively long time, under- or over-modulation and consequently voltage instability is expected [29]. To improve dc-link voltage stability, fast response short-term energy storage can be installed in DG units [48].

To overcome aforementioned difficulties, in this thesis, a comprehensive control strategy is proposed for VSCs. It augments all the aforementioned requirements in one compact topology which has the following salient features. 1) It emulates the behaviour of SMs with proper adjustment of the dc-link voltage so the power grid views the VSC dc-link as a virtual rotor. Thus, it can be easily integrated to grids with numerous SMs; 2) it introduces some inertia for the frequency, therefore the stored energy in the dc-link can be used for frequency regulation during contingencies which is the same role of SM's rotor; 3) Since it provides bidirectional power transfer, even active loads can be used as an asset for frequency stabilization [77]. Therefore, the proposed topology can be an interesting choice for multi-terminal dc networks [78]-[79]; 4) since the controller has cascaded frequency, angle and dc-link voltage loops, it offers extra damping and synchronizing powers, therefore, it can automatically synchronize itself with the main grid; offer self-synchronization capability; and eliminate the need for a PLL; 5) since dynamics of the dc-link voltage is inherently taken into account during design and analysis, it presents a more practical control topology and design process. In [80], a simple control strategy for dc-link voltage regulation in frequency domain and polar coordinates has been proposed; however, it lacks a comprehensive and general framework for emulating and integrating SM characteristics in VSCs. This thesis presents a comprehensive framework for design of VSCs controllers with SMs behaviour while the dc-link acts like a virtual rotor; 6) it offers well-defined dynamics for frequency, angle and dc-link voltage, which in turn makes power system analysis easier; 7) similar to SMs, it has a fault-ride-through capability.

Two different topologies, namely virtual torque and direct dc-link voltage control strategies are developed for the frequency control loop. In these topologies, the output power and the dc-link voltage are used as control variables, respectively. It will be shown that the direct dc-link voltage control presents very good performance with a simple control structure; however, the virtual torque control offers more degrees of freedom to select design parameters because there is an extra power loop. For the voltage control loop, two variants are addressed to

realize either a P-Q bus or P-V bus operation. A theoretical analysis, simulation and experimental results are presented to verify the validity and effectiveness of the proposed control strategy.

1.3.3 Enhanced Stability Operation of Microgrids Using Nonlinear Micro-Grid Stabilizer

Although, the droop based decentralized controller eliminates the need for communication infrastructure, its stability especially during sudden large transients such as islanding, grid restoration and load power variations is of high concern [5] ,[18], [81]. It is shown by small signal analysis in [5] that in a droop-controlled DG, power changes may result in instability. Furthermore, the conventional linear controllers and small signal analysis reported previously only deal with small variations around the operating point or base load; this refers to small signal stability because it just deals with stability at one specific operating point when small perturbations appear in the system. However, in an MG system with comparable sizes of DG units and because of the absence of physical inertia due to high penetration level of converter-based DG units, an MG system will be subjected to large transients and power angle swings. Typical large-signal disturbances in an MG system include transition between grid connected and islanding modes, and sudden large load demands. In these situations, linear controllers are not sufficient to guarantee MG stability at different operating conditions; and accordingly, instabilities due to severe transients are expected. On the other hand, nonlinear controller with global stability can be designed to guarantee stable and robust operation at different operating conditions.

The *synchronverter* [50] is adopted in chapter 5 to enhance the DG stability during severe disturbances and guarantee large signal stability of the microgrid while the main motivation is the highly-nonlinear behaviour of power sharing dynamics and the wide-band of operating conditions in a typical MG system. The adaptive back-stepping method is employed to design the nonlinear controller which is one of the most rigorous nonlinear control design tools [82]-[86]. The proposed nonlinear controller accounts for nonlinearities of power, frequency and

angle of VSCs in a power converter system while most of previous researches focused on nonlinearities of current and voltage of VSCs [82],[87]-[92], which are not noticeable effects in VSC operation. Further, the proposed controller considers both angle and voltage control requirements by providing an additional signal for the voltage loop to stabilize the system, which can be considered as a nonlinear supplementary control signal. The nonlinear supplementary control structure is inherently designed in the large-signal sense and therefore, it automatically provides improved dynamic performance and global stability as compared to conventional small-signal-based solutions [40].

1.3.4 General Interface for Power Management of Microgrids by Nonlinear Cooperative Droop Control

This thesis also proposes a general control strategy, for both converter- and synchronous-machine-based DG units in MGs, based on a combined angle-frequency droop controller with improved dynamic performance. As compared to previous autonomous control strategies, the proposed controller has the following advantages. 1) The proposed strategy combines frequency and angle droop strategies, therefore better power sharing accuracy can be obtained. In addition, designer has more degrees of freedom to select drooping gains since there are two droop loops. Satisfactory static and dynamic performances can be simultaneously fulfilled by proper selection of these two constants. 2) Since the first loop is the angle loop, a designer has more degree of freedom, with respect to controllers in 1.2.1, to adjust the set values of the angle and power loops such that better overall large signal stability and power sharing accuracy are simultaneously achieved. In fact, to inject a given power in the grid-connected mode, there are infinite combinations of power and angle references and by optimization of these values system performance can be significantly improved. 3) A supplementary nonlinear controller is designed to assist the angle-frequency droop controller. It provides a supplementary additional signal for the voltage control loop. The duty of the nonlinear controller is to preserve large-signal stability of the MG when severe contingencies, such as transition to islanding, out-of-phase closing and DG

reconnection occur. The embedded virtual inertia can significantly improve power system dynamic performance and frequency regulation especially in converter-dominated grids where grid equivalent rotational inertia is low [48], [93].

1.3.5 Current Management Methodology for Weak Microgrids by Multivariable Droop-Based Synchronous Converter

Although the technique of power synchronization has been proposed in [35], [58] to overcome problems resulted from PLL, it is a simple power loop aims at adjusting the load angle based on the real power error and the supplementary power synchronization controller acts like a virtual PLL by emulating the behaviour of SGs. However, it suffers from highly real and reactive powers coupling and large steady-state error In fact, in weak grids, dq-axis components coupling result in poor disturbance rejection and noticeable steady-state error. In other words, in weak grids the single-input single-output (SISO) controllers does not offer satisfactory performance and multivariable control is necessary [94]-[98]. In order to realize a promising decoupled control, several methods have been reported in the literature [94]-[98]. Nonetheless, these methods are developed for single loop current-controlled-VSCs and are sensitive to mathematical modeling mismatch. An optimization based multivariable control design has been reported in [96]. Nevertheless, none of the proposed methods are applicable to both islanded and grid-connected modes and since they are based on the vector control strategy, they are subject to stability issues in weak grids.

This thesis presents a control and management strategy for weak MGs based on loop shaping technique and multivariable control. The controller adopts a multivariable controller which realizes d- and q-axis current components superior decoupling. The decoupled behaviour results in better dynamic and static performance in weak grids where real and reactive powers are highly coupled. The current loop is used for current regulation during grid connected mode and it can realize accurate current regulation and current sharing during islanding mode by a multivariable droop. Thus, current regulation, limitation and sharing are embedded in one compact and neat strategy. In summary, a universal compact

multivariable topology with current regulation, limitation and sharing capability and applicable to very weak MGs with superior dq-axis decoupling capability are the main benefits of the controller.

1.3.6 Nonlinear Power Damping Control of Weak Grids

Synchronization of a VSC to a grid is of high importance since any mal-synchronization may lead to severe transients and protection system action [99]. When an islanded VSC is suddenly connected to the grid via a weak interface without a synchronization process, frequency and angle mismatch between a VSC and grid at the moment of connection may cause severe transients. As mentioned earlier, another major concern related to VSC operation in weak grids is the lack of physical inertia in conventional VSCs resulting in poor frequency and load angle regulation; thus, islanded operation of MGs with high penetration of VSCs can be prone to frequency instability. Accordingly, significant efforts have been recently devoted to introduce some dynamics for frequency using virtual inertia.

Motivated by the aforementioned challenges, a hybrid nonlinear control of VSCs in weak grids is proposed in this thesis. The main characteristic of the proposed controller is that the hybrid nonlinear power damping controller enables self-synchronization of a VSC in weak grids. This means that the controller does not need a separate synchronization unit and it automatically synchronizes itself with the grid. Self-synchronization is a new concept [100], and its importance is more pronounced in weak grids. It should be noted that the proposed method in [100] still needs the inception time of synchronization and some information from the remote grid, thus it cannot realize a true plug-and-play operation. Moreover, its performance and stability in weak grids have not been investigated. It is noticeable that during islanding, an MG may usually face permanent frequency drop representing considerable frequency and angle mismatch at the moment of reconnection, however, with the proposed controller system does not need any initial synchronization with grid and it realizes a plug-and-play system.

1.4 Research Objectives

Driven by the aforementioned challenges, this dissertation is an attempt to address a universal family of controller-management strategies for VSCs and conventional SGs in smart distribution grids and enhancement of their operation in the large signal sense and weak grids. To achieve these goals, the following subtasks are proposed:

- Creating a new comprehensive and general family of managers-controllers for VSCs mainly for MG operation which can realize requirements of both grid-connected and islanded operational modes without the need for reconfiguration and also present dynamic characteristics similar to SGs and emulated virtual inertia by developing the concept of synchronous converter.

- Proposing a novel control strategy for integrating VSCs to smart power grids with ability of simultaneous regulation of dc-link voltage, ac side voltage and power which makes it suitable for dc and hybrid ac/dc MGs using the concept of synchronous-VSC.

- Establishing foundations for large signal stability of MGs with stability in a wide range of operating points by emulating inertia and nonlinear microgrid stabilizer.

- Developing a general and unified control framework for incorporating VSCs and SGs into MGs with ability to work in both islanding and grid-connected modes without a need for reconfiguration, constant steady state frequency operation and large signal stability using the concept of nonlinear cooperative droop control.

- Providing the basis for operation of DG units and VSCs in very weak grids with guaranteed large signal stability and self-synchronization capability by the concept of nonlinear power damping control.

- Besides extremely nonlinear behaviour of VSCs in weak grids which necessitates nonlinear power damping, another major issue related to the operation of weak MGs is noticeable coupling between real and reactive powers or equivalently d- and q-axis currents which results in large steady state error, poor performance and instability when system drifts to the nonlinear region. Toward this, the concept of multivariable synchronous converter will be proposed for current management of weak MGs to realize superior decoupling by using loop shaping technique.

Chapter 2 New Family of Microgrid Control and Management Strategies in Smart Distribution Grids-Modeling, Testing and Comparison[1]

This chapter presents a general framework for power and current management of MGs by a universal family of controllers-managers in smart distribution grids applicable to both islanded and grid-connected mode without a need for reconfiguration action. The controller are based on the new concept of synchronous converters as they mimic the dynamic characteristics of SGs as they provide frequency and voltage regulation similar to SGs with emulated inertia. The proposed controllers are compact and neat ones which open a new field for integration of VSCs into future smart grids as they can overcome problems resulted from interaction between conventional electric machines and VSCs and also realize many operational requirements of MGs by one comprehensive strategy.

2.1 The Load Sharing Theory

Fig. 2.1 shows a typical MG including two DG units, local loads and a common load connected at the point of common coupling (PCC). The MG is connected to the utility grid at the PCC through a static switch. If the static switch is closed, the MG is in the grid-connected mode whereas if it is opened, an islanded MG is formed. To improve system reliability and guarantee continuous power supply of the critical and sensitive local loads, the islanding operation of MGs is becoming an essential requirement of smart grids [9]. As mentioned earlier, in an islanded MG, it is required that DG units share total power demand among themselves proportional to their power capacities. In a grid connected mode, a DG unit should generate its preset power or current. The basic theory of power and current sharing is investigated by the study of power-flow in Fig. 2.1. The power-flow of

[1] This work is published in *IEEE Transactions on Power Systems* [101].

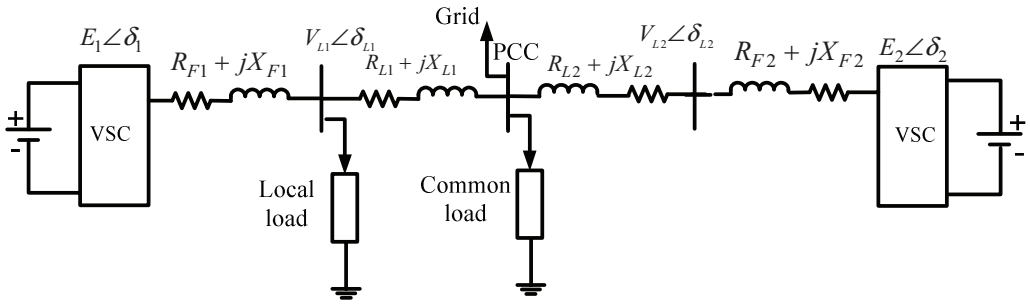

Figure 2-1. A typical MG with local and common loads.

the *i*th unit is expressed by the well-known equations

$$P_i = \frac{E_i}{R_{Fi}^2 + X_{Fi}^2}(X_{Fi}V_L \sin\delta_{DGi} + R_{Fi}(E_i - V_L\cos\delta_{DGi})) \tag{2.1}$$

$$Q_i = \frac{E_i}{R_{Fi}^2 + X_{Fi}^2}(R_{Fi}V_L \sin\delta_{DGi} + X_{Fi}(E_i - V_L\cos\delta_{DGi})) \tag{2.2}$$

The main assumptions in the conventional control methods are that the load angle is small and the line is inductive. In this case, the real power is controllable through the load angle δ_{DG} and reactive power is regulated by the voltage amplitude. The method which is usually employed for the power sharing is to drop frequency as a function of the real power and drop voltage amplitude proportional to the reactive power. The $P-\omega$ and $Q-E$ droop controls are addressed as

$$\omega = \omega_0 - m_i(P_{avgi} - P_{seti}) \tag{2.3}$$

$$E = E_0 - n_i(Q_{avgi} - Q_{seti)} \tag{2.4}$$

where P_{avg} and Q_{avg} are the average real and reactive powers, respectively, which are adopted instead of their instantaneous values to eliminate VSC switching effects and avoid interference between power and current loops and are expressed by

$$P_{avg} = \frac{\omega_c}{s+\omega_c}P \tag{2.5}$$

$$Q_{avg} = \frac{\omega_c}{s+\omega_c}Q \tag{2.6}$$

Since the goal of power sharing is to minimize the circulating current among DG units, an alternative is to use current components as drooping variables and

consequently apply direct current sharing instead of conventional power sharing. Toward this, if (2.1)-(2.2) are presented in the *d-q* frame, the following equations are derived

$$P_i = 1.5(e_{di}i_{di} + e_{qi}i_{qi}) \tag{2.7}$$

$$Q_i = 1.5(e_{di}i_{qi} - e_{qi}i_{di}) \tag{2.8}$$

which in steady-state are simplified to

$$P_{i-steady} = 1.5e_{di}i_{di} \tag{2.9}$$

$$Q_{i-steady} = 1.5e_{di}i_{qi}. \tag{2.10}$$

This means that real and reactive powers are proportional and controllable through i_d and i_q, respectively. Therefore, P and Q can be replaced with i_d and i_q to realize a direct current sharing and control. The governing equations in this case are

$$\omega = \omega_0 - m_i(i_{d-avgi} - i_{d-seti}) = \omega^* - m_i i_{d-avgi} \tag{2.11}$$

$$E = E_o - n_i(i_{q-avgi} - i_{q-seti}) \tag{2.12}$$

Similar to power sharing, the average current components are adopted for drooping, and they are given by

$$i_{d-avg} = \frac{\omega_c}{s+\omega_c} i_d \tag{2.13}$$

$$i_{q-avg} = \frac{\omega_c}{s+\omega_c} i_q \tag{2.14}$$

Equations (2.11)-(2.14) realize direct current management-sharing in an MG whereas (2.3)-(2.6) provide power sharing. Although the power sharing is the common adopted method, designers can also employ the current sharing as it fulfills direct control and management over the currents of DG units. Also, the frequency drooping suffers from some drawbacks such as permanent frequency offset and low stability margin [5]. To compensate the permanent frequency drop, the angle drooping is recently proposed in [40]-[41],[61] which necessitates a general clock and communication links in an MG to synchronize various units [40],[61].

2.2 Proposed Strategies for MG Management

In this chapter, a new family of management methodologies is proposed using either current or power sharing which integrates the requirements of MG operation in one compact structure called synchronous converter. To determine the output power requirements, the controller employs independent real/reactive power control strategies. The output of the power manager can be either d-q currents or voltage amplitude and frequency. The first is a CC-VSC and the latter is a VC-VSC. In the current-controlled VSC, a PLL is required to process the measured currents and voltages of the DG unit and to estimate the local frequency.

2.2.1 Real Power Management and Frequency Control

To share real power among DG units, either frequency or load angle drooping method can be utilized. It was mentioned that the load angle regulation is the basic tool for power sharing. An alternative approach to benefit from advantages of both frequency and angle droop methods is to combine them and use as one unified control method. Fig. 2.2 represents the proposed hybrid droops with connection of angle and frequency droops in series. The series connection of the frequency and angle loops allows to use advantages of both drooping methods and they provide some damping and synchronizing power which significantly enhance system stability It has three cascaded loops namely angle, frequency and power loops. The first loop is the frequency loop in which the reference angle is obtained as a function of the frequency error. Generated by the angle droop loop, the reference of the real power loop is obtained. The power loop involves an integrator which acts as a controller and simultaneously emulates momentum of inertia of a virtual rotor and introduces some dynamics for frequency. As shown in Fig. 2.2, the output of the power controller can be either frequency (Fig. 2.2 (a)) or d-axis reference current (i_{dref}, Fig. 2.2 (b)). The first case yields a VC-VSC whereas the latter yields a CC-VSC. The CC-VSC has the benefits of current regulation, current limitation and better current quality due to the

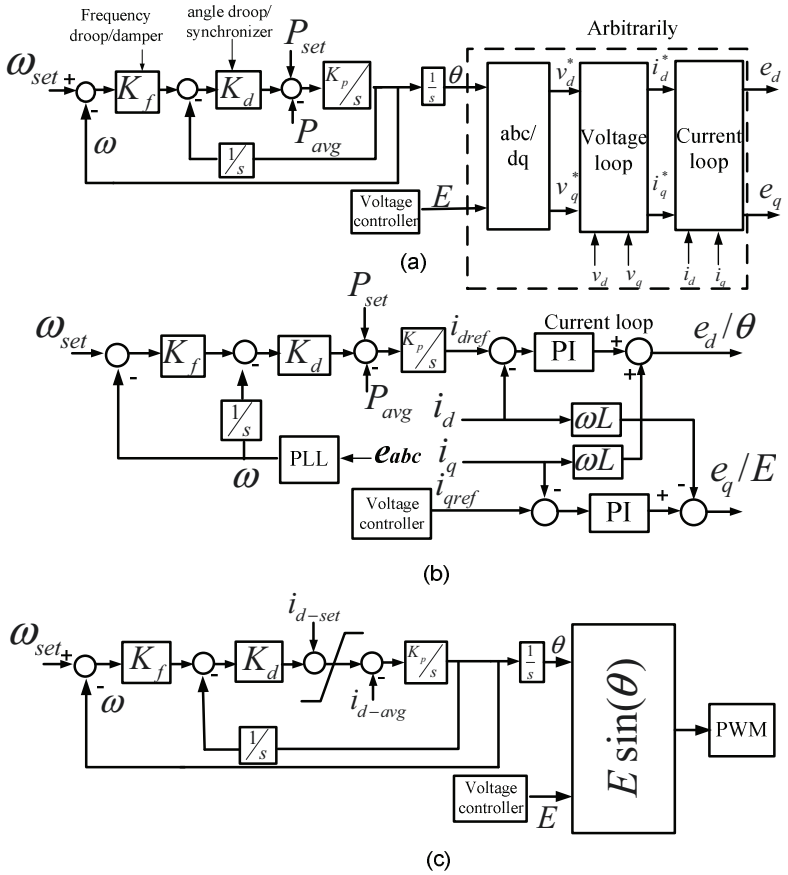

Figure 2-2. Proposed topologies with cascaded series frequency-angle drooping; (a) VC-VSC with power drooping (model-a), (b) CC-VSC with power drooping (model-b), (c) Current-course-based CC-VSC with current drooping (model-c).

existence of a current loop; however, it is not a suitable choice for an autonomous MG because of lack of voltage frequency and amplitude regulation which may result in poor voltage profile and even instability whereas it is a good candidate for a grid connected DG. If a voltage amplitude control loop is embedded within the reactive power manager, since voltage regulation is realized in the reactive power manager, it is possible to eliminate the voltage loop and apply the vector voltage directly to the PWM; however current quality may be deteriorated since there is no current regulation and feedback loop.

The existence of the current loop allows current shaping, regulation and limitation simultaneously with very fast response. Actually, this is a neat controller which augments many of the MG operational requirements in one compact structure. In spite of this, if the inner current and voltage loops are

removed from model-a, current limitation and regulation are missed which may result in very high current injection during severe contingencies and poor current quality. Otherwise, if inner loops are adopted, they may degrade system overall stability and the response speed. If the output vector voltage is directly applied to the VSC, the extra internal voltage and current regulation loops shown in Fig. 2.2 (a) can be eliminated which results in very fast response with very high bandwidth. Another major advantage of model-c is that it operates as a current-source-based VSC with high equivalent parallel impedance which in turn facilitates smooth grid synchronization [37].

2.2.2 Reactive Power Management and Voltage Control

The proposed topologies are shown in fig. 2.3. They consist of sequential voltage and reactive power loops. The model shown in Fig. 2.3 (a) provides a constant voltage operation with proper reactive power adjustment. Although constant voltage operation can be applied to both grid-connected and islanded DG units, it is not the common approach for an islanded MG. On the contrary, the voltage drooping is applicable for both operational modes but it is not an optimal solution for a grid-connected MG since voltage regulation is violated. It is recommended in [9] that for the sake of constant voltage regulation, one DG unit works in constant voltage mode whereas other units should participate in the reactive power sharing. To obtain a general topology for both modes, the integrator must be eliminated. In the case of $K_w = 0$, the characteristics equation is obtained as

$$Q_{avg} = Q^* - K_v E_{fb} \tag{2.17.a}$$

$$Q^* = K_v E_{set} \tag{2.17.b}$$

Based on (2.9-2.10), reactive power is proportional to i_q, so the q-axis current can be utilized for the reactive power control while current regulation is automatically realized within the reactive power manager. In this case the static characteristic equation is

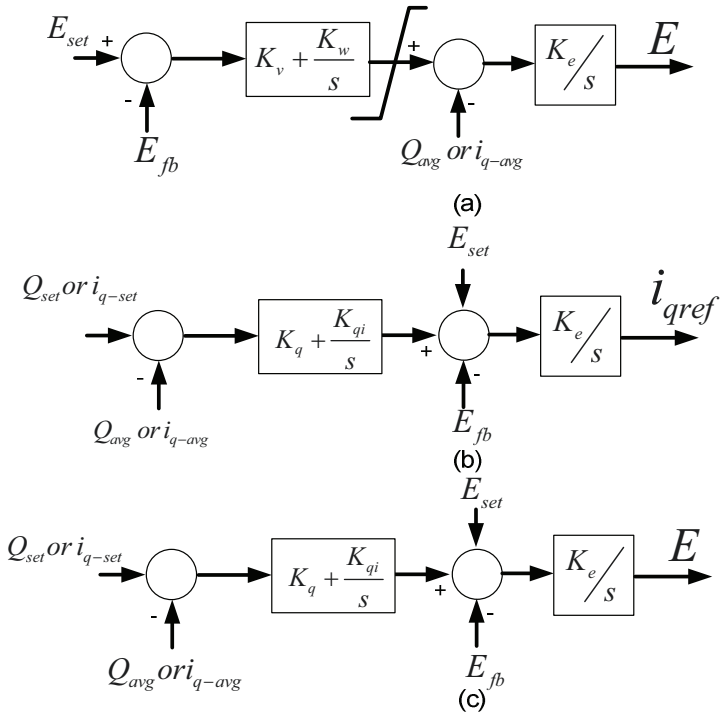

Figure 2-3. Voltage control methodologies, (a) Voltage-controlled constant voltage bus, (b) Current-controlled constant reactive bus and (c) Voltage-controlled constant reactive power bus.

$$i_{q-avg} = i_q^* - K_v E_{fb} \tag{2.18.a}$$

$$i_q^* = K_v E_{set} \tag{2.18.b}$$

If an islanding detection strategy is available within the controller, the reactive power management can be changed from P-V to voltage drooping after transition to islanding by setting K_w to zero which is not the case in this chapter.

Fig. 2.3 (b) represents a current-controlled constant reactive power bus in which the voltage reference in the outer reactive power regulation loop is adjusted to compensate the reactive power error and q-axis current component is regulated as a function of voltage amplitude error. Similar to model–b of the real power controller, since this topology cannot usually guarantee voltage regulation within acceptable limits during islanding, the current controlled method is mainly applicable to a grid-connected DG unit. Therefore, to realize a CC-VSC control, topologies shown in Fig. 2.2 (b) and Fig. 2.3 (b) should be adopted for the real and reactive power management, respectively.

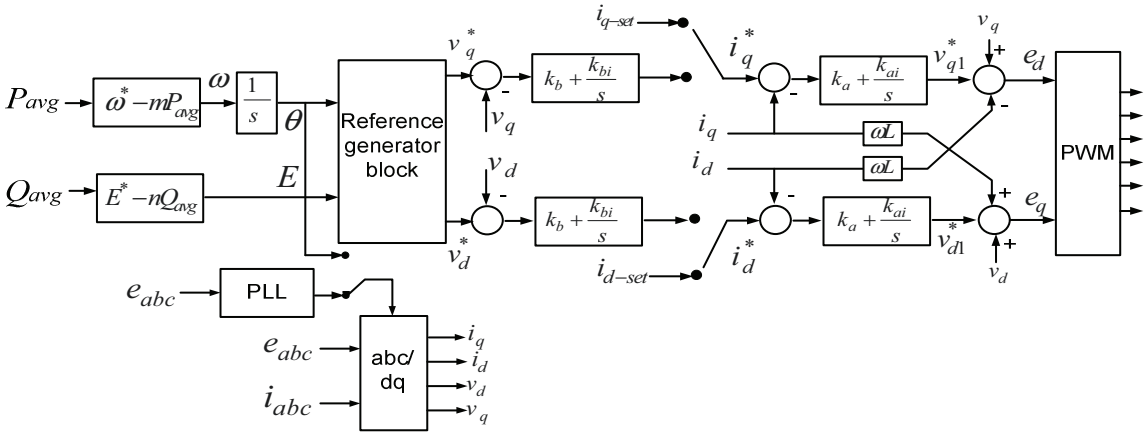

Figure 2-4. The conventional control strategy.

To have a voltage-controlled constant-Q bus, the sequence of reactive power and voltage loops are reversed in Fig. 2.3 (c). Suitable for the grid-connected mode, the constant-Q bus is not appropriate for the autonomous mode and may lead to severe under- or over-voltage and even instability. Moreover, the reactive power sharing is also not fulfilled in an autonomous MG. In other words, if a DG unit is employed as a constant-Q bus in the grid-connected mode, it may suffer from poor voltage regulation and instability subsequent to islanding. If the integrator is removed ($K_{qi}=0$), the proportional gain (K_q) is equal to the voltage drooping constant (n):

$$E = E^* - K_q Q_{avg} \tag{2.19.a}$$

$$E^* = E_{set} + K_q Q_{set} \tag{2.19.b}$$

$$E = E^* - K_q Q_{avg} \tag{2.20.a}$$

$$E^* = E_{set} + K_q i_{q-set} \tag{2.20.b}$$

2.2.3 Conventional Control Strategy

Fig. 2.4 shows the conventional MG control strategy. As shown, for the grid-connected mode, the VSC acts as current source and generates the preset dq-axis currents whereas subsequent to islanding, the controller is switched to voltage-controlled power drooping, therefore an islanding detection technique is required for the switching action. Also, for the grid-connected mode, a PLL is necessary to detect the grid angle and synchronize the VSC to the grid.

Table 2-1 Comparison of Different Control Strategies.

Feature	Model-a (without inner loops)	Model-b	Model-c	Conventional strategy
Generality for both operational modes	✓		✓	
Constant frequency operation	✓	✓	✓	
Seamless transition to islanding	✓		✓	
Current regulation		✓	✓	✓
Current limitation		✓	✓	✓
Mimicking SGs	✓		✓	
Elimination of PLL in steady state	✓		✓	
Vector control		✓	✓	✓
Polar control	✓		✓	
Current-source-based operation		✓	✓	✓

2.2.4 Discussion

The proposed real power management strategies involve power drooping voltage-controlled (model-a), power drooping current controlled (model-b) and current drooping voltage-controlled VSC (model-c). Table 2.1 shows a comparison between the characteristics of the proposed controllers and the conventional control strategy. For the sake of voltage regulation and reactive power control, the constant voltage operation, constant reactive power operation and voltage drooping are proposed. By the proper combination of real and reactive power control strategies, current-controlled-based, voltage-controlled-based and hybrid voltage-current-control-based operation can be obtained. For example, if the current-controlled-based (model-c) management and constant voltage regulation (Fig. 2.3 (a)) strategies are adopted, hybrid current- and voltage-controlled VSC is realized. Alternatively, polar vector and hybrid polar-vector control are various available variants as model-a, model-b and model-c work in polar, vector and hybrid coordinates, respectively. The controllers also augment the secondary and primary controllers in one neat compact controller as they provide nominal frequency and voltage restoration, and voltage and current regulation in one topology. Since the model-b is a current controlled one and cannot guarantee voltage regulation, it is not commonly a good candidate for the islanding mode and consequently cannot realize a universal strategy. The power drooping voltage controlled strategy is not able to guarantee current limitation and regulation without the inner loops. Inner current and voltage loops can provide

voltage and current regulation and limit the current amplitude during fault and transients; however they reduce the overall controller bandwidth and response speed and may degrade system stability. This control strategy can work in both modes without controller switching. Model-c can provide current management, regulation and limitation in one compact and neat scheme without the need for inner loops. It is a hybrid polar-vector controller with ability to work as both current source-based and hybrid current- and voltage-source-based controller. The same concept is valid for the reactive power/voltage controller with inner *q*-axis current loop (Fig. 2.3 (a)) where voltage and current regulation, limitation and sharing are achieved simultaneously. It should be noted that all the proposed controllers need a synchronization process for their initial start-up by using a PLL; however, model-a and model-c can realize self-synchronization with the grid after initial synchronization without a need for a PLL.

2.3 Small Signal Analysis

To analyze the dynamic performance of the proposed control schemes and optimize their parameters, a set of small-signal analysis for a grid connected VSC is performed on the systems shown in Figs. 2.2 (a) and (c) (model-a and model-c). These two topologies are selected for further studies because of their generality for both grid-connected and autonomous modes and elimination of PLL in steady state.

2.3.1 Model-a with Power Feedback

In this section, small-signal dynamics of model-a is obtained. The load angle derivative is given by

$$\Delta\dot{\delta} = \Delta\omega. \tag{2.21}$$

The frequency dynamics is governed by

$$\Delta\dot{\omega} = -K_p K_d K_f \Delta\omega - K_p K_d \Delta\delta - K_p \Delta P_{avg}. \tag{2.22}$$

Considering (2.5), the average power derivative is expressed by

$$\Delta P_{avg} = -\omega_c \Delta P_{avg} + \omega_c \Delta P. \tag{2.23}$$

The voltage dynamic is calculated based on Fig. 2.3 as follows:

$$\Delta\dot{E} = -K_e K_v \Delta E_{fb} - K_e \Delta Q_{avg} \tag{2.24}$$

where

$$\Delta\dot{Q}_{avg} = -\omega_c \Delta Q_{avg} + \omega_c \Delta Q \tag{2.25}$$

and ΔE_{fb} is the perturbation of the feedback voltage. Equation (2.25) is written for the voltage drooping case with K_w. If a constant voltage bus is required, (2.24) is rewritten as

$$\Delta\dot{E} = -K_e K_v \Delta E_{fb} - K_e \Delta Q_{avg} + K_e z \tag{2.26}$$

$$\dot{z} = -K_w \Delta E_{fb} \tag{2.27}$$

Thus, the new state variable (z) which is the output of the integrator K_w, is introduced to the system. The perturbation of the real and reactive powers at an operating point is obtained by linearization of equations (2.1) and (2.2):

$$\Delta P = H_{p\delta}\Delta\delta + H_{pE}\Delta E \tag{2.28}$$

$$\Delta Q = H_{q\delta}\Delta\delta + H_{qE}\Delta E \tag{2.29}$$

where the variables $H_{p\delta}$, H_{pE}, $H_{q\delta}$ and H_{qE} are given by

$$H_{p\delta} = \frac{1}{R^2 + X^2}(2RE_o - RV\cos\delta_o + XV\sin\delta_o). \tag{2.30}$$

$$H_{pE} = \frac{1}{R^2 + X^2}(RE_oV\sin\delta_o + XE_oV\cos\delta_o). \tag{2.31}$$

$$H_{q\delta} = \frac{1}{R^2 + X^2}(XE_oV\sin\delta_o - RE_oV\cos\delta_o). \tag{2.32}$$

$$H_{qE} = \frac{1}{R^2 + X^2}(2XE_o - XV\cos\delta_o - RV\sin\delta_o). \tag{2.33}$$

Equations (2.21)-(2.27) along with algebraic equations (2.28)-(2.33) present the overall small-signal analysis of the power manager. Fig. 5 represents the modes of model-a as a function of K_f and K_d. The fifth pole is not shown here because it appears far away from the imaginary axis and has high natural damping. It is evident that the MG has acceptable stability margin and the most dominant pole appears away from the imaginary axis. This is due to existence of extra damping and synchronizing powers in this topology which provides more damping as compared to the conventional angle or frequency droop [7,34]. The dominant

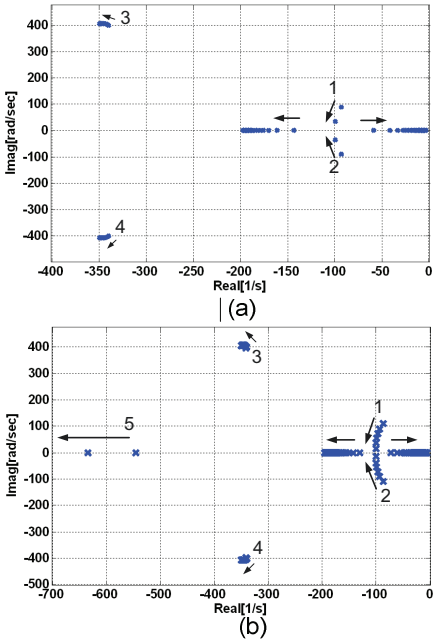

Figure 2-5. Eigenvalue locus of model-a, (a) 0.2< Kf <5. Kd=3e5. (b) 5e4< Kd<1e6.

poles are highly dependent on K_f and K_d while poles number 3 and 4 are almost constant.

Fig. 2.5 reveals that considerable stability margin can be achieved by the proposed controller. However, by further increment of $K_f \times K_d$ the system stability margin is drastically degraded and the dominant mode moves toward the imaginary axis.

2.3.2 Model-c with Current Feedback

In this case, the real power management block is modeled by the following equation:

$$\Delta\dot{\omega} = -K_p K_d K_f \Delta\omega - K_p K_d \Delta\delta - K_p \Delta i_{d-avg}. \tag{2.35}$$

According to (2.13) and (2.14), it is followed that

$$\Delta\dot{i}_{d-avg} = -\omega_c \Delta i_{d-avg} + \omega_c \Delta i_d \tag{2.35}$$

$$\Delta\dot{i}_{q-avg} = -\omega_c \Delta i_{q-avg} + \omega_c \Delta i_q \tag{2.36}$$

The following equations relate i_d and i_q to the load angle and voltage amplitude:

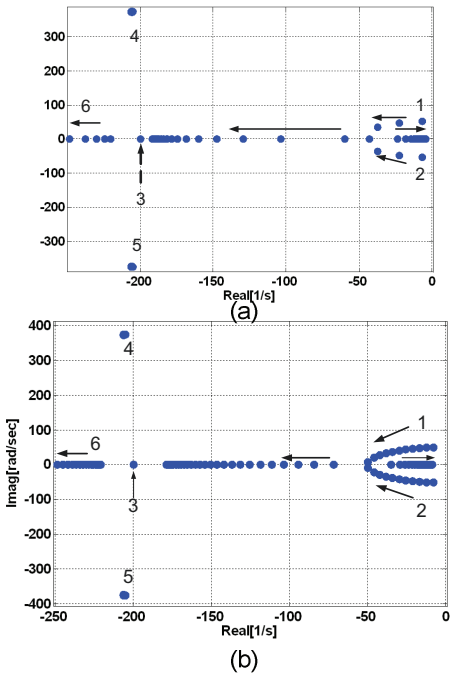

Figure 2-6. Eigenvalue locus of model-c, (a) 0.2< K_f <5. K_d =100, (b) 10< K_d <200.

$$L\frac{di_d}{dt} = E\cos\delta - Ri_d + \omega_0 Li_q - V_d \tag{2.37}$$

$$L\frac{di_q}{dt} = E\sin\delta - Ri_q - \omega_0 Li_d - V_q \tag{2.38}$$

Small-signal dynamics of model-c is obtained by linearizing these equations around the operating point:

$$\Delta\dot{i}_d = -\frac{R}{L}\Delta i_d + \omega_0\Delta i_q - \frac{E_o}{L}\Delta\delta\sin\delta_o + \frac{\Delta E}{L}\cos\delta_o \tag{2.39}$$

$$\Delta\dot{i}_q = -\frac{R}{L}\Delta i_q - \omega_0\Delta i_d + \frac{E_o}{L}\Delta\delta\cos\delta_o + \frac{\Delta E}{L}\sin\delta_o \tag{2.40}$$

The voltage dynamics are the same as (2.24)-(2.27) with the difference that Q_{avg} is replaced with i_{q-avg}. Thus, equations (2.21), (2.22) and (2.34)-(2.40) describe the overall small-signal analysis of model-c. Fig. 2.6 shows the loci of system modes as a function of control parameters. With equivalent drooping constants, the stability margin in this case is pretty similar to the power drooping case and system still presents considerable damping. Mode 3 appears at the cut-off frequency (200 rad/s) and mode 4 appears near to the cut-off frequency and move

toward left by increment of drooping constants. Except two right most modes other modes are not affected by changing drooping constants. By increasing K_f, mode1 moves toward the imaginary axis and mode 2 converges to the cut-off frequency. Modes 3 and 4 are almost constant.

2.3.3 Small-Signal Analysis of a Multiple-DG MG

To investigate the interactions between VSCs which significantly influence the frequency and voltage stability, it is of high importance to evaluate overall system performance in both grid-connected and islanded MGs. In the following, a small-signal framework for a multi-DG MG is presented. From power systems perspective, since most of buses are load ones, modeling the whole system including the load nodes is not helpful to draw a conclusion about the controllers performance. One approach is to model passive loads with their impedances and eliminate these nodes by Kron reduction [102]. In fact, in this case, the load impedances are transferred to be in parallel to the nearby VSCs feeding the load by T to π transformation method and the grid is modeled by an admittance matrix representing the equivalent admittance between the generation units whereas there is no common load node. This allows studying the coupling and interaction between controllers and generation units. To obtain an augmented model for the whole MG, VSCs, network and the grid are combined. In this case, VSCs determine the voltage phasors ($\bar{V}$) the network and load models feedback the power and current to the controller. The governing equations for each VSC are the same as (2.21)-(2.27), with only difference that the real and reactive powers are given by

$$\begin{aligned} P_i = {} & E_i \cos\delta_i \sum_{j=1}^{N+1} (G_{ij}E_j \cos\delta_j - B_{ij}E_{ij}\sin\delta_j) \\ & + E_i \sin\delta_i \sum_{j=1}^{N+1} (G_{ij}E_j \sin\delta_j + B_{ij}E_{ij}\cos\delta_j) \\ & + \frac{E_i^2}{Z_{Li}}\cos\vartheta_i \end{aligned} \tag{2.41}$$

$$Q_i = E_i \sin\delta_i \sum_{j=1}^{N+1}(G_{ij}E_j \cos\delta_j - B_{ij}E_{ij}\sin\delta_j) + E_i \cos\delta_i \sum_{j=1}^{N+1}(G_{ij}E_j \sin\delta_j + B_{ij}E_{ij}\cos\delta_j) + \frac{E_i^2}{Z_{Li}}\sin\vartheta_i \tag{2.42}$$

The terms $E_i^2 \cos\vartheta_i / Z_{Li}$ and $E_i^2 \sin\vartheta_i / Z_{Li}$ represent the real and reactive powers absorbed by the equivalent reflected local load bus, respectively. The term Z_{Li} represents the total equivalent impedance of the local load connected to bus *i* and involves the reflection of the common loads set to the bus *i* after π transformation or Kron reduction. The linearized form of (2.41) and (2.42) around an operating point is

$$\Delta P_i = \sum_{j=1}^{N+1}(\frac{\partial P_i}{\partial E_j}\Delta E_j + \frac{\partial P_i}{\partial \delta_j}\Delta\delta_j) \tag{2.43}$$

$$\Delta Q_i = \sum_{j=1}^{N+1}(\frac{\partial Q_i}{\partial E_j}\Delta E_j + \frac{\partial Q_i}{\partial \delta_j}\Delta\delta_j) \tag{2.44}$$

The overall system state-space model consists of the state-space of all DG units, i.e. $\overline{X} = (\Delta\overline{\delta}, \Delta\overline{\omega}, \Delta\overline{P}_{avg}, \Delta\overline{Q}_{avg}, \Delta\overline{E}, \Delta\overline{z})^T$ where $\Delta\overline{\delta} = (\Delta\delta_1, ..., \Delta\delta_N)$ and the vector of other variables are obtained similarly. The overall MG model is expressed by

$$\dot{\overline{X}} = A\overline{X} \tag{2.45}$$

$$A = \begin{pmatrix} 0_N & I_N & 0_N & 0_N & 0_N & 0_N \\ -K_{pi}K_{di}I_N & -K_{pi}K_{di}K_{fi}I_N & -K_{pi}I_N & 0_N & 0_N & 0_N \\ \omega_c \frac{\partial\Delta\overline{P}}{\partial\Delta\overline{\delta}} & 0_N & -\omega_c I_N & 0_N & \omega_c \frac{\partial\Delta\overline{P}}{\partial\Delta\overline{E}} & 0_N \\ \omega_c \frac{\partial\Delta\overline{Q}}{\partial\Delta\overline{\delta}} & 0_N & 0_N & -\omega_c I_N & \omega_c \frac{\partial\Delta\overline{Q}}{\partial\Delta\overline{E}} & 0_N \\ 0_N & 0_N & 0_N & -K_{ei}I_N & -K_{ei}K_{vi}I_N & K_{ei}I_N \\ 0_N & 0_N & 0_N & 0_N & -K_{wi}I_N & 0_N \end{pmatrix} \tag{2.46}$$

Note that for a grid-connected MG, the perturbations of the real and reactive powers, frequency, voltage and angle of the bus number *N*+1 which is connected to the grid are set to zero and it is assumed that they do not have dynamics ($\Delta\delta_{N+1} = \Delta\omega_{N+1} = \Delta P_{N+1} = \Delta Q_{N+1} = \Delta E_{N+1} = 0$).

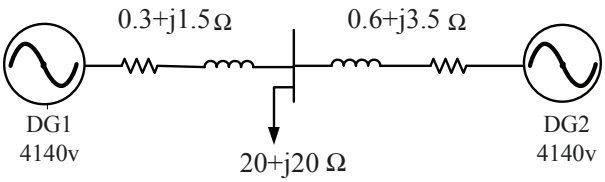

Figure 2-7. The parameters of the analyzed two-DG MG system.

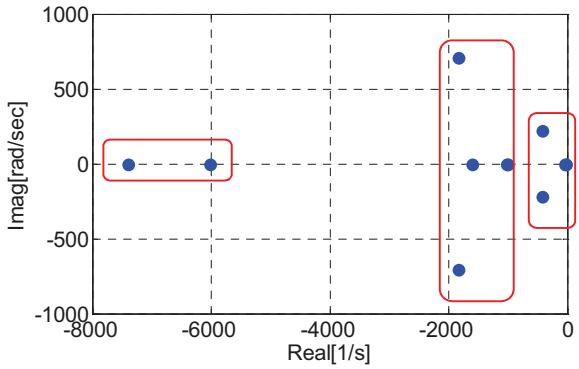

Figure 2-8. The location of eigenvalues of a two-DG MG using model-a.

The proposed model is applied to an islanded MG shown in Fig. 2.7. The MG has two DG units and a common load at its PCC. DG1 is a constant voltage bus whereas DG2 works in voltage drooping mode, i.e. $K_{w2}=0$. The state matrix of A has 11 eigenvalues and Fig. 2.8 shows their locations as three clusters. Fig. 2.9 shows the trajectory of the dominant eigenvalues by variations of K_v, K_w and K_q. The oscillatory mode represented by eigen1, which corresponds to the voltage drooping mode of DG2 with respect to the electrical system has a relatively low damping. Thus, it has a detrimental effect on the system performance. Another factor which significantly affects the dominant eigenvalues is K_{q1}. In fact, as shown in Fig. 2.9 (b), all the eigenvalues except eigen1 are dependent on this parameter. Actually, for low values of K_{q1} modes 5 and 6 become dominant. As shown in Fig. 2.9 (c), eigen2 is mainly influenced by the voltage restoration loop integrator (K_{w1}) whereas other dominant modes are almost constant. Therefore, satisfactory performance and fast response the can be achieved without loss of stability.

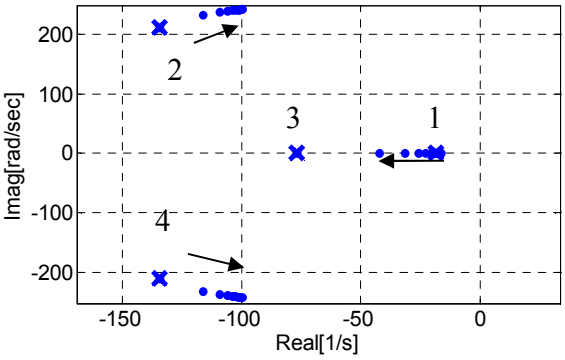

(a)

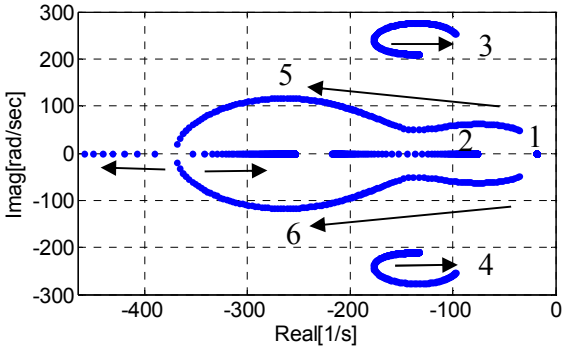

(b)

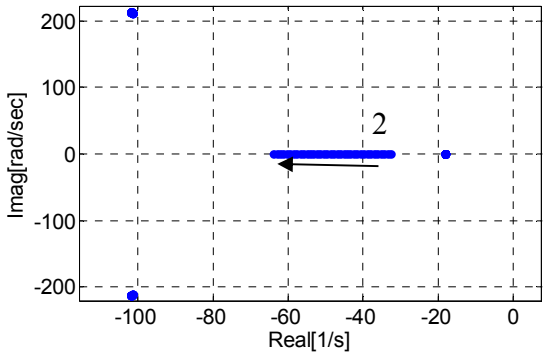

(c)

Figure 2-9. The loci of MG's eigenvalue as by variations of the reactive power manager parameters, (a) $2000 < K_{v2} < 15000, K_{q2} = 0.1$, (b) $K_{w1} = 2e5 \quad K_{v1} = 10000$, $0.01 < K_{q1} < 3$ and (c) $1e5 < K_{w1} < 8e5$, $K_{v1} = 20000$, $K_{q1} = 0.1$.

2.4 Simulation Studies

To evaluate the performance of the proposed topologies, the MG model with the parameters given in Table 2.2 and schematic shown in Fig. 2.10 (adapted from IEEE Std. 399) is simulated in MATLAB/SIMULINK environment. The VSCs' dc-links are considered as inertia-less ones. In this section, model-a and model-c are simulated and in each case, three different scenarios are taken into account.

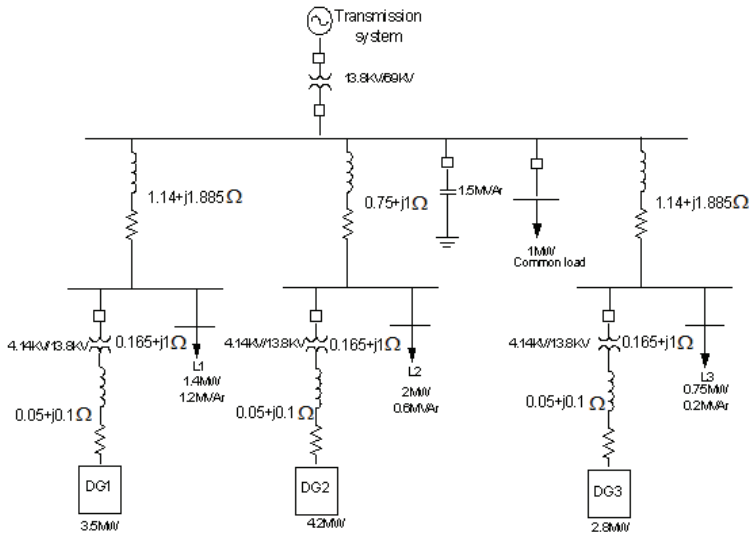

Figure 2-10. The simulated system.

Table 2-2 Controllers Parameters (SI Unit)

Parameter (SI Units)	**DG1**		**DG2**		**DG3**	
	Model (a)	Model (c)	Model (a)	Model (c)	Model (a)	Model (c)
Line-line voltage (V-rms)	4140		4140		4140	
VSC voltage(rms)	4760		4760		4760	
K_d	253000	112.5	304000	135	203000	90
K_f	2	2	2	2	2	2
K_p	0.01	2.5	0.01	2.5	0.01	2.5
K_v	33800	10	40560	12	27000	8
K_w	5e5	50	0	0	0	0
K_e	500	25	500	25	500	25
ω_c	200	200	200	200	200	200

The scenarios include power set points change in the grid connected mode, frequency variation of the grid, transition from to islanding, and disconnection of DG1. During the autonomous mode, both transient and static characteristics are studied. The cascaded voltage-reactive power loops shown in Fig. 2.3 (a) is adopted for the voltage control. It is assumed that DG3 works as a constant voltage bus and two other DG units are used for reactive power sharing; therefore, their integrator gains (K_w) are set to zero. In the case that model-c is adopted for DG3, since it generates the *d*-axis current and the voltage amplitude references, it operates as a hybrid voltage-current source. Although constant voltage regulation

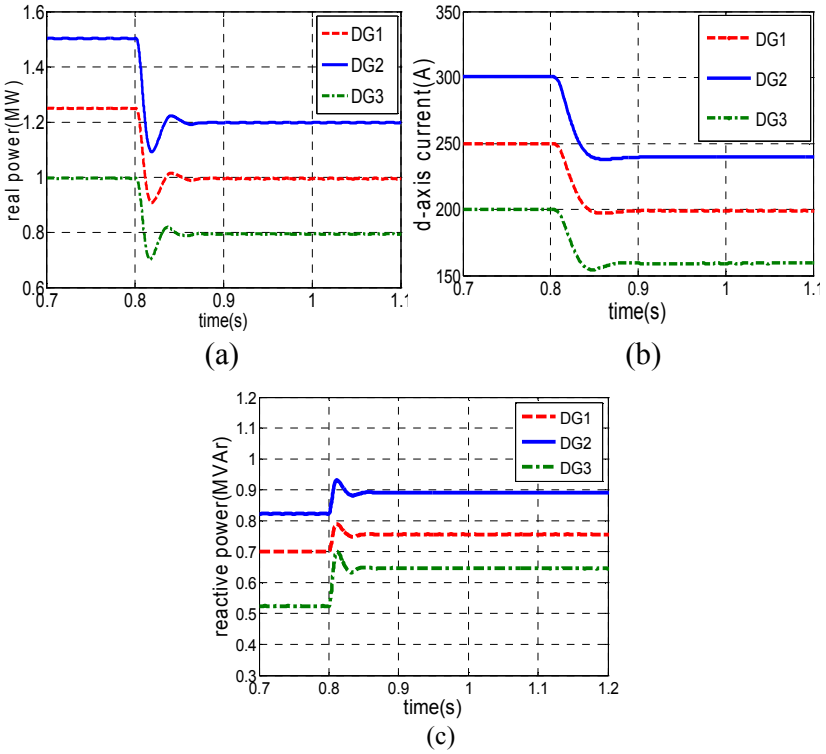

Figure 2-11. System waveforms subsequent to the reference change, (a) Real power waveforms of model-a, (b) *d*-axis current waveforms of model-c, (c) Reactive power of model-a.

is missed in the grid-connected mode for DG2 and DG3, this strategy can realize the reactive power sharing by the voltage drooping in both modes.

2.4.1 Grid-Connected Mode

Fig. 2.11 shows controllers responses of model-a and model-c in the grid-connected mode of operation. The system is initially in the steady-state and at time instant t=0.8 s the converter is subjected to a 20% step reduction in the reference power (model-a) and current (model-c). Fig. 2.11 shows that both model-a and model-c properly regulate the real and reactive powers, and current oscillations are well damped. Model-a offers slightly faster response and system settles within 0.07 s whereas in model-c the settling time is about 0.1 s. The waveforms of reactive power is shown in Fig. 2.11 (c), showing that for the case

of model-a, the reactive powers of DG1 and DG2 before the reference change are equal to 720 and 870 MVAr, representing acceptable sharing accuracy. Since DG3 works as a constant voltage bus, it does not participate in the reactive power sharing. At t= 1.3 s, it is supposed a fault occurs in the main grid and the grid frequency is reduced by 0.5 Hz. Fig. 2.12 depicts frequency variations of DG units during this disturbance which proves that the system is able to track grid frequency variations without a PLL similar to synchronous machines. Both models present satisfactory performance subsequent to this sudden frequency drop manifesting fault ride through capability of these models. Although there is no PLL, the existence of damping and synchronizing power and current provide self-synchronization capability [35],[100]. Furthermore, as it is seen, the frequencies of various DG units in the steady-state are equal; however, they show different transient responses.

2.4.2 Islanding Mode

In this scenario, the static switch is suddenly opened at t= 2.0 s and the MG is disconnected from the utility grid. The real power, d-axis current and instantaneous currents are shown in Fig. 2.13. Both models offer well damped transient characteristics with minimum oscillations. The controller topology and parameters are the same before and after islanding and there is no islanding detection strategy. As shown, the transients settle down within 0.2 s. The angle drooping coefficient (K_d) is adjusted such that MG presents accurate real power sharing and K_f is adjusted based on the small-signal analysis to achieve satisfactory dynamic performance. In this case, in model-a, the generated power of DG1, DG2 and DG3 are equal to 1.67, 2.01 and 1.341 MW, respectively, which indicates the power sharing error is less than 0.5%. In model-c, the steady-state values of i_d of DG1, DG2 and DG3 are 310 A, 375 A and 250 A, respectively. The current sharing error in this case is less than 1% which proves the effectiveness of the proposed current drooping method for the current sharing. In this case, since current sharing and current regulation are embedded within the

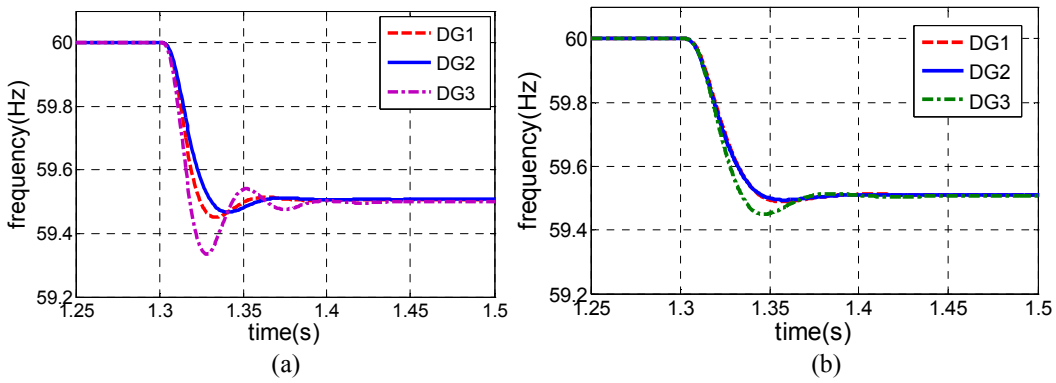

Figure 2-12. Frequency waveforms subsequent to frequency disturbance in the grid, (a) model-a and (b) model-c.

power manager, there is no need for the inner current and voltage loops as shown in Fig. 2.2 (a) which provides higher bandwidth. It is also assumed that the MG has enough power capacity to supply the local loads after islanding.

The key issue in seamless transition to islanding is eliminating the need for reconfiguration and elimination of PLL in the controller. In the conventional strategies, the switching from the current-controlled mode to the voltage control strategy subsequent to islanding and delays related to islanding detection may result in severe transients. The frequency waveforms are illustrated in Fig. 2.14, which clearly confirm that the controllers are well capable of preserving frequency stability subsequent to islanding. The frequencies increase from 59.5 Hz to 60 Hz subsequent to islanding which indicates frequency restoration ability of the controller in islanding mode even in the case that the initial frequency is less than 60 Hz. Note that the frequency responses of various DG units are very close. On the contrary, in the conventional frequency droop controllers, a permanent frequency offset is expected. The load sharing with frequency restoration capability provides better power quality which is an important requirement for sensitive loads, and enables more accurate load sharing without loss of stability.

At t=5.0 s, DG1 is disconnected from the rest of the grid and DG2 and DG3 are responsible to supply the MG total load including the load of DG1. As shown in Fig. 2.15, in model-a, the real power of DG2 and DG3 are increased to 2.901 and

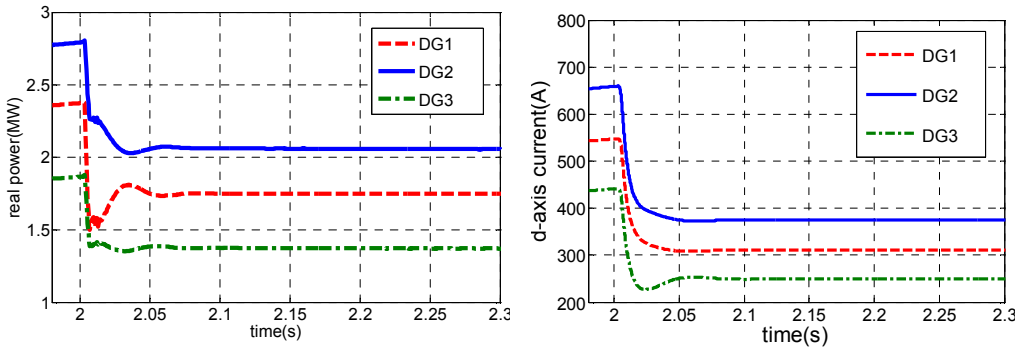

(a) (b)

Figure 2-13. System waveforms subsequent to islanding, (a) *R*eal power waveforms of model-a, and (b) *d*-axis current waveforms of model-c.

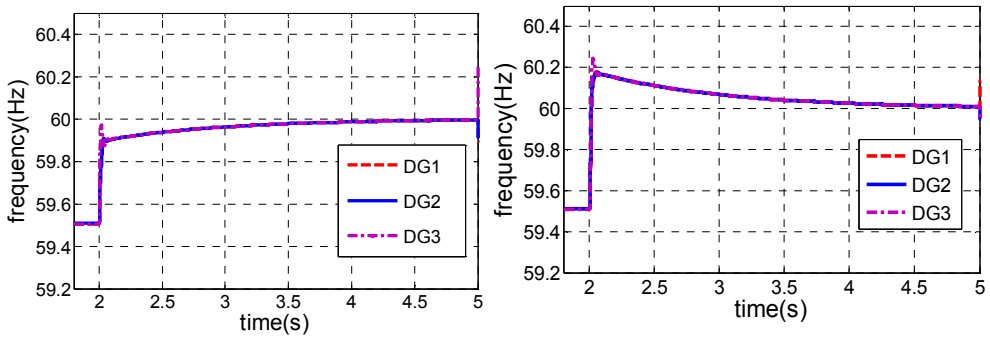

(a) (b)

Figure 2-14. Frequency waveforms subsequent to islanding, (a) model-a and (b) model-c

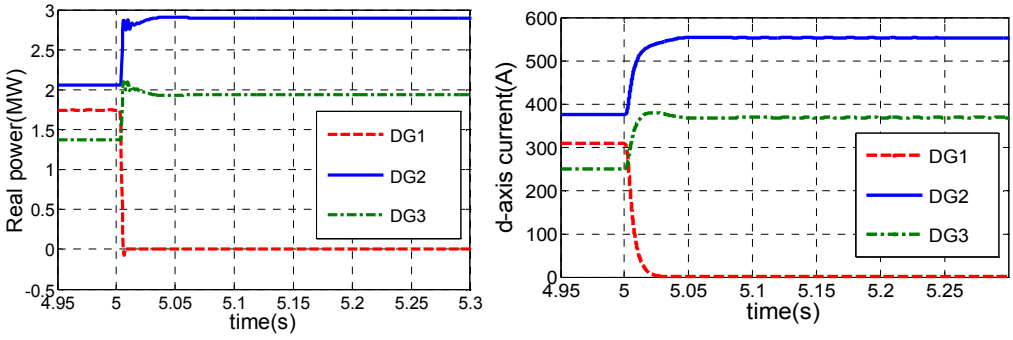

(a) (b)

Figure 2-15. System waveforms before and subsequent to DG1 disconnection, (a) Real power waveforms of model-a, (b) and d-axis current of model-c.

1.935 MW within 0.15 s; in model-c the generated *d*-axis currents of DG2 and DG3 are smoothly increased to 550 A and 371 A, respectively. In this case, although the connecting impedances of DG units are unequal, both models offer

power and current sharing ratio error less than 1%. It should be noted that it assumed that DG units have enough capacity to supply the MG overall demand after DG1 disconnection because in this case the goal is to study transient and steady-state behaviours of the controllers. Available DG capacity is usually guaranteed by a supervisory MG operating center to ensure the power flow matching. It should be noted that the power flow matching is a necessary but not sufficient condition for the system stability.

2.4.3 Comparison to the Conventional Droop

It was mentioned that in the conventional approach, the current source-based VSC is adopted to supply the preset *d*- and *q*-axis currents to the grid whereas subsequent to islanding, the voltage- source-based strategy with power sharing capability is adopted. To compare the performance of the proposed controllers with the conventional control and management policies, the response of the conventional strategy before, during and subsequent to an islanding event is studied. The simulated system is exactly the same as the previous case and it is supposed that in the grid connected mode, the *d*-axis preset currents are $i_{d-set1} = 200\,\text{A}$, $i_{d-set2} = 240$ A and $i_{d-set3} = 180$ A, and the *q*-axis current presets are $i_{q-set1} = 50\,\text{A}$, $i_{q-set2} = 60$ A and $i_{q-set3} = 40$ A.

The parameters of the controllers are given in Table 2.3. The corresponding waveforms of *d*-axis currents and frequencies are shown in Fig. 2.16. The DG units generate the preset currents during grid connected mode. At *t*=2 s the MG is switched to the islanding mode and it is also assumed that islanding is detected without any delay, therefore at *t*=2 s the controller is switched from current-source-based to the voltage-source-based strategy. Fig. 2.16 shows that although there is no islanding detection delay, due to the controller change action, the transition to islanding is not seamless and huge spikes and transients appear in the current waveforms. In spite of this, the model-c provides very seamless transition to islanding without any reconfiguration while it operates as a current-source-based controller and realizes the preset current generation in the grid connected

Table 2-3 The MG with the Conventional Control Strategy (SI Units and the parameters were defined in Fig. 2.4)

Parameter	m	n	K_a	K_{ai}	K_b	K_{bi}
DG1	0.96e-6	0.96e-5	50	15300	0.165	400
DG2	0.8e-6	0.8e-5	50	15300	0.165	400
DG3	1.2e-6	1.2e-5	50	15300	0.165	400

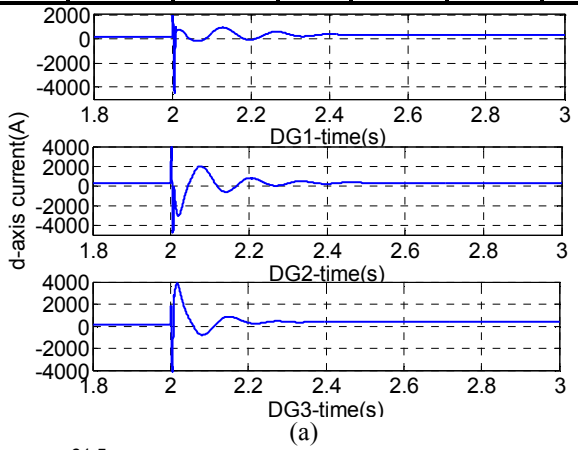

(a)

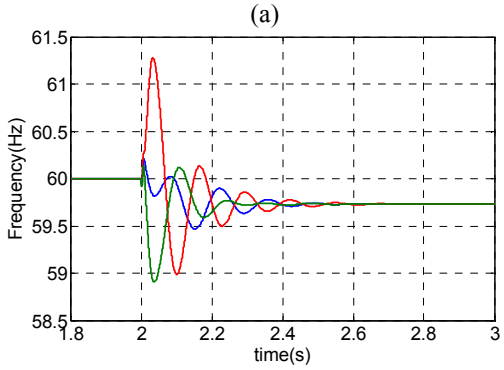

(b)

Figure 2-16. System response of the conventional control strategy in grid connected mode, transition to islanding and islanded mode, (a) *d*-axis currents and (b) Frequency.

mode and share current during islanding. Actually, it presents a hybrid current-voltage source based operation, so it enjoys the benefits of both. If system continues its operation in the islanding mode, the *d*-axis currents in the steady-state settle to $i_{d1} = 330$ A, $i_{d2} = 407$ A and $i_{d3} = 270$ A with current sharing error about 2.5%. The frequency waveforms shown in Fig. 2.16 (b) also reveal that a permanent frequency drop equal to 0.3 Hz occurs in the islanding operation whereas in the proposed controllers the power and current sharing are achieved with the constant steady-state frequency operation at the rated value (e.g. 60 Hz).

Chapter 3 Synchronous-VSC Based Framework for Incorporating VSCs to Smart Power Grids[2]

In this chapter, a comprehensive control strategy is proposed for VSCs. It augments all the aforementioned requirements in one compact topology. Two different topologies, namely virtual torque and direct dc-link voltage control strategies are developed for the frequency control loop. In these topologies, the output power and the dc-link voltage are used as control variables, respectively. It will be shown that the direct dc-link voltage control presents very good performance with a simple control structure; however, the virtual torque control offers more degrees of freedom to select design parameters because there is an extra power loop. For the voltage control loop, two variants are addressed to realize either a P-Q bus or P-V bus operation. A theoretical analysis, simulation and experimental results are presented to verify the validity and effectiveness of the proposed control strategy.

3.1 Polar Control of VSC In Frequency-Angle Domain With Synchronous Machine Behaviour

In this chapter, a control topology is proposed in which the frequency, load angle and dc-link voltage are control variables rather than conventional vector controls which employ current components for dc-link voltage regulation and reactive power control. Thus, direct control of frequency, angle and dc-link power and voltage is available which in turn provides easier controllability and system analysis. In the following, the control topology is described in details. One of the main goals in VSC control is to maintain the dc-link voltage constant. Assuming

[2] This work is published in *IEEE Transactions on Power Systems* [66].

lossless VSC, the input ac power is equal to the dc power $P_{DC} = V_{DC} I_{DC}$; and the reactive power does not correspond to any real power exchange with the converter dc-side. The power-circuit part involves the VSC and the connecting impedance between VSC and the grid and is similar to conventional grid-connected VSC systems. Usually in high power VSCs used in power systems, which are the main scope of this chapter, a pure inductor without capacitor is used as output filter. If the VSC is employed to regulate frequency variations during contingencies, an energy storage system can be installed at the dc-link to transfer power from the energy storage device to the grid to damp the frequency and angle oscillations. However, for rectifier applications in which no energy storage is used, the active load can be used for power exchange with the grid.

3.1.1 Synchronous Machine Model

Generally, an SM involves excitation and damper windings mounted on the rotor and stator three-phase windings. Although the damper windings significantly improve transient performance in terms of synchronism and damping capabilities, and the reluctance torque increases power density of an SM, in this chapter, the model of a round rotor synchronous motor without damping windings is considered. In fact, the effect of damping and synchronizing powers can be emulated by the control functions in the VSC without physical damping components as in conventional SMs. The mechanical dynamics is expressed by

$$J\frac{d^2\theta_r}{dt^2} + K_m\frac{d\theta_r}{dt} + K_s\theta_r = P_m - P_{load} \tag{3.1}$$

where θ_r is the rotor angle; J is the total moment of inertia; and P_m and P_{load} are input mechanical power of SM and the load power, respectively. The constants K_m and K_s provide damping and synchronizing torque components given by

$$Damping\,torque = \Delta T_{damp} = -K_s\Delta\omega_r \tag{3.2}$$

$$Synchronizing\,torque = \Delta T_{synch} = -K_m\Delta\theta_r \tag{3.3}$$

The damping power damps load angle oscillations, whereas the synchronizing power supports machine-grid synchronism.

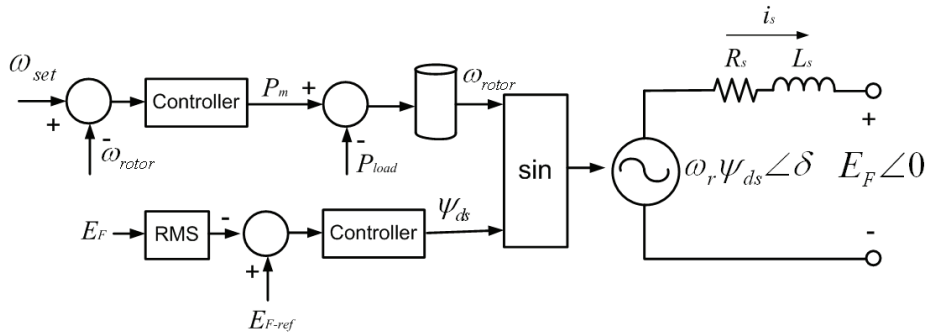

Figure 3-1. SM principal operation and control concept.

The electrical torque of an SM (T) is given by [103]

$$T = \psi_{ds} i_{qs} - \psi_{qs} i_{ds} \tag{3.4}$$

where ψ_{ds} and ψ_{qs} are d- and q-axis flux components, respectively. The reactive power is given by

$$Q = \omega_r \psi_{qs} i_{qs} + \omega_r \psi_{ds} i_{ds} \tag{3.5}$$

where ω_r is the rotor frequency.

It is also useful to model an SM as a voltage behind reactance as shown in Fig. 3.1; where the back-EMF voltage amplitude is given by

$$E = \omega_r \psi_{ds} \tag{3.6}$$

The virtual electrical torque and reactive power in this case are governed by the following equations:

$$T = \frac{P_{vsc}}{\omega_r} = \frac{E}{R_s^2 + (L_s \omega_r)^2} (L_s V_g \sin\delta + \frac{R_s (E - V_g \cos\delta)}{\omega_r}) \tag{3.7}$$

$$Q = \frac{E}{R_s^2 + (L_s \omega_r)^2} (R_s V_g \sin\delta + (L_s \omega_r)(E - V_g \cos\delta)) \tag{3.8}$$

where δ is the load angle, i.e. angle displacement between the back-EMF and grid voltage, and P_{vsc} is the VSC's power. Assuming an inductive stator winding, the injected real power is mainly regulated by the load angle δ whereas reactive power is regulated by VSC voltage amplitude (E). In SGs, the reference power is determined by the governor such that the rated frequency is preserved and the output power or equivalently the load power finally becomes equal to the reference power.

3.1.2 Frequency Control Loop

In this section, the proposed topologies for frequency control are presented. For the frequency control, two variants are proposed-namely virtual torque control and direct dc-link voltage control as depicted in Fig. 3.2. To generate a three-phase sinusoidal voltage in polar system, its amplitude, frequency and angle are required. The voltage generation principle in a synchronous-VSC is similar to back-EMF generation in SGs shown in Fig. 3.1. The back-EMF amplitude is given by $E = \omega\psi_{ds}$, thus the d-axis flux (ψ_{ds}) and frequency are necessary. Toward this, two separate channels are adopted to independently regulate VSC's frequency and virtual flux as shown in Fig. 3.2. The first loop is the frequency control loop shown in Fig. 2 which emulates the mechanical behaviour of an SG with proper control of the dc-link voltage and frequency such that grid views the capacitor as a virtual rotor. The angle of the generated sine wave is easily obtained by integrating the frequency. The goal of the second channel shown in Fig. 3 is to mimic the electrical behaviour of SGs by appropriate adjustment of the virtual flux. Having the frequency and angle trajectories from the first control channel and virtual flux from the second channel, the voltage command is generated by $E = \omega\psi_{ds}\sin(\theta)$.

The virtual torque control structure has three cascaded loops. The first one is the frequency loop which determines the load angle reference; based on the angle error, the virtual torque reference value is obtained in the angle loop. Finally, the power loop adjusts the VSC frequency such that it generates the reference torque. In this case, the reference torque is equivalent to the generated electrical torque of an equivalent SM. The question is that how to set the torque reference to achieve desirable output dc-link voltage because unlike synchronous motors where electrical torque is automatically generated to overcome the load and friction torque at synchronous speed, the main objective of a VSC control is to regulate the dc-link voltage (e.g. in bi-directional VSCs and in VSCs interfacing renewable resources).

Toward this, an extra dc-link voltage and virtual torque control loops are added to the core control loops to adjust the dc-link voltage as a function of the virtual

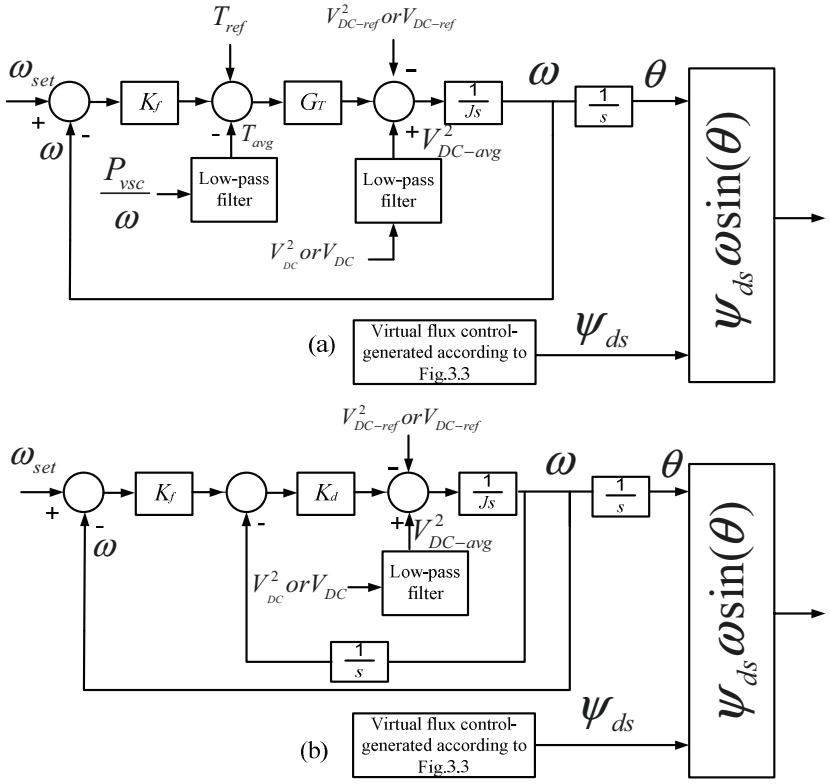

Figure 3-2. Proposed control topologies for frequency regulation; (a) Virtual torque control, and (b) Direct dc-link voltage control.

torque error. If in the grid connected mode we set $T_{ref}=0$, then the VSC generates the dc-link voltage reference, otherwise if ($V_{DC-ref}=0$) it injects the power corresponding to the virtual torque reference (T_{ref}) to the grid.

The frequency dynamics is similar to an SM in which the rotating shaft is opposed by a viscous damping proportional to the frequency deviation plus a damping torque proportional to the load angle deviation. The extra angle loop here offers an additional angle shift which enhances system stability. The augmented dynamic equation of the topology shown in Fig. 3.2 (a) is given by

$$J\frac{d\Delta\omega}{dt}=-K_f G_T\Delta\omega-G_T\Delta T_{avg}-\Delta V^2_{DC-avg} \tag{3.9}$$

$$\Delta\omega=\omega-\omega_{set} \tag{3.10}$$

$$\omega=\frac{d\theta}{dt}\,(a),\ \delta=\int\Delta\omega dt\,(b)$$

The transfer function G_T is the virtual torque controller which is usually a proportional-integral (PI) one with $G_T = K_t + K_{ti}/s$. The load angle is denoted by δ. It should be noted that the controller finally generates the dc-link voltage reference and the frequency and virtual torque loops just affect the transient response. To remove effects of switching and low-order harmonic in the output power; and allow sufficient time-scale separation between the power and voltage control loops, a low-pass filter is used to obtain the average virtual torque

$$T_{avg} = \frac{\omega_c}{s + \omega_c} T \tag{3.12}$$

where ω_c is the cut-off frequency of the low-pass filter. Similarly, a low-pass filter is adopted to extract the dc-value of the output dc-link voltage as follows:

$$V_{DC-avg} = \frac{\omega_c}{s + \omega_c} V_{DC} \tag{3.13}$$

One of the interesting points of this topology is that all control variables except output currents and voltages are internally available within the digital-signal-processor (DSP). To transform variables from *abc* frame to *dq* frame, there is no need for a PLL. However, an initial synchronization process with the grid is needed to overcome severe transients and large currents during converter connection to the grid (i.e. similar to the initial synchronization process of a conventional SM). After the start-up process, the PLL can be removed from the control system and the DSP internally determines the output angle.

An alternative for the virtual torque control topology shown in Fig. 3.2 (a) is the direct dc-link voltage control in which the extra torque regulation loop is removed. In this case, instead of indirect dc-link voltage adjustment via power regulation, the dc-link voltage square, as an index of power, is controlled. This structure is more compact where all requirements are augmented in one general strategy.

The dc-link voltage is controlled based on the power balance between the dc- and ac-sides of the VSC. The stored energy in the dc-link capacitor is given by

$$W = \frac{1}{2} C V_{DC}^2 \tag{3.14}$$

Thus, it is rational to control the torque reference as a function of V_{DC}^2. As it will be shown, this also helps to mitigate nonlinearities produced in the state-space model. Based on Fig. 3.2 (b), the governing equation in this case is

$$J \frac{d\Delta\omega}{dt} = -K_f K_d (\omega - \omega_{set}) - K_d \delta + V_{DC-avg}^2 - V_{DC-ref}^2 \tag{3.15}$$

Comparing (3.15) and (3.1), it can be observed that the damping and synchronizing torque components can be interpreted as $\Delta T_{damp} = -K_f K_d \Delta\omega$ and $\Delta T_{synch} = -K_d \Delta\theta$, respectively. Both torque components can be controlled in a way that is not possible in a typical SM. It is possible to use V_{DC} instead of V_{DC}^2 as the controller variable; however, it makes system more nonlinear. In the case of a resistive load connected to the dc-link, since $P_{vsc} = V_{DC}^2 / R_{load}$, it is recommended to employ V_{DC}^2 as control variable to mimic SM characteristics. If the load or the generation is modeled as a current source, since $P_{vsc} = V_{DC} I_{DC}$, a better solution is to use V_{DC} as the control variable.

To relate the dc-link capacitance size to the equivalent SM time-constant, the concept of inertia constant (H) and capacitor time-constant τ_c are introduced as follows:

$$H = \frac{W_{SM}}{S_{SM}} = \frac{0.5 J \omega^2}{S_{SM}} \tag{3.16}$$

$$\tau_c = \frac{W_C}{S_{VSC}} = \frac{0.5 C V_{DC}^2}{S_{VSC}} \tag{3.17}$$

where W_{SM} and W_C are stored energy in the SM and capacitor, respectively, and S_{SM} and S_{VSC} are the rated power capacity of the synchronous machine and VSC, respectively. If the damping and synchronizing coefficients in (3.1) are ignored, the dynamic equation of an SM can be rewritten as a function of (H) and frequency (f) as

$$\frac{2H}{f_0} \frac{df}{dt} = P_m - P_{load} \tag{3.18}$$

Similarly, the dynamic equation of the capacitor can be expressed as

$$\frac{CV_{DC}}{S_{VSC}}\frac{dV_{DC}}{dt} = P_{in} - P_{source} \tag{3.19}$$

where P_{in} and P_{source} are input and output (source) power to the capacitor. To obtain the size of the capacitor corresponding to the equivalent SM with similar power rating, equations (3.18) and (3.19) are set equal and both sides are integrated [49]

$$\int \frac{CV_{DC}}{S_{VSC}} dV_{DC} = \int \frac{2H_{VSC}}{f_0} df \tag{3.20}$$

$$\frac{2H_{VSC} f}{f_0} = \frac{CV_{DC}^2}{2S_{VSC}} + K_1 \tag{3.21}$$

$$K_1 = 2H_{VSC} - \frac{CV_{DC0}^2}{2S_{VSC}} \tag{3.22}$$

where f, f_0 and V_{DC0} are frequency in Hertz, nominal frequency and nominal dc-link voltage. H_{VSC} is the equivalent emulated inertia introduced to the power system by the VSC. With some simplification, the emulated inertia time-constant is obtained as [49]

$$H_{VSC} = \frac{\frac{1}{2}\frac{CV_{DC0}^2}{S_{VSC}}[(\frac{\Delta V_{DC}}{V_{DC0}} + 1)^2 - 1]}{2\frac{\Delta f}{f_0}} \tag{3.23}$$

where ΔV_{DC} and Δf are the maximum dc-link voltage and frequency deviations:

$$\Delta V_{DC} = V_{DC} - V_{DC0}, \Delta f = f - f_0 \tag{3.24}$$

Using (3.23), (3.24), the dc-link capacitance required to emulate the rotor of a SG by a VSC for given frequency and dc-link voltage deviations can be calculated.

Although the controller is mainly proposed for integration of VSCs into power grids and it is originally developed for grid connected mode, it is worth investigating its behaviour and dynamics during islanded operation. In islanded and in steady-state conditions, the input to the integrator ($1/J$) is zero [100]; therefore, the steady-state characteristic equation is

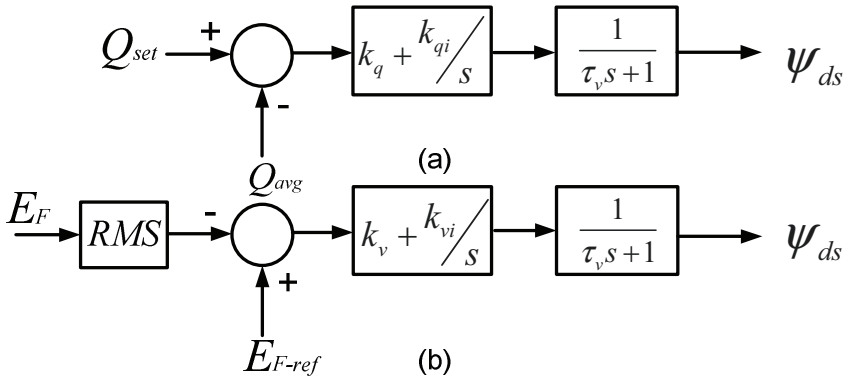

Figure 3-3. Proposed control topologies for the virtual flux regulation, (a) Constant reactive power operation and (b) Constant voltage operation.

$$V_{DC}^2 = V^* + K_f K_d \omega + K_d \delta, \tag{3.25.a}$$

$$V^* = V_{DC-ref}^2 - K_f K_d \omega_{set} \tag{3.25.b}$$

This means that a dc-link voltage against the load angle and frequency rise is obtained. Accordingly, in islanded mode, the dc-link voltage is variable, and in inverting mode an increment in the real power increases the load angle and consequently the dc-link voltage. As the scope of this chapter is on the grid-connected mode, the controller operation in islanded conditions is an open question for future studies.

3.1.3 Virtual Flux Control Loop

Similar to an SM, two strategies can be defined in which the voltage is controlled to 1) generate a pre-specific amount of reactive power, 2) achieve voltage regulation at a specific load-power (P-V bus). These two strategies are shown in Fig. 3.3.

Strategy 1: Reactive Power Regulation. Usually the pre-set value of the VSC input reactive power is set to zero. However, similar to SMs, the synchronous VSC can either absorb (under-excitation) or inject (over-excitation) reactive power to the grid, to support the grid in various situations. This significantly can enhance voltage stability especially when grid falls short to provide enough reactive power for some local loads. A PI controller tunes the virtual rotor excitation voltage such that the required reactive power is achieved. The

excitation dc voltage is transformed to a virtual air-gap flux through a low-pass filter emulating the flux decay behaviour of a real SM caused by the excitation RL circuit. Besides emulating electrical dynamics of an SM, the low-pass filter improves the stability of the system by drifting voltage controller modes to more damped locations in the left-half-plane of the complex-frequency domain. The desirable reactive power tracking and dynamic performance can be simultaneously achieved by optimal tuning of K_q, K_{qi} and τ_v. The criterion for designing τ_v is that it does not pass the switching frequency, usually $1/\tau_v < 0.2\omega_s$, where ω_s is the switching frequency.

Strategy 2: Voltage Regulation. In weak grids where the connecting impedance between converter and grid is high, voltage regulation and stability may be deteriorated, thus in this case, voltage regulation is of high interest to keep bus voltage at a certain value. The controller specifies the corresponding excitation voltage set-point to regulate the PCC voltage to the reference value.

3.2 Small-Signal Analysis

To investigate the dynamic performance and transient response of the system, a small-signal model is developed. The small-signal analysis gives insights on how controller variables variation affects the stability and convergence characteristics of the controlled variables. It also helps in optimum tuning of controller parameters to reach the best trade-off among design objectives. In the following, the small-signal analysis of the frequency controller shown in Fig. 3.2 (b) is presented. The voltage control loop used for reactive power regulation, shown in Fig. 3.3 (a), is analyzed. The small-signal model of other topologies can be obtained in a similar way.

The state-space variables are: $[\Delta\delta, \Delta\omega, \Delta\psi, \Delta x, \Delta y, \Delta z, \Delta E]$,

where $[x = V_{DC-avg}^2, y = V_{DC}^2]$ and z is the output of the integrator of the reactive power controller in Fig. 3.3 (a).

The overall small-signal model of frequency and voltage loops for the generative mode are given as follows:

$$\Delta\dot{\delta} = \Delta\omega \tag{3.26}$$

$$\Delta\dot{\omega} = -a_{22}\Delta\omega - a_{21}\Delta\delta - \Delta x \tag{3.27}$$

$$\Delta\dot{x} = -\omega_c\Delta x + \omega_c\Delta y \tag{3.28}$$

$$\frac{1}{2}C\Delta\dot{y} = -\Delta P_{vsc} - \Delta P_{source} \tag{3.29}$$

$$\Delta\dot{z} = K_{qi}\Delta Q \tag{3.30}$$

$$\Delta\dot{\psi} = -\omega_v\Delta\psi + \omega_v\Delta z - K_q\Delta Q_{avg} \tag{3.31}$$

$$\Delta\dot{Q}_{avg} = -\omega_c\Delta Q_{avg} + \omega_c\Delta Q \tag{3.32}$$

where $a_{22} = K_f K_d / J$ and $a_{21} = K_d / J$. Note that the direction of power flow in considered toward the grid. Considering small disturbances of output power around the stable equilibrium point and under the assumption of zero converter losses, ΔP_{vsc} is given by

$$\Delta P_{vsc} = H_{P\delta}\Delta\delta + H_{PE}\Delta E \tag{3.33}$$

where

$$H_{P\delta} = \frac{1}{R^2 + X^2}(RE_0V_0\sin\delta_0 + XE_0V_0\cos\delta_0) \tag{3.34}$$

$$H_{PE} = \frac{1}{R^2 + X^2}(2RE_0 - RV_0\cos\delta_0 + XV_0\sin\delta_0) \tag{3.35}$$

$$\Delta E = \omega_0\Delta\psi + \psi_0\Delta\omega \tag{3.36}$$

In a similar way, the perturbed form of the reactive power Q is given by

$$\Delta Q = H_{Q\delta}\Delta\delta + H_{QE}\Delta E \tag{3.37}$$

$$H_{Q\delta} = \frac{1}{R^2 + X^2}(XE_0V_0\sin\delta_0 - RE_0V_0\cos\delta_0) \tag{3.38}$$

$$H_{QE} = \frac{1}{R^2 + X^2}(2XE_0 - XV_0\cos\delta_0 - RV_0\sin\delta_0) \tag{3.39}$$

Equations (3.26)-(3.32) along with algebraic equations (3.33)-(3.39) give the overall small-signal model of the VSC with the proposed controller topology.

The design values of the controller parameters can be obtained using the small-signal analysis to achieve satisfactory transient response. The given model has

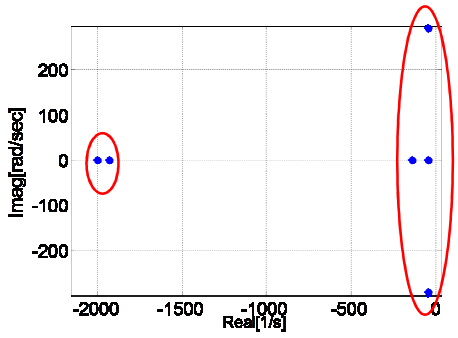

Figure 3-4. Position of eigenvalues as two clusters.

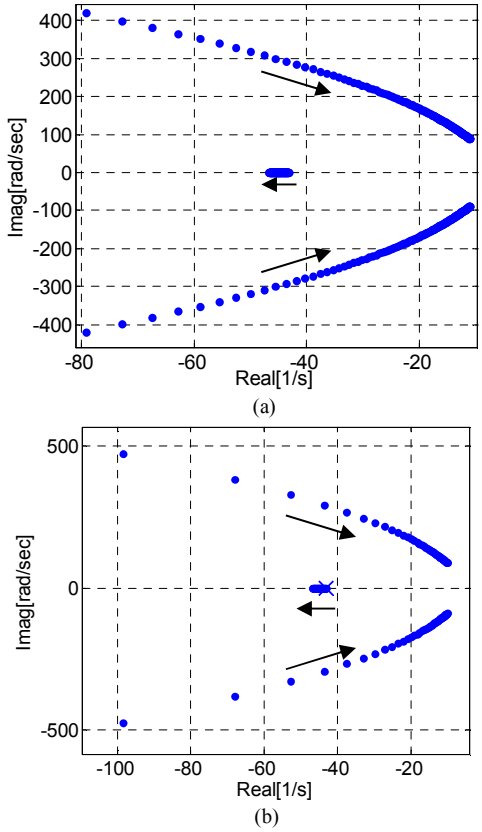

Figure 3-5. Loci of the first three dominant eigenvalues as a function of frequency regulation loop parameters, (a) $500 < K_d < 5000$, $K_f = 10$ and $K_p = 1$, and (b) $1 < K_f < 100$, $K_d = 1000$ and $K_p = 1$ $K_q = 0.0005$.

been used to extract the family of the system eigenvalue plots. The system has three clusters of eigenvalues where six dominant eigenvalues are shown in Fig. 3.4. The seventh pole appears in the left of -50000s-1 which is not shown here. To investigate the effect of the frequency regulation loop, loci of the system dominant eigenvalues as functions of K_d and K_f is presented in Fig. 3.5. It is seen that the first three eigenvalues are highly dependent on these parameters. With an increase

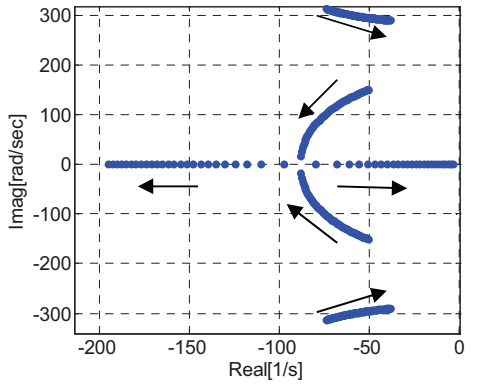

(a)

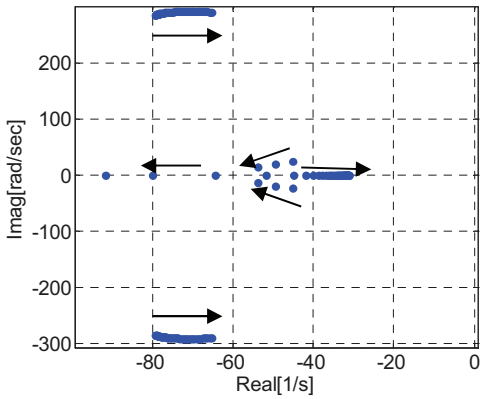

(b)

Figure 3-6. Loci of the first three dominant eigenvalues as a function of frequency regulation loop parameters,(a) $0.0001 < K_{qi} < 0.005$, and (b) $0.001 < \tau_v < 0.02$, $K_{qi} = 0.001$ and $K_q = 0.0005$.

in these parameters, system stability is degraded; whereas eigenvalue 1 is almost constant. Eigenvalue 1 is highly sensitive to the reactive power controller parameters as depicted in Fig. 3.6. Actually, all the dominant poles are affected by K_{qi}; therefore, it is the most influential factor. Accordingly, the design value for K_{qi} is around 0.0005 which results in a damped response with a time-constant less than 0.02 s. To verify the effectiveness of the low-pass filter representing the electrical dynamics of the rotor circuit, loci of the fourth dominant eigenvalues as a function of voltage loop low-pass filter is presented in Fig. 3.6 (b). This figure reveals that by increasing τ_v from 0.001 s to 0.005 s, the damping of the overall system is improved whereas further increment of the cut-off frequency results in lower stability margin. In other words, by proper adjustment of K_{qi} and τ_v the highest damping can be fulfilled.

3.3 Controller Design Guidelines

Using (3.15), the transfer function of the controller is obtained as

$$\frac{\Delta\delta}{\Delta P} = \frac{\xi\omega_n}{s^2 + 2\xi\omega_n s + \omega_n^2} \tag{3.40}$$

where $\omega_n = \sqrt{K_d / J}$ and $\xi = K_f \sqrt{JK_d} / 2$. Consequently, for a desired bandwidth and damping ratio ω_n and ξ, the control parameters can be obtained. The controller natural frequency (ω_n) should be chosen much smaller than the switching frequency (ω_s). Another concern related to ω_n is the system rise time. Usually, the most inner controller bandwidth is selected to be less than 20% of the switching frequency. Unlike real SMs, the rotational momentum and friction factor can be selected equal to values that are not possible for physical electrical machines. The larger J the higher stored energy is; however, to provide this energy, more short-term energy storage or equivalently inertia is required. If sufficient energy storage devices are not available, lower values for J are recommended to have faster response. Equation (3.23) is the main tool for calculating the virtual momentum of inertia to introduce desirable virtual inertia to the grid. The lower the gain K_f, the lower the frequency time-constant is. Nevertheless, it may lead to a steady-state error in the output. If the extra phase angle shift is removed, the transfer function is reduced to

$$\frac{\Delta\omega}{\Delta V_{DC}^2} = \frac{1}{\tau_f s + 1}, \quad \tau_f = \frac{J}{K_f} \tag{3.41}$$

which gives more straight-forward approach to determine the system time-constant and calculate control variables. To calculate frequency recovery time-constant, the voltage reference deviations (ΔV_{DC}^{2*}) are obtained as

$$\frac{\Delta V_{DC}^{2*}}{\Delta\omega} = -K_d\left(\frac{1}{T_i s} + 1\right),\ T_i = 1/K_f \tag{3.42}$$

where T_i is the integrator time-constant. Lower values of K_f results in faster response at the cost of higher steady-state error. T_i can be adjusted by the usual

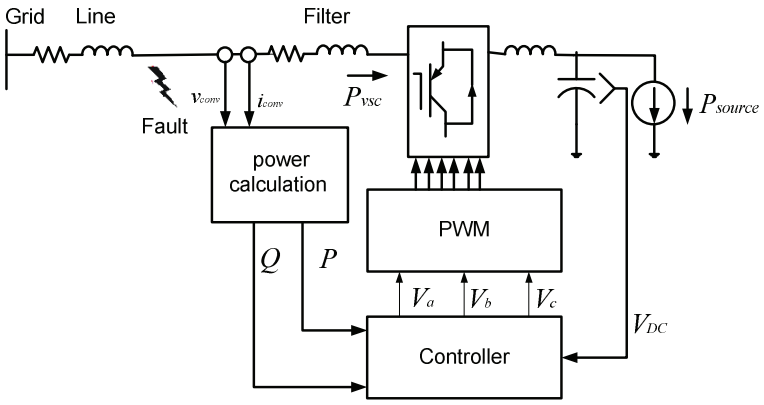

Figure 3-7. Schematic view of the simulated system.

phase margin criterion. The proper values K_q, K_{qi} and τ_v can be obtained by the small-signal analysis to reach satisfactory dynamic performance.

In summary, a two-step design process is proposed. In the first step, the approximate values of the design parameters are determined using (3.40)-(3.42) and (3.24), and in the second step, the proposed small-signal analysis is used for accurate tuning of control parameters.

3.4 Simulation Results

This section presents detailed simulation results of the proposed control system. The simulated system is shown in Fig. 3.7. Simulation studies are carried out in the MATLAB/SIMULINK® environment. Different conditions in both generative and rectification modes are considered to show effectiveness and generality of the controller in all cases. The system parameters are given in Table 3.1. The controller parameters are chosen based on the design process given in Section 3.3 and the small-signal analysis to offer satisfactory performance. The system is simulated under various scenarios of VSC operating conditions. Three scenarios are taken into account; load/generation power change, dc-link voltage reference change, and grid voltage change in both rectifying and inverting modes. The P-Q bus control using flux control topology, shown in Fig. 3.3 (a), is adopted to regulate the reactive power to zero. It is worth mentioning that no PLL is used in the simulation studies.

Table 3-1 The simulated system parameters (SI units)

Parameter	Value
Line inductance	4 mH
Line resistance	0.3 Ω
Grid L-L voltage	220 v
Switching frequency	8kHz
Filter inductance	1 mH
Filter resistance	0.1 Ω
DC side capacitor	2 mF
DC side inductance	0.2 mH
Virtual rotor momentum (J)	10
K_q	0.0001
K_d	1000
K_f	10
K_{qi}	0.00025
τ_v	0.005
ω_c	200 (rad/s)

3.4.1 Rectification Mode

In this section, the transient behavior of the proposed controller topology in rectification mode is presented. The corresponding waveforms are shown in Fig. 3.8. The first event occurs at t= 0.8 s due to a sudden load power increment from 9.0 kW to 12.0 kW. The dc voltage encounters 60V sag due to the load power change; however, the recovery time is less than 0.1 s presenting very fast response. The step change in the preset active power causes some transients in the voltage due to the coupled relatively weak grid parameters, and accordingly, in the reactive power response; however, the load angle is almost constant. In spite of the coupling among active and reactive power components, the controller quickly regulates the reactive power to its pre-set value. At t=2.5 s, the input reactive power reference is varied from 0 to 2.0 kVAr. In this case, the rectifier stars to absorb reactive power from the grid. The controller successfully tracks the new set value within 1s. The effect of reactive power set variation on the dc-link voltage is almost negligible which proves the decoupling between real and reactive power regulation. At t=4 s, the dc voltage reference is reduced to 270 V. The controller tracks the voltage reference accurately within 0.2 s while the reactive power

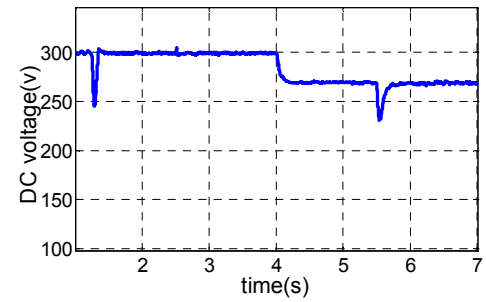

(a)

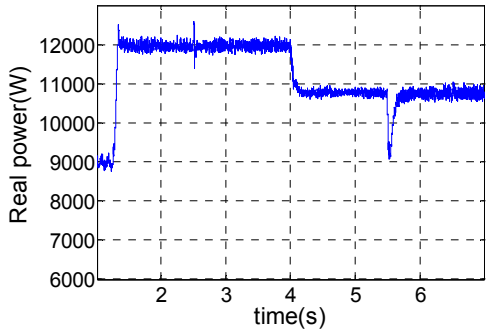

(b)

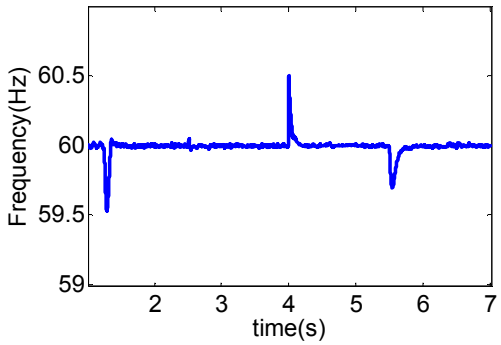

(c)

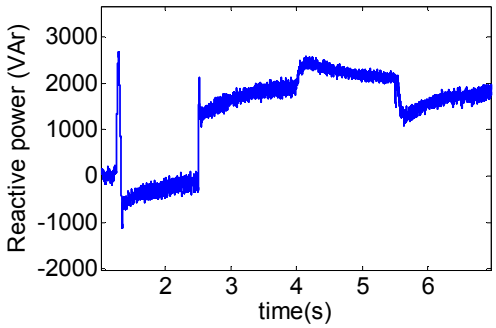

(d)

Figure 3-8. Simulation results for rectifying mode. (a) dc voltage, (b) Real power, (c) Frequency and (d) Reactive power.

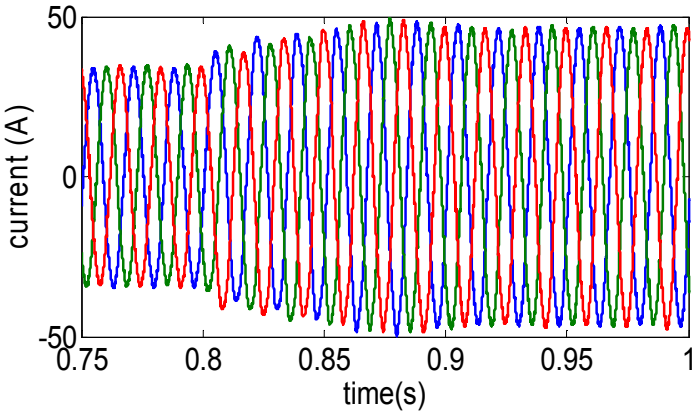

(a)

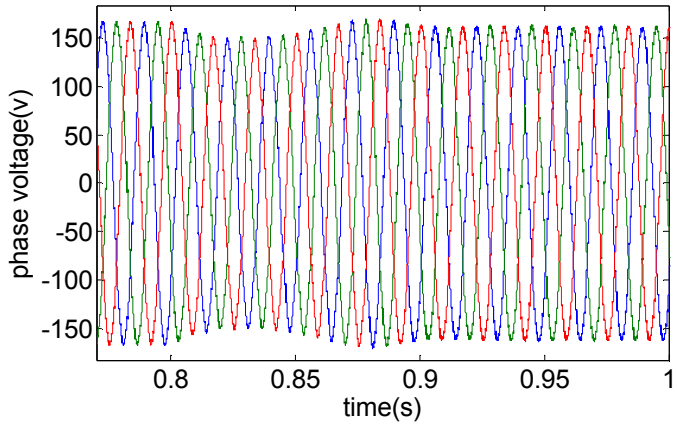

(b)

Figure 3-9. (a) Current and (b) average output filter voltage waveforms for the case of load power increment.

slightly varies. The real power waveforms patterns are close to the dc-link voltage waveforms as $P_{vsc} = V_{DC} I_{DC}$. The validity of the controller has been tested also in the presence of a voltage sag, equals to 0.15 p.u. which occurs at t=5.5 s. In this case, the VSC provides the required reactive power to compensate for the voltage sag and it easily tracks the reference variation. Thus, the converter has the low-voltage ride-through capability to support the system voltage during severe voltage sags.

In order to investigate controller effect on instantaneous current and voltage regulation in transient and steady-state conditions, their waveforms for the case of load current increment from 30 A to 40 A in interval between t=0.77 s to 1 s are

shown in Fig. 3.9. It is clear that both three-phase voltages and currents show smooth and well-damped transient behaviour.

3.4.2 Inverting Mode

The behaviour of the synchronous VSC in the inverting or equivalently the generative mode is studied. It is assumed that a non-dispatchable DG unit is connected at the dc-side where its output power is time variant. As mentioned earlier, since the proposed topology has inherent dc-link voltage regulation functions, it is suitable for non-dispatchable renewable resources where the VSC has to transfer the available power of the source to the grid. The initial voltage of the dc-link voltage in this case is 300V. At t=2 s, the output dc current of the DG unit is increased from 20 A to 30 A. The waveforms of dc-link voltage, real power, frequency for the inverting mode are shown in Fig. 3.10. The dc-link voltage shows a well- damped transient response as well as the real power.

The time-domain responses are in agreement with the eignevalue analysis presented in Section 3.3, which indicates the effectiveness of the designed controller. When a grid voltage sag occurs at t=3.0 s, the controller successfully damps this disturbance with a negligible effect on the real power and dc-link voltage. After the DG output power is increased, the dc-link voltage catches its reference value within 0.08 s and the output power is increased with some minor spikes. At t=4 s, the dc-link voltage reference is reduced to 250 V and the VSC tracks the reference value with highly damped transient response.

3.4.3 Fault-Ride-Through Capability

As mentioned earlier, the proposed controller emulates the characteristics of an SM with frequency and virtual flux regulation. It is well known that one of the main characteristics of SGs is their ability to operate and synchronize themselves with the grid during and subsequent to stable faults. The question is that can the inverter provide fault-ride-through performance like synchronous machine. To investigate this scenario, an unsymmetrical single-phase to ground bolted fault occurs after the filter at t=1.0 s and is cleared at t=1.1 s as shown in Fig. 3.7. The

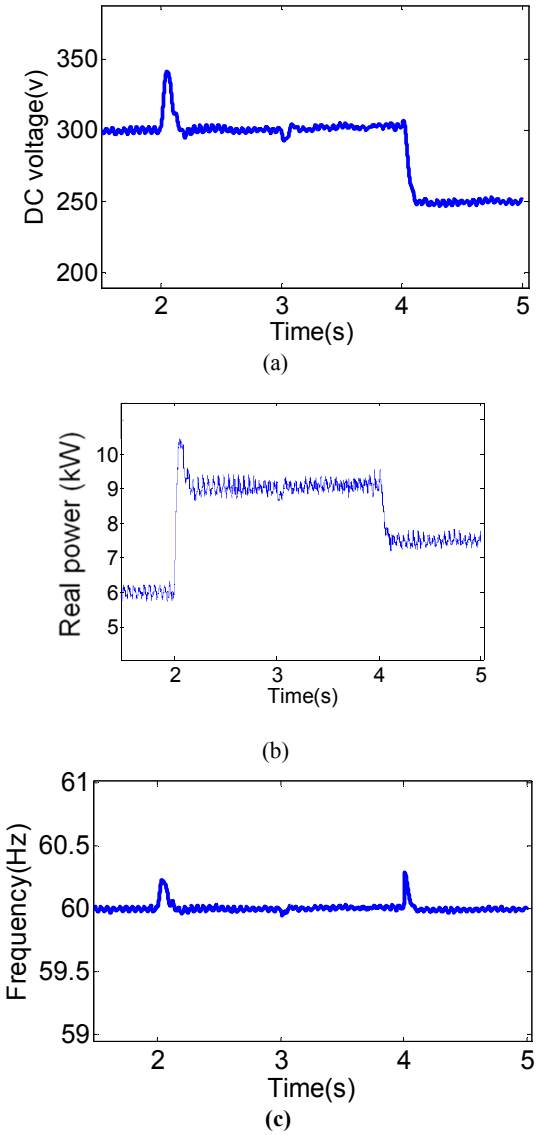

Figure 3-10**.** Simulation results for inverting mode, (a) dc-link voltage. (b) Real power, (c) Frequency.

initial conditions are similar to case A, i.e. dc-link voltage=300 V, reference reactive power=0 VAr and load current (i_{source}) 30A to investigate whether the VSC can override the fault and synchronize itself with the grid during and subsequent to an unsymmetrical fault without PLL. The VSC works in the rectification mode when a fault occurs in phase 'b'. The corresponding waveforms of dc-link voltage, three-phase instantaneous currents and output filter voltage are shown in Fig. 3.11. During the single phase fault, V_{DC} is reduced to

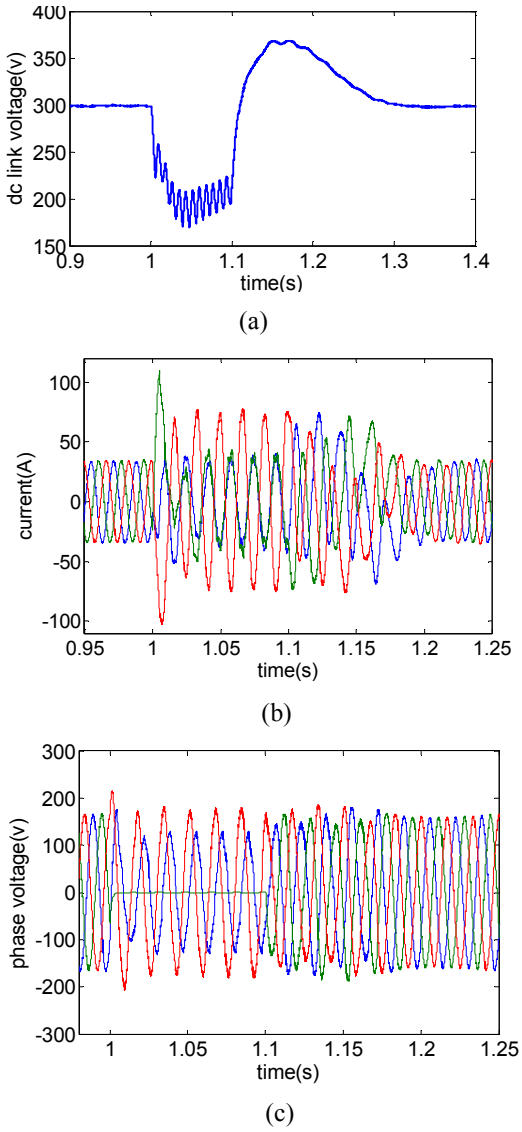

Figure 3-11. The fault-ride-through capability of the synchronous-VSC, (a) dc-link voltage, (b) Instantaneous currents, and (c) Instantaneous output filter voltages.

about 180 V and subsequent to the fault a voltage overshoot of 75 V is observed to charge the capacitor; the controller needs 0.2 s to recover the reference voltage. Also, as it is expected, a second harmonic ripple with frequency 120 Hz appears in the dc-link voltage during the fault to the unbalanced power exchange conditions between the ac- and dc-sides. The amplitude of current in phase 'b' increases to 70 A during the fault whereas in two other phase the current amplitude is almost constant. As expected, the current waveforms are unbalanced

and distorted. The frequency waveform shows that although the frequency is oscillatory during the fault, the controller keeps its synchronism with the grid during the contingency and recovers its initial value after the fault is cleared. This is due the fact that the controller acts like a virtual SG and inherently produces some damping and synchronizing power which enable self-synchronization in various operating conditions. The instantaneous output filter voltage waveform, shown in Fig. 3.11 (c), confirms that phase voltages are kept within acceptable limits during the fault while voltage of phase 'b' is zero due to the short circuit to the ground. Moreover, after the fault clearance phase voltages return to their initial conditions with minimum transients. It is worth noticing that lack of the PLL in this control topology prevents propagation of instabilities which is contributed because of PLL in contingencies such as faults.

3.4.4 Comparison to the Conventional Synchronous dq-Frame Vector Control

Fig. 3.12 shows the diagram of a VSC with conventional vector control system with outer dc-link voltage controller and inner current control loops. The reference d-axis current (i_d^*) is obtained as a function of error of square of dc-link voltage (V_{DC-er}^2) as follows:

$$i_d^* = (k_{p1} + \frac{k_{i1}}{s})(V_{DC-ref}^2 - V_{DC}^2) \tag{3.43}$$

Since the reactive power is proportional to i_q, reactive power control can be realized by i_q control. In both current control channels, to improve dynamic performance and fulfill a faster response, there are two feed-forward loops to directly add the output dq voltage components (v_q , v_d) to the controller voltage commands. Also, to decouple dq-axis dynamics, decoupling terms are added to v_d and v_q, respectively, and final voltage commands are obtained as

$$e_d = v_d^* = (k_{p2} + \frac{k_{i2}}{s})(i_d^* - i_d) - \omega L i_q + v_d \tag{3.44}$$

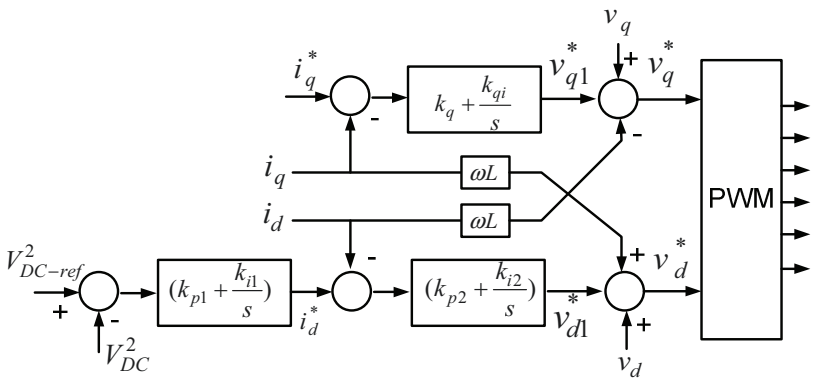

Figure 3-12. Schematic of the vector control.

Table 3-2 The Vector Controller Parameters

Parameter	Value [SI Units]
K_{p1}	-0.088
K_{i1}	-0.5
K_{p2}	20
K_{i2}	600
K_q	20
K_{qi}	600
Switching frequency	10 kHz

$$v_q^* = (k_{qp} + \frac{k_{qi}}{s})(i_q^* - i_q) + \omega L i_d + v_q \tag{3.45}$$

The controller shown in Fig. 3.12 is implemented to compare its features with the proposed synchronous-VSC. The controller parameters are given in Table 3.2. The connecting circuit parameters are the same as the synchronous-VSC case. The parameters are tuned optimally for a 10 kHz switching frequency to achieve adequate performance. A PLL is necessary to observe grid frequency and angle and transform voltage and current variables from abc to dq frame and vice versa. Two scenarios similar to synchronous-VSC case-studies are taken into account in the rectifying mode. In the first scenario, the load current is increased from 30 A to 40 A at t=1.5 s and a single phase-to-ground fault happens after the filter at t=2.8 s. The waveforms of V_{DC} and VSC's frequency for the case that the load current is increased from 30 A to 40 A are presented in Fig. 3.13. As can be seen,

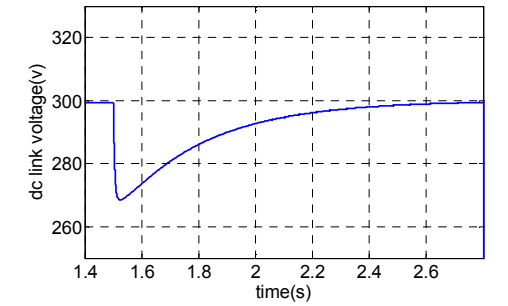

(a)

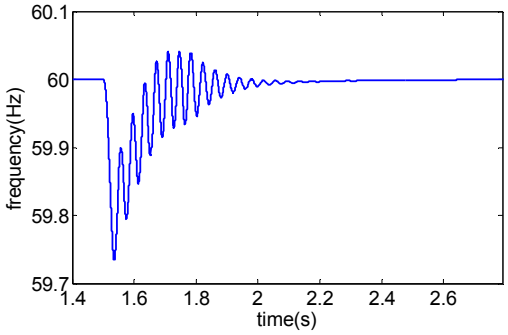

(b)

Figure 3-13. System responses of the vector control for the case of the load power increment, (a) dc-link voltage and (b) VSC's frequency.

the settling time for the synchronous-VSC is about 0.1 s whereas it increases to more than 1 s in the conventional vector control, therefore the controller shows slower response with respect to the synchronous-VSC. However, the voltage undershoots in synchronous-VSC and vector control are limited to 52 V and 32 V, respectively representing lower voltage drops for the vector control. The VSC's frequency shows oscillatory behaviour with slow recovery time due to grid voltage oscillations which are reflected to the PLL dynamics. The situation becomes worse in weaker grids, where coupling between grid, PLL and converter dynamics increases and threatens converter stability. The vector controller does not offer direct frequency control, and its frequency dynamic is complex and unknown. In fact, overall PLL, converter controller and grid parameters determine the frequency response during transients and the controller does not have frequency regulation capability. On the contrary, the proposed synchronous-VSC has predictable and known frequency dynamics. Fig. 3.14

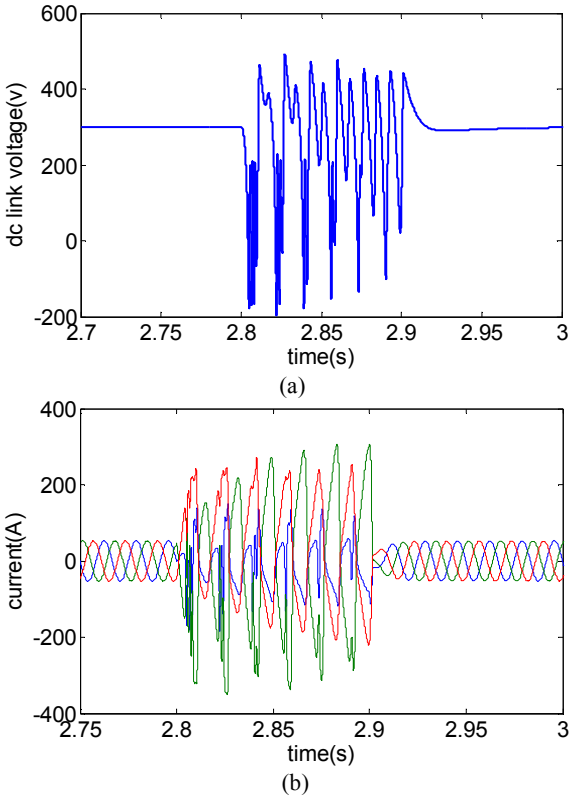

Figure 3-14. System response during the fault using the vector control, (a) dc-link voltage and (b) instantaneous currents.

shows the vector control response subsequent to the single-phase-to-ground fault occurs after the filter. The dc-link voltage and three-phase current variation for this case are shown in Fig. 3.14 which clearly shows that the vector control is unstable during the fault and cannot override the fault. Actually, instability is contributed because of both the controller and PLL.

3.4.5 Virtual Torque Control Strategy

In the previous sections, we presented the results for the direct dc-link voltage controller. In this section the practicability and performance of the virtual torque controller shown in Fig. 3.2 (a) is briefly studied. The parameters of the frequency loop are as follows: ($K_f = 1000$, $K_t = 30$, $K_{ti} = 2$, J=10). As shown in Fig. 3.2 (a), in this case based on the frequency error the virtual torque reference is obtained and the virtual torque control loop adjust the dc-link voltage in such a way damping

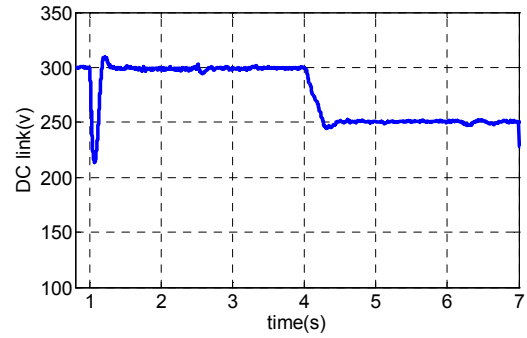

(a)

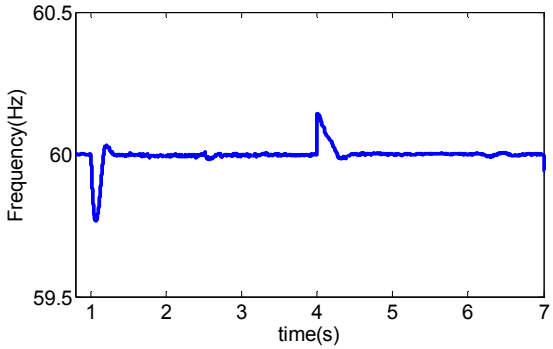

(b)

Figure 3-15. The system waveforms for the virtual torque controller,(a) dc-link voltage and (b) VSC's frequency.

and synchronizing torques are generated within the controller during transients similar to SMs. The parameters of the simulated system and the virtual torque control loop parameters are the same as the previous case. Also, the same scenarios of section 3.4.1 are applied to the system. Fig. 3.15 shows the dc-link voltage and frequency variations for this case. It is seen that the controller easily tracks the dc-link voltage reference variations and proves its practicability. Also, this controller offers good real and reactive powers decoupling capability as the reactive power reference is altered at t= 2.5 s, there is no observable change in the dc-link voltage. The system performance indexes in terms of response speed and frequency regulation are similar to the direct dc- link voltage controller with more under and overshoot in the dc-link voltage but less under and overshoot in the frequency. However, the designer has more degree of freedom to adjust the controller parameters in the virtual torque controller.

3.5 Experimental Results

For further investigation of the proposed controller, extensive experimental tests are conducted. Key results are presented in this section. A Semikron Semistack intelligent power module which includes gate drives, six insulated gate bipolar transistors (IGBTs), and protection circuit, is used to implement a bi-directional VSC. The VSC is interfaced to a 120V, 60Hz, utility grid via an L-filter with inductance 1.2 mH and resistance 0.1 Ω, and a transformer with a feeder modeled by an inductance and resistance are 2.4 mH and 0.2 Ω, respectively, which represent a weak grid for the low-voltage setup with *X/R* ratio of 4.5. Therefore, the test conditions resemble typical conditions that can be found in distribution systems with DG units or active loads. The low *X/R* ratio increases the coupling among the active and reactive power components, however, the proposed controller yields very good control performance under such practical test conditions. The dc-link capacitance is 2.0 mF. The dSPACE1104 control system is used to implement the proposed control scheme in real-time. The pulse-width modulation algorithm is implemented on the slave-processor (TMS320F240-DSP) of the dSPACE controller. The VSC inductor currents are measured by HASS-50-S current sensors whereas the voltages are measured by LEM-V-25-400 voltage sensors. The converter is interfaced to a dSPACE1104 control card via a CMOS/TTL interfacing circuit. The dSPACE1104 interfacing board is equipped with eight digital-to-analogue channels and eight analogue-to-digital channels to interface the measured signals to/from the control system. The software code is generated by the Real-Time-WorkShop under a Matlab/Simulink environment. The switching frequency is 10 kHz and the voltage and currents are measured after the filter. As the synchronous VSC automatically synchronizes itself with grid similar to an SM, no PLL is employed after initial synchronization. The control system parameters are selected using the design guidelines and small-signal analysis provided in Sections 3.3 and 3.4. Fig. 3.16 shows a view of the experimental setup, whereas Fig. 3.17 shows a circuit diagram of the laboratory setup.

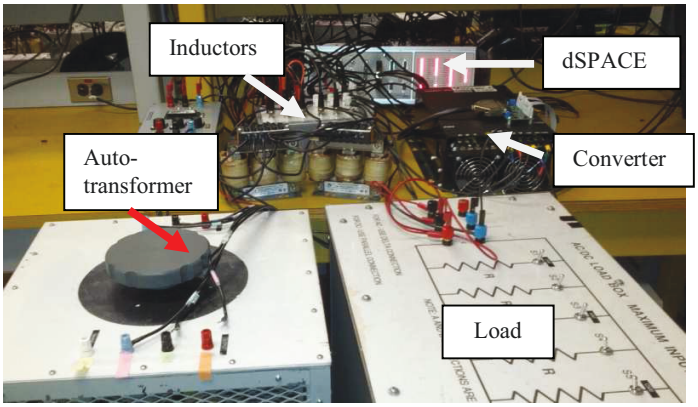

Figure 3-16. View of the experimental setup.

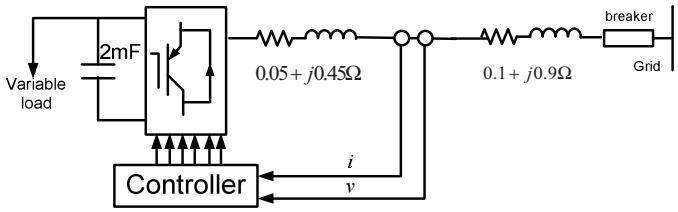

Figure 3-17. The experimental setup parameters.

Experimental tests involve load power increase and decrease, grid voltage variation and dc-link voltage reference variations. The sequence of the events is as follows: first, the VSC operates as a rectifier is in steady-state, then the load power is increased from 0.5 p.u. to 0.8 p.u. In the second step, the load power is reduced to its initial value. Next, grid voltage is reduced by 0.2 p.u., and finally the dc reference-voltage is varied to 0.8 p.u. of its nominal value. The reactive power reference is set to zero to achieve a unity power factor interface.

In this case, the load power is increased from 0.5 p.u. to 0.8 p.u at t=0.9 s. Figs. 3.18 (a), (b) and (c) show the dc-link voltage, frequency and instantaneous reactive power waveforms. The waveforms of V_{DC} and frequency exhibit similar dynamics, which shows high coupling between the dc-link voltage and frequency; the latter controls the active power via the load angle. The recovery time is less than 0.2 s; however, the reactive power recovery time is higher which is due to the slower time-constant of the reactive power regulation loop. The measured responses are in line with the theoretical analysis presented in Section 3.3. The dc-link voltage is dropped slightly to inject power to the load. After this

disturbance, the load power is reduced to its initial value. It is worth mentioning that in both cases, the effect of load power variation on the reactive power is not noticeable. The magnified views of the dc-link voltage and frequency indicate the smooth control performance of the proposed controller without saturating the VSC.

In the second scenario, a sudden 20% voltage dip in the grid voltage is applied via the connecting transformer to test the low-voltage ride-through capability of the proposed synchronous VSC. Fig. 3.19 verifies that the controller is robust against grid voltage disturbances. The VSC easily converges to the rated dc-link voltage and frequency only after 0.5 s. However, the transition in the reactive power indicates a 30 VAr dip in the reactive power subsequent to grid voltage disturbance as it is more dependent on the grid voltage amplitude. These plots confirm the low-voltage ride-through ability of the controller. In the next test, the voltage reference is changed from 1.0 p.u. at t=0.8 s to 0.8 p.u. at t=1.8 s as a ramp function. The corresponding voltage waveform is shown in Fig. 3.20, which confirms the tracking ability of the proposed controller with damped transient response.

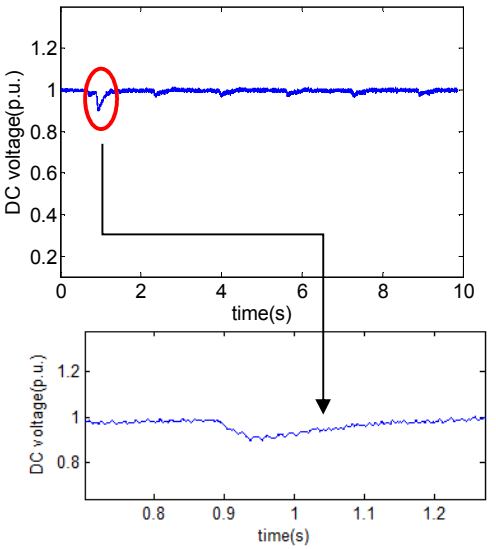

(a)

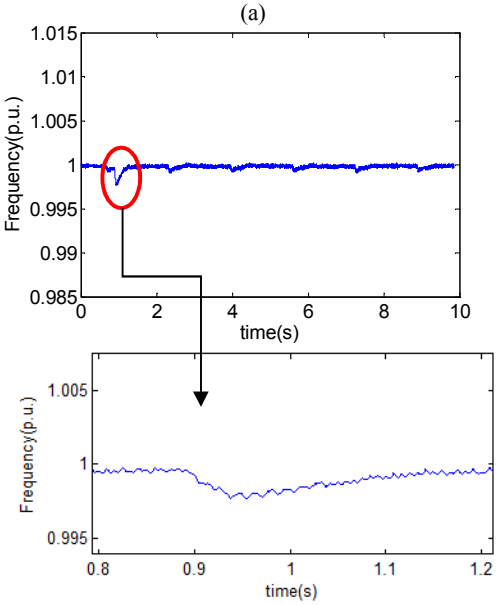

(b)

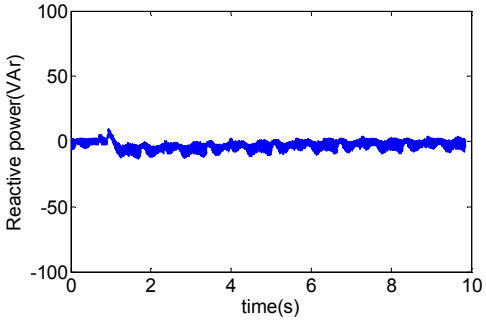

(c)

Figure 3-18. Experimental results for the case of load increment; (a) dc voltage (p.u.), (b) Frequency and (c) Reactive power.

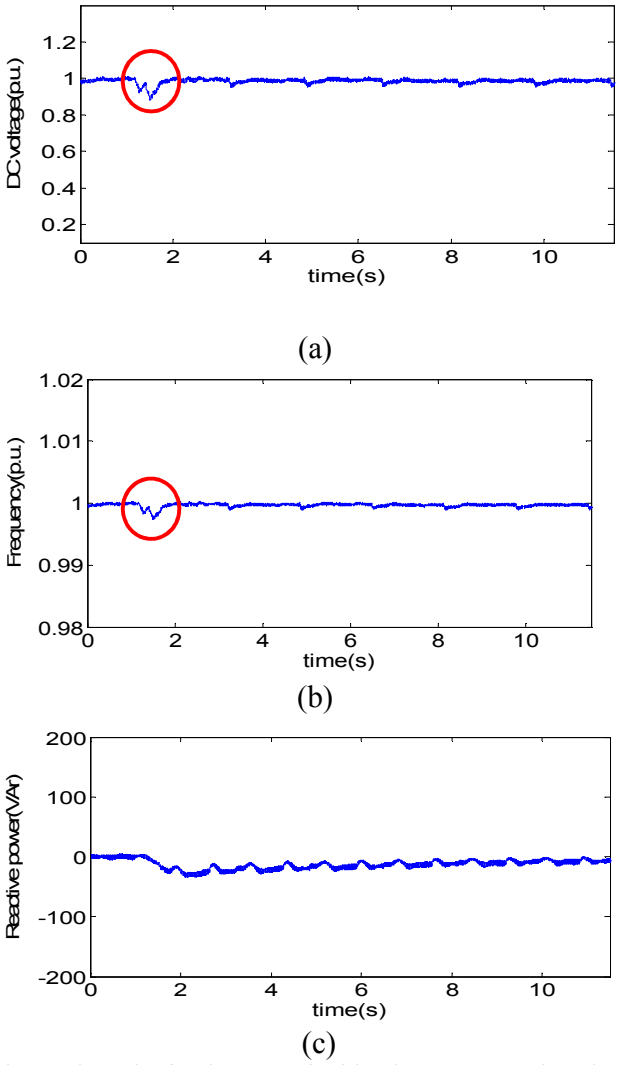

Figure 3-19. Experimental results for the case of grid voltage sag; (a) dc voltage, (b) Frequency, (c) Reactive power.

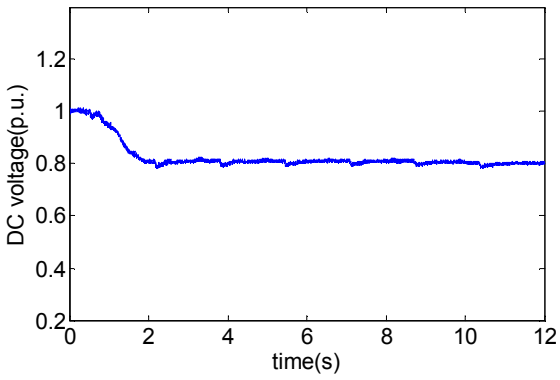

Figure 3-20. DC-link voltage tracking performance.

Chapter 4 General Interface for Power Management of Micro-Grids Using Nonlinear Cooperative Droop Control[3]

This chapter proposes a general control strategy, for both converter- and synchronous-machine-based DG units in MGs, based on a combined angle-frequency droop controller with improved dynamic performance. A supplementary nonlinear controller is designed to compensate nonlinearities of load angle, frequency and power. The controller design has two steps; in the first step the parameters of the linear cooperative droop control are adjusted and in the second step a supplementary nonlinear controller is designed according to the linear controller and the connected interface parameters to ensure large signal stability of the overall MG in both grid-connected and islanded modes. Ability to work in both modes without a need for reconfiguration and parameters change, steady state constant frequency operation, accurate power sharing and stable operation subsequent to out-of-phase auto reclosing are some other advantages of the proposed nonlinear cooperative droop controller.

4.1 Proposed Controller Scheme and Design Process

As mentioned in chapter 2, the most adopted approach for the power sharing in an islanded MG is frequency and voltage drooping in which the frequency (ω) and voltage amplitude of a DG unit are obtained as

$$\omega = \omega_0 - mP \tag{4.1}$$

$$E = E_0 - nQ. \tag{4.2}$$

The frequency and voltage droops form a communication-free medium to share real and reactive power among DG units proportional to their power capacities. In fact, frequency and voltage set-points are used as global virtual communication signals between DG units. The droop constants can be selected as

[3] This work is published in *IEEE Transactions on Power Systems* [104].

$$m = \frac{\Delta\omega_{\max}}{P_{\max}} \tag{4.3}$$

$$n = \frac{\Delta E_{\max}}{Q_{\max}}. \tag{4.4}$$

It is well understood that if droop coefficients are increased in the autonomous mode, power sharing accuracy is improved at the cost of poor frequency and voltage regulation [5], [18]. It is also well known that higher droop gains adversely affect system stability and there are some limits to ensure performance and stability indicating some inherent trade-off between power sharing accuracy, power quality, transient response, and system stability. An alternative for real power sharing is angle drooping. Unlike SGs, the output power angle of a VSC can be changed instantaneously without change in frequency; and frequency is employed as a medium for angle tuning in conventional SGs. Therefore using the angle droop is another way to share real power. As a matter of fact, since real power is controllable through load angle, there is no need for vary frequency to regulate power. The governing equation for the angle drooping is as follows:

$$\delta = \delta_{set} - dP. \tag{4.5}$$

The angle droop provides a constant frequency operation which is the main benefit; however, it suffers from poor power sharing and low stability margin. This is more pronounced when the load angle is large. To achieve accurate load sharing, a centralized control strategy using communication infrastructure is developed in [75] to adjust the load angle preset values online. However, it is not of high interest to embed communication infrastructure in an autonomous control where its main goal is MG power management based on local information without data exchange with a centralized controller. Moreover, by increasing the angle droop gain or output power, a DG unit may be easily driven into instability [41].

To overcome the aforementioned problems, a comprehensive control topology is presented in this chapter. All control and power management requirements of an MG are augmented in one general control scheme. It involves angle, frequency and power loops and consequently benefit from their advantages simultaneously. Constant frequency operation and accurate power sharing can be realized by

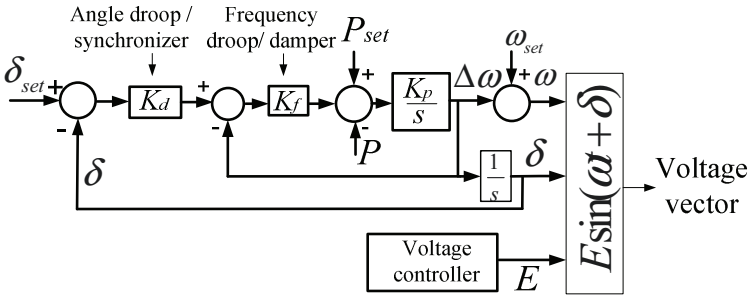

Figure 4-1. Hybrid angle-frequency droop control.

combined angle-frequency drooping while large-signal stability of the system is achieved by a supplementary nonlinear controller.

Fig. 4.1 represents the block diagram of the overall power manager-controller proposed for a VSC-based DG unit. The controller is implemented in polar coordinates and directly regulates the output voltage vector amplitude and angle. As it is seen from Fig. 4.1, the frequency control loop has two cascaded angle and frequency loops which determine the reference power; and a power synchronization loop which adjusts the VSC output frequency based on the reference and actual active powers. This power synchronizing loop introduces virtual inertia for frequency as it mimics rotor momentum of inertia of a conventional SG [104]. The angle and frequency loops play two various roles; first, they behave like dampers to mitigate angle and frequency oscillations. Second, they provide synchronizing power. The damping and synchronizing power components [103] are given by

$$Damping\ power = \Delta P_{damp} = -K_f \Delta\omega \tag{4.6}$$

$$Synchronizing\ power = \Delta P_{synch} = -K_f K_d \Delta\delta. \tag{4.7}$$

The synchronizing power attempts to return load angle to its equilibrium point subsequent to transients while damping power is responsible for preserving frequency stability and mitigating frequency oscillations. Hence, the proposed topology offers more damped transient behavior as compared to the conventional frequency or angle-droop controllers because of these extra loops. In autonomous mode, K_d and K_f act as angle and frequency droops while the angle droop is the main power sharing loop.

The frequency dynamics is the same as in an SG, in which the rotating shaft is resisted by a viscous damping proportional to the frequency deviation and used as damping power. In the proposed topology, an extra damping (K_d) exists, which is responsible to damp angle oscillations, therefore, the controller offers better angle stability. The augmented dynamic equation is given by

$$\frac{d\Delta\omega}{dt} = -K_p K_f(\omega - \omega_{set}) - K_d K_p K_f(\delta - \delta_{set}) - K_p(P - P_{set}) \tag{4.8}$$

The relationship between the VSC frequency and the load angle is

$$\frac{d\delta}{dt} = \Delta\omega \tag{4.9}$$

As mentioned, in autonomous mode, two cascaded droop loops exist which cooperate with each other to share active power and also damp angle and frequency oscillations. The first angle droop loop generates the frequency reference for the second frequency droop loop according to the angle error

$$\Delta\omega_{set} = K_d(\delta_{set} - \delta) \tag{4.10}$$

Based on this frequency set-point, the frequency droop determines the power reference

$$\Delta P_{set} = K_f(\Delta\omega_{set} - \Delta\omega) \tag{4.11}$$

In stable steady-state conditions, the input to the integrator is zero. Thus, it is followed that

$$P = P^* - K_f K_d \delta - K_f \Delta\omega \tag{4.12}$$

where $P^* = P_{set} + K_f K_d \delta_{set}$. The angle and frequency drooping gains are equal to $K_d \times K_f$ and K_f , respectively. From (4.12) it is concluded that K_f is proportional to the inverse of frequency droop (m) and $K_d \times K_f$ is equal to the inverse of the angle droop (d).

There are different approaches for the adjustment of δ_{set} . Actually, in the grid connected mode, infinite combinations of δ_{set} and P_{set} exist to inject a specific power to the grid. Load flow or optimization processes can be used to find the optimal values of δ_{set} and P_{set} to fulfill an objective function. A multi-objective

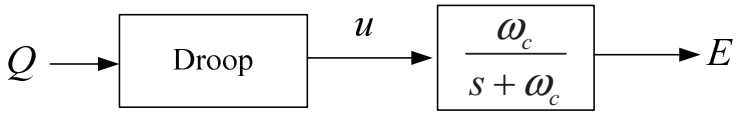

Figure 4-2. The voltage controller.

function can be adopted for the optimization aiming at goals such as improvement of system stability (small signal and large signal), load sharing accuracy can be defined. Once the optimum set points of the angle and power loops are calculated, they are set constant in a system without communication links. Load flow is another approach to adjust the angle set points which is widely discussed in [75]. However, it needs a communication link to coordinate the angle set-points as a function of loads in the power system. It should be noted that in this case, a designer has one more degree of freedom to select controller parameters as compared to synchronous converters presented in chapter 2, since in the synchronous converters the set point of the frequency loop is set to 60 Hz whereas in this model the angle set-point can be adjusted any value optimally.

The adopted topology for voltage amplitude control is shown in Fig. 4.2. It includes a voltage versus reactive power droop and a low-pass filter. The voltage drooping is a tool to share the MG reactive power among DG units proportional to their power capacities. The voltage amplitude is obtained by processing the drooped voltage command by a low-pass filter. Actually, the existence of the low-pass filter presents additional dynamics for the voltage and resembles the flux decay behavior of an SG. As it will be shown in the next section, this voltage dynamics is useful during nonlinear controller design. It is worth noticing that the low-pass filter helps to eliminate high-order harmonics generated due to VSC switching behavior.

4.2 Supplementary Nonlinear Controller Design

To design the supplementary nonlinear controller, the state-space model of the system is required. The supplementary nonlinear controller is illustrated in Fig. 4.3. It is seen that this controller generates an additional signal for the linear

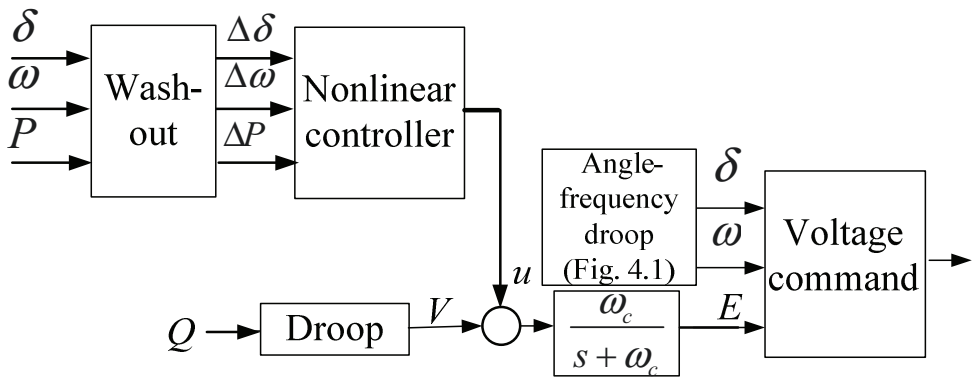

Figure 4-3. The nonlinear supplementary controller.

controller of the voltage loop. The concept of supplementary voltage control has been originally derived from the power system stabilizer [103] in which an additional signal is added to the rotor excitation reference voltage to improve angle stability under system disturbances. In its conventional version, the power system stabilizer adopts power deviations as its input and it is processed by a lead-lag compensator to obtain the supplementary voltage-reference [35]. By proper tuning of the lead-lag controllers at a given operating point, angle stability can be enhanced; however, since the relation between the load angle and power is nonlinear, the linear controller may fall-short to ensure system stability in all operating points, particularly under large-signal transients. Similarly, the load-angle equation is highly nonlinear and in an MG system, the nonlinearity is more pronounced because there is no base power. Therefore, DG output power and load angle may vary in a wide range. In this chapter, the concept of power system stabilizer is adopted for VSCs where a nonlinear controller is designed for to assure large-signal stability of each DG unit. The load angle, frequency and power are selected as state-space variables and the DG state-space model is given by

$$\dot{x}_1 = x_2 \tag{4.13}$$

$$\dot{x}_2 = a_1 x_1 + a_2 x_2 + a_3 x_3 \tag{4.14}$$

$$\dot{x}_3 = u_f + E\frac{V_L}{X} x_2 \cos x_1 - \omega_c x_3 + \gamma \tag{4.15}$$

where u_f is related to the control input u by,

$$u_f = u\omega_c \frac{V_L}{X} \sin x_1 \tag{4.16}$$

and

$a_1 = -K_p K_f K_d$, $a_2 = -K_f K_p$, $a_3 = -K_p$, $[x_1, x_2, x_3] = [\Delta\delta, \Delta\omega, \Delta P]$.

The term γ is added to (4.15) to account for system uncertainties including local and inter-area ones. This augmented disturbance rejection yields a more robust system and is estimated during nonlinear controller design using adaptive estimation technique. The adaptive back-stepping technique is employed to design the nonlinear controller and overcome system uncertainties. The control design procedure is based on the following steps.

Firstly, the frequency reference (x_{2ref}) is calculated to stabilize the load angle δ. The Lyapunov function is selected as

$$V_1 = \tfrac{1}{2} x_1^2. \tag{4.17}$$

To stabilize x_1, $\dot{V}_1$ should be negative definite. Now, if

$$x_{2ref} = -k_1 x_1 \quad k_1 > 0 \tag{4.18}$$

then

$$\dot{V}_1 = -k_1 x_1^2 + x_1 e_2 \tag{4.19}$$

where $e_2 = x_2 - x_{2ref}$. According to (4.19), there is no guarantee that $\dot{V}_1 < 0$. In the next steps, by proper selection of x_{3ref}, $\dot{V}_1$ is made negative definite [85, 86].

To stabilize the frequency dynamics, x_{3ref} is chosen according to the Lyapunov function

$$V_2 = V_1 + \tfrac{1}{2} e_2^2. \tag{4.20}$$

The derivative of V_2 along its trajectory is

$$\dot{V}_2 = \dot{V}_1 + e_2 \dot{e}_2 \tag{4.21}$$

where $\dot{e}_2 = \dot{x}_2 - \dot{x}_{2ref}$. Using equations (4.14) and (4.18), it follows that

$$\dot{e}_2 = [k_1 k_p k_f - k_p k_d k_f - k_1^2] x_1 + (k_1 - k_p k_f) e_2 + a_3 (e_3 + x_{3ref}) \tag{4.22}$$

If

$$x_{3ref} = c_1 x_1 + c_2 e_2 \tag{4.23}$$

where

$$c_1 = \frac{(1 - k_1(-a_2 + k_1) + a_1)}{a_3} \tag{4.24}$$

$$c_2 = -\frac{(k_1 + k_2 + a_2)}{a_3}, \quad k_2 > 0 \tag{4.25}$$

then $\dot{V}_2$ becomes

$$\dot{V}_2 = -k_1 e_1^2 - k_2 e_2^2 + a_3 e_2 e_3 \tag{4.26}$$

From (4.26), it is concluded that system (4.13)-(4.15) still is not fully stabilized and hence u_f should be designed in the next step to make $\dot{V}_2$ negative definite.

Finally, to obtain the control input u_f, the Lyapunov function is defined as

$$V_3 = V_2 + \tfrac{1}{2} e_3^2 + \tfrac{1}{2} \rho(\gamma - \hat{\gamma})^2 \tag{4.27}$$

where γ and $\hat{\gamma}$ are the lump-sum uncertainty and its estimated value, respectively, and ρ is the adaptation law gain. To ensure that $\dot{V}_2 < 0$, the Lyapunov function V_3 involves V_2, global stability of frequency is not confirmed, so in this step u_f is obtained in such a way that it guarantees stability of the Lyapunov functions V_2 and V_3 simultaneously. Now, consider the dynamics of

$$\dot{e}_3 = \dot{x}_3 - \dot{x}_{3ref} \tag{4.28}$$

$\dot{x}_3$ is given by (4.15) and

$$\dot{x}_{3ref} = Ax_1 + Be_2 + Ce_3 \tag{4.29.a}$$

$$A = K_f - k_1^2 K_f + k_1 K_d K_f - 2k_1 K_p + \frac{k_1^3}{K_p} - \frac{k_2}{K_p}, \tag{4.29.b}$$

$$B = (k_1 + k_2 - K_d) K_f + \frac{1 - k_1^2 - k_2^2 - k_1 k_2}{K_p}, \tag{4.29.c}$$

$$C = -k_1 - k_2 + K_p K_f. \tag{4.29.d}$$

Thus, $\dot{V}_3$ is given by

$$\dot{V}_3 = -k_2 e_2^2 + \tag{4.30}$$
$$[u_f$$
$$-(A + k_1 \frac{EV_L}{X}\cos x_1)x_1$$
$$-(B - \frac{EV_L}{X}\cos x_1 - a_3)e_2$$
$$-Ce_3 + \gamma]e_3$$
$$-\rho(\gamma - \hat{\gamma})\dot{\hat{\gamma}}.$$

If the adaptation law is chosen as

$$\dot{\hat{\gamma}} = \frac{1}{\rho} e_3 \tag{4.31}$$

and the control input is selected equal to

$$u_f = (A + k_1 \frac{EV_L}{X}\cos x_1)x_1 \tag{4.32}$$
$$(B - \frac{EV_L}{X}\cos x_1 - a_3)e_2$$
$$+(C - k_3)e_3 - \hat{\gamma} \qquad k_3 > 0$$

then $\dot{V}_3$ is given by

$$\dot{V}_3 = -k_1 x_1^2 - k_2 e_2^2 - k_3 e_3^2. \tag{4.33}$$

Since $\dot{V}_3$ is negative definite, global stability of the system (4.13-4.15) is confirmed. This globally asymptotically stability means that system is stable during large-signal transients regardless of the operating point.

4.3 Discussion about Practicability of the Proposed Controllers

As shown in Fig. 4.3, the proposed controller has two main parts which are 1) a linear cooperative angle-frequency droop control, and 2) a supplementary nonlinear controller aiming at stabilizing the load angle dynamics during large-angle transients. The only inputs to the linear controller are real and reactive powers which are directly available at the output of the converter. Another advantage of the controller is that the frequency and angle signals are internally available. Moreover, the controller has internal power synchronization and damping dynamics (as defined in (4.6) and (4.7)), which provide inherent synchronizing during steady-state and automatically tracks grid frequency and angle deviations, similar to a synchronous machine. This shows that the linear

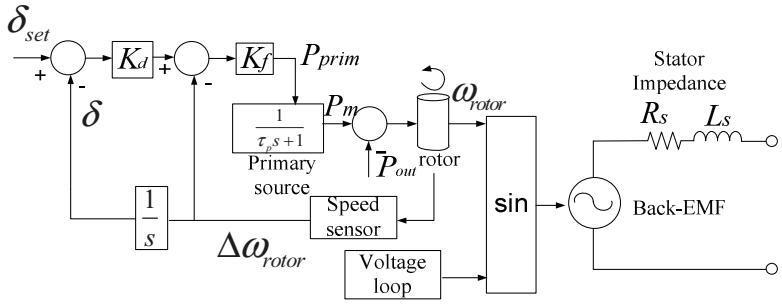

Figure 4-4. SG control with angle-frequency control.

controller can be easily implemented and a supplementary nonlinear signal is generated using equation (4.32). To calculate the supplementary control input of the nonlinear controller, according to (4.32), the perturbations of signals of load angle, frequency and output power ($\Delta\delta, \Delta\omega, \Delta P$) are required. Toward this, a wash-out filter is employed which adopts angle, frequency and power as input and detects their perturbation. The VSC frequency is available internally and output power can be easily calculated using the measured output current and voltage of the VSC. Using the calculated state variables $\Delta\delta, \Delta\omega, \Delta P$, the control law can be easily implemented in a commercial-grade digital-signal processor (DSP). In other words, all the required variables and control laws can be directly calculated using local information without a need for complex operations or communication. Other practical aspects, such as the presence of conventional SGs in the MG system and noise sensitivity are addressed in the following subsections.

4.3.1 Application of the Cooperative Angle-Frequency Droop to SGs

As mentioned earlier, one of major advantages of the proposed controller is mimicking the behavior of SGs. Accordingly; the proposed angle-frequency droop can be extended to SGs to ensure nominal steady-state frequency operation whereas power sharing is also achieved.

The regular approach for power sharing among SGs is frequency versus real power and voltage versus reactive power drooping. In the regular frequency drooping of SGs, as the output power of SG is increased, a permanent offset in

frequency occurs. Apparently, the droop control is an external control function and is not part of an SG behavior. The static equation of an SG is given by

$$P_{prim} = P_{SG}^{*} - K_f \omega_{rotor} \tag{4.32}$$

where P_{SG}^{*} is the reference power of the primary source of the SG. Usually, the primary source model is presented by a first-order transfer function [76]. Similar to VSCs, it is possible to deploy the load angle as drooping variable. In this case, the load angle of the SG is directly regulated such that the desirable output power is achieved without permanent frequency offset. In a similar manner, cooperative load angle-frequency is an alternative for power sharing in SGs. In this case, the input power to the SG is governed by

$$P_{prim} = P_{SG}^{*} - K_f \Delta\omega_{rotor} - K_d K_f \delta \tag{4.33}$$

Fig. 4.4 presents the implementation of cooperative droop control for an SG. The perturbation of the SG rotor speed $\Delta\omega$ is obtained by processing the measured rotor speed. The load angle is calculated by integration of $\Delta\omega$. Since the main drooping is applied to the load angle, the frequency is maintained constant after the load angle is adjusted. The primary power is applied to the primary source which can be a diesel generator as it generates the reference power with a delay.

4.3.2 Effect of Measurements Noise on the Controller

Another issue that the controller may face is the presence of noise in the measured signals. If the proposed cooperative angle-frequency droop control is adopted for VSCs, since only the real and reactive powers are measured through sensors and filtered using a low-pass filter to remove switching effects and obtain the average power, effects of high frequency noises on the powers are automatically eliminated by the low-pass filter. However, if the cooperative angle-frequency droop controller is applied to a real SG, the frequency is not internally available and a speed sensor is necessary to measure the rotor speed. In this case, noise superimposed on the measured speed signal may affect the controller performance because K_f has usually large values; therefore noise effect is intensified and appears in the reference power of the SG. It is worth noticing

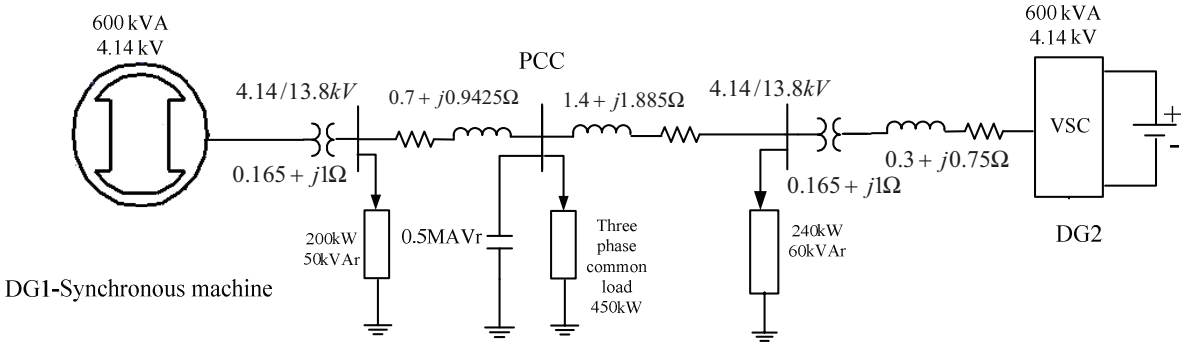

Figure 4-5. The configuration of the system A.

that K_f is equal to the inverse of m. Since in the conventional frequency droop method, m has small values, K_f usually has large size, thus its effects on the system operation should be investigated. The positive point is the existence of a large rotor with high momentum of inertia which acts as a low-pass filter, which in turns filters out the impact of high frequency noises. In other words, when a white noise with zero average appears in either the input power or measured frequency, its effect is highly attenuated by the rotor dynamics.

4.4 Case Studies

To evaluate the validity and effectiveness of the proposed controller, it is applied to two different, which are simulated under the MATLAB/SIMULINK environment. The first system includes SG and VSC as shown in Fig. 4.5 and the controllers' parameters are given table 4.1. The first system consists of a conventional SG and a VSC-interfaced DG unit. The cooperative droop control without the supplementary nonlinear controller is applied to both units, where power sharing accuracy, constant frequency operation and system transient behavior are investigated. Both units supply a local load and a common loadthrough a transformer and the connecting lines. The SIMULINK-based average-model of a VSC and detailed SG model are adopted. The loads consume

Table 4-1 Parameters of the Two-DG Microgrid shown in Fig. 4.5.

Parameter	DG1	DG2
Line-line voltage (V)	4140	4140
Stator inductance (L_s)	2mH	-
Stator resistance (R_s)	0.2 Ω	-
K_d	10	10
K_f	1e5	1e5
K_p	-	0.1
Rotor momentum of inertia	10	-
Voltage slope (n)	1e-3	1e-3

their rated real and reactive powers at the rated voltage. In this case, the goal is to investigate the practicality of the cooperative droop for SGs and VSCs in various conditions. In the second system, the MG has three DG units and is connected to a medium-voltage level power system at the PCC through matching transformer. A three-phase matching/isolation transformer is also installed in each DG unit. Each DG has a local load. At the PCC, a sensitive load exists. The MG should supply both sensitive and local loads without interruption. Four scenarios are taken into account; disconnection and reconnection of one unit during islanding, grid restoration and transition to islanding. Static power sharing performance of the MG during islanding is also studied. It is noticeable that in all conditions, the controller topology and parameters are not changed.

4.4.1 Application of Cooperative Droop to the MG with Conventional SG and VSC

The simulated system in this case is shown in Fig. 4.5 and it involves two units. The system parameters are given in Table 4.1. The cooperative droop is applied to both the SG and VSC to evaluate its practicality for different types of generation units. Two controller topologies are taken into account to study effect of frequency restoration; the first controller involves both angle and frequency droops whereas in the second controller, only the frequency loop exists and the angle drooping is removed ($K_d = 0$), (i.e. only frequency drooping is enabled). Initially, DG units supply a common 180 kW load. At t=4 s the common load power is increased to 450 kW and at t=5.5 s, a 100 kW single phase load is

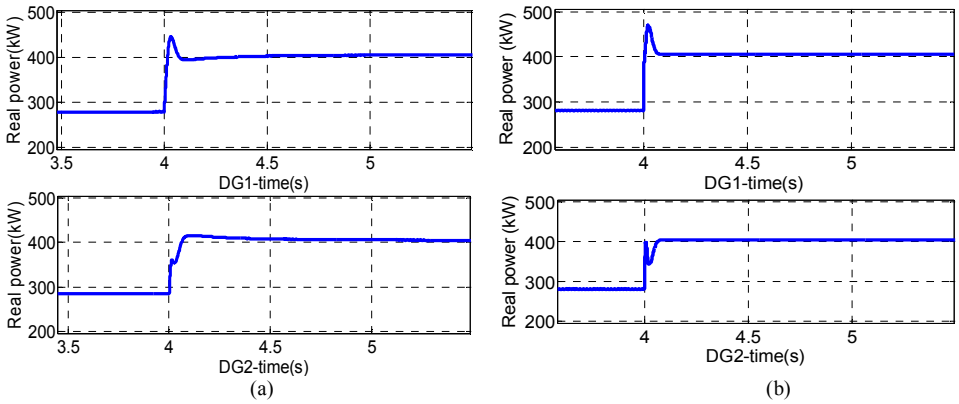

Figure 4-6. The real power waveforms of the MG with SG and VSC, (a) with cooperative droop and power loop, and (b) without the angle loop.

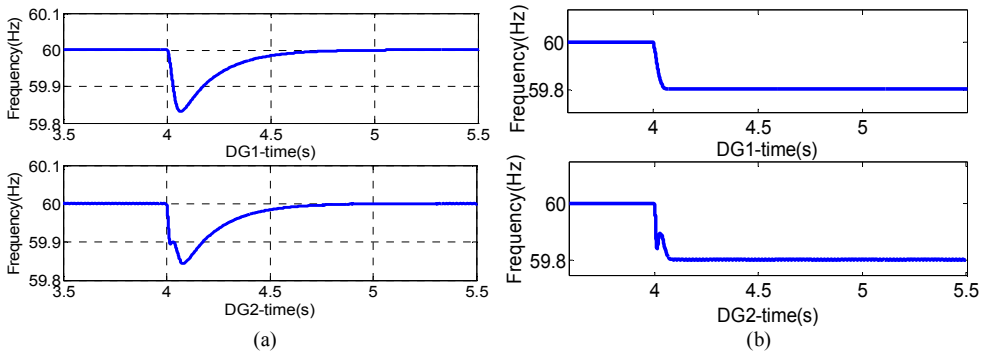

Figure 4-7.The frequency waveforms of the MG with SG and VSC, (a) with cooperative droop and power loop, and (b) without the angle loop ($K_d = 0$).

connected to the PCC. Figs. 4.6 and 4.7 exhibit the power and frequency waveforms before and after the load power variation for both cooperative droop control and frequency drooping methods. As it can be seen, power sharing error for both controllers before and subsequent to load power change is less than 0.5%. Nevertheless, in the system in which cooperative droop is employed, the rated frequency is recovered in less than 0.5 s whereas in the system with pure frequency drooping control, a permanent frequency offset equal to 0.2 Hz occurs. This is because when $K_d = 0$, system characteristics equation converges to (4.34), which yields a permanent frequency drop.

From the power quality perspective, it is important to have constant frequency operation because most of modern loads are sensitive to frequency deviations and it may adversely affect their operation. Whenever frequency droop in an MG is

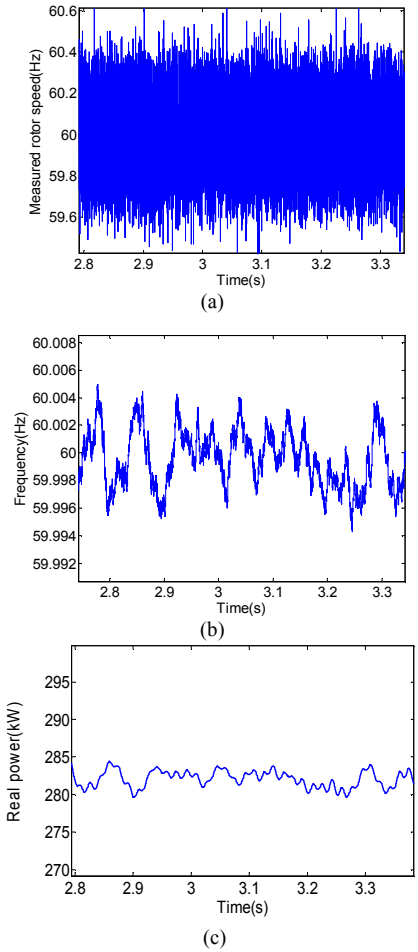

Figure 4-8. Effect of noise on the system performance, (a) measured rotor frequency, (b) actual rotor frequency, and (c) output power.

employed, proper operation of sensitive loads, when steady state frequency varies in a wide range, is a major concern. In this case, the system without the angle droop loop still presents satisfactory dynamic performance similar to the cooperative angle frequency controller which is due to existence of the extra power loop. Further, the maximum overshoot in the SG's real power is reduced from 475 kW to 445 kW with the hybrid droop control.

A1. Effect of Speed Sensor Noise on the Controller Performance

The controller performance with and without the presence of white noise in the SG's speed sensor are compared. Toward this, a white noise with average amplitude between 0.2-0.3 Hz is added to the measured speed as shown in Fig.

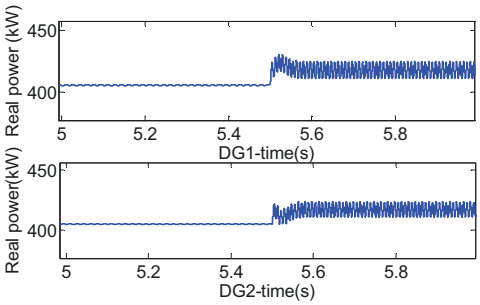

Figure 4-9. Effect of switching of a single phase load at PCC.

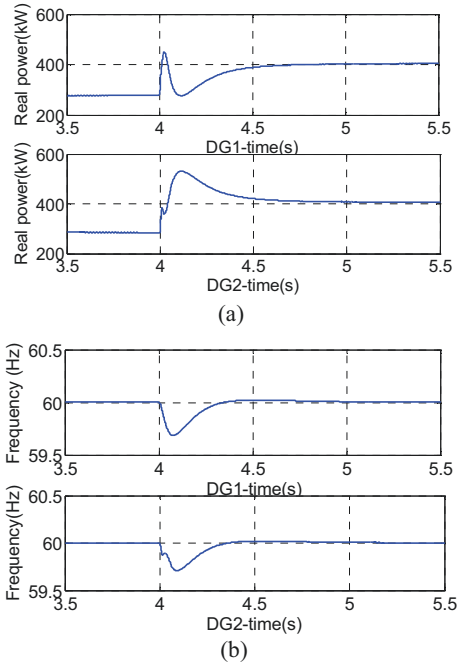

Figure 4-10. Effect of the SG's primary source with $\tau_p = 0.5$ (s) on system performance, (a) real power and (b) frequency.

4.8 (a). The actual rotor speed and output power waveforms are shown in Figs. 4.8 (b) and (c), respectively. It is obvious that noise does not have considerable effect on the output power and actual rotor speed as the rotor inertia filters-out high-frequency disturbances.

A2. Unbalanced system

In this scenario, it is supposed the system initially supplies the common 450 kW load and at *t*=5.5 s, a 25 kW single phase load is connected to phase b at PCC. The power waveforms after this event are given in Fig. 4.9. The single phase load

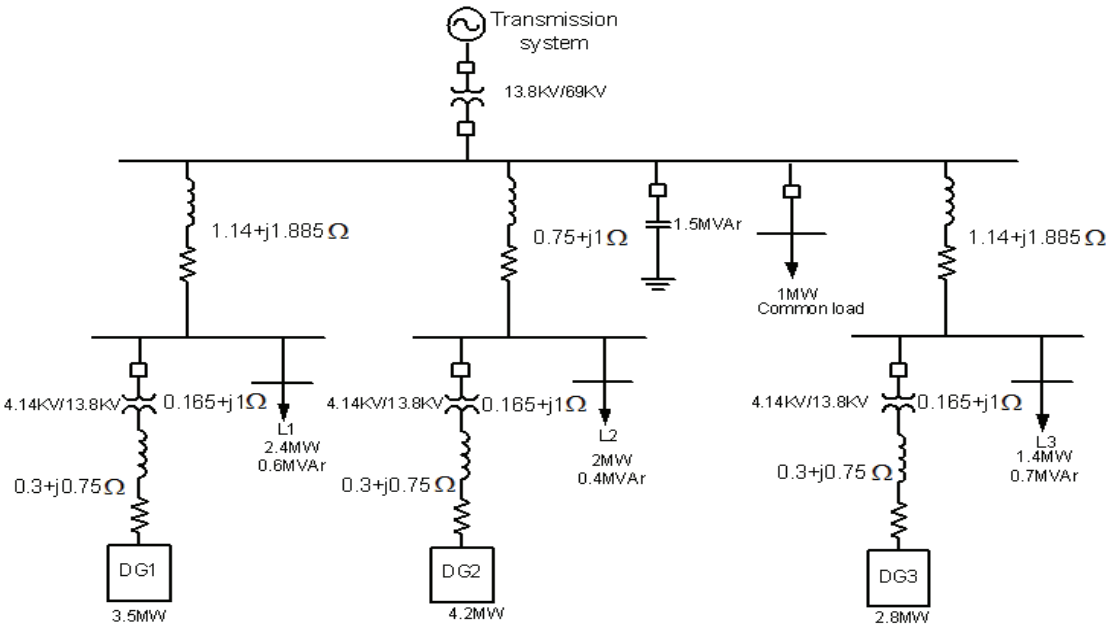

Figure 4-11. The Simulated system (case B).

causes power oscillations with amplitude of 7 kW with the average power equal to 416 kW. The real power is still shared equally between DG units. The ratio of negative and positive components of voltage is less than 2.6% which is within the acceptable typical unbalance limits. System stability is also preserved during unbalanced conditions. It should be noted that in this scenario, the positive sequence of the real and reactive powers are used for control purposes rather than the total real and reactive powers. It is emphasized that unbalanced condition is out of scope of this chapter. Although the controller presents satisfactory performance, to obtain better power sharing accuracy under unbalanced loading conditions, either virtual impedance shaping [105] or online set-point adjustment [106] can be applied.

A3. Effect of Dynamics of SG's Primary Source

In the previous studies, for the sake of simplicity, the dynamics of the primary source was ignored, i.e. $\tau_p = 0$. However, as shown in Fig. 4.4, in reality, an SG is driven by a primary mover with inherent dynamics. In this case, the dynamics of the primary source is taken into account, and it is supposed the SG is fed by a

Table 4-2 Parameters of the Three-DG MG (Case B)

Parameter	DG1	DG2	DG3
Line-line voltage (V)	4140	4140	4140
Maximum L-L VSC voltage (V)	4760	4760	4760
K_d	100	120	80
K_f	1e5	1e5	1e5
K_p	0.1	0.1	0.1
Voltage slope (n)	2.5e-4	2e-4	3e-4
ω_c	200	200	200

slow diesel engine with time constant (τ_p) equal to 0.5 s to study the effect of the primary source on power sharing and system dynamics. Other parameters are similar to those given in Table 4.1. The simulation results with consideration of primary mover dynamics before and after load power change are given in Fig. 4.10. It reveals that accurate power sharing with error less than 0.5% is achieved at nominal steady-state frequency operation. The frequency recovery time is about 1.0 s. It is also noticeable that the dynamic performance is degraded as compared to the case with $\tau_p = 0$. Furthermore, during the transient period, since VSC's source is considered as an ideal one without delay, the VSC mainly provides higher share of the MG power during transients causing more overshoot in its output power. In other words, the degraded dynamic performance is mainly caused by different time constants and dynamic behaviors of primary sources of VSC and SG. In general, the higher the time constant of the SG primary source, the worse dynamic performance and more interaction between units is yielded.

4.4.2 MG with Three DG Units and Supplementary Control (System B)

B1. Case 1: Disconnection of DG2

The model shown in Fig. 4.11 is simulated to evaluate the performance of the control system with nonlinear cooperative droop control. The controller parameters are given in Table 4.2. It is supposed that the MG initially works in islanding mode, and then it is reconnected to the grid. The sequence of events is

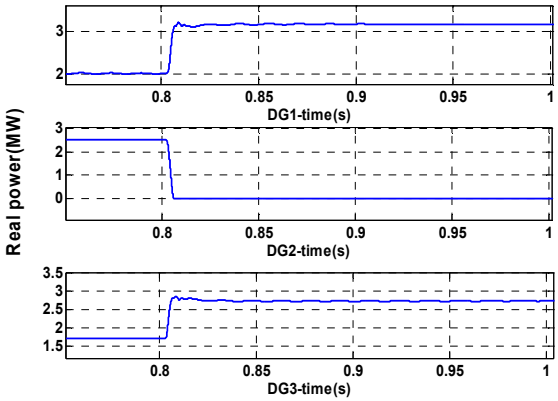

Figure 4-12. Power waveforms of case *B1*.

as follows: at t=0.8 s, DG2 is disconnected and DG1 and DG3 supply the total MG load demand. At t=1.5 s, DG1 is again connected to the MG. At t=2.5 s, the static switch is closed and the grid is restored. At t=3 s, again an islanding event occurs. All these scenarios are considered as large-signal disturbances, where DGs output powers, frequencies and load angles rapidly change in a wide range. It is assumed that the MG initially works in islanding mode and all the DGs and loads are connected. At t=0.8 s, DG2 is disconnected from the MG and DG1 and DG3 supply the local load of DG2. The power waveforms with the supplementary control are shown in Fig. 4.12. Before DG2 disconnection, the generated power of DG1, DG2 and DG3 are 2.06, 2.43 and 1.645 MW, respectively, which are very close to their desirable ratios (4:5:6) and the maximum error in power sharing is less than 1.5%. It should be noted the main assumption here is that DG units have enough power capacity to supply the total MG load demand. As it can be seen from Fig. 4.12, after DG2 disconnection, the output powers of DG1 and DG3 still remain within their power capacities. If this is not the case and DG units cannot provide the load power demand, a load shedding strategy, as presented in [36], should be applied to shed non-critical loads. However, this chapter deals with stability issues of MG under generation-load matching conditions, which is a necessary but not sufficient condition for the overall MG stability. After the DG disconnection, the system with the supplementary control exhibits fully damped behavior without any overshoot.

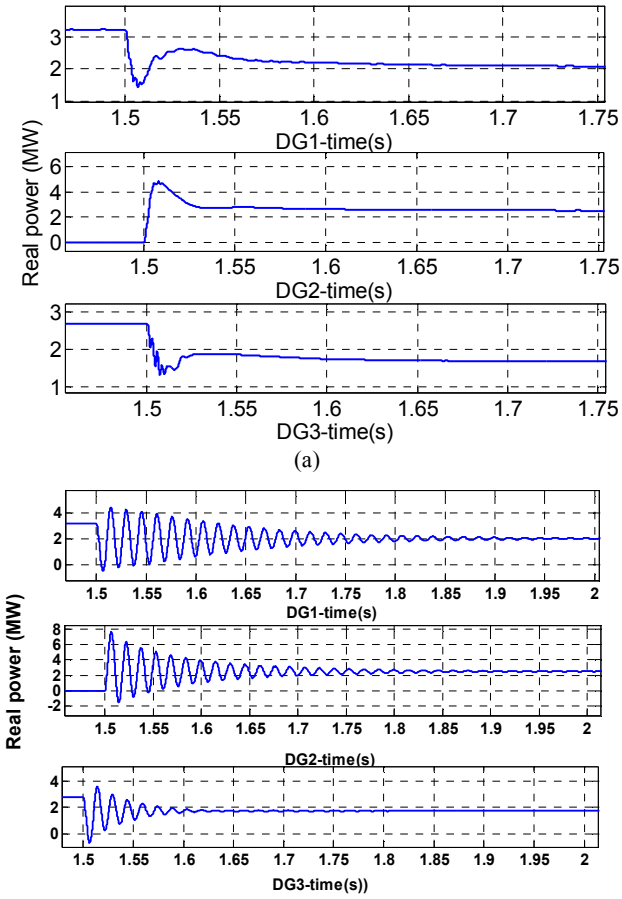

Figure 4-13. Power waveforms of case B2, (a) with, and (b) without the supplementary controller.

B2. Case2: Reconnection of DG2 with Out-of-Phase Reclosing

In this section, the transient behavior of the MG after reconnection of DG1 is investigated. Again, this scenario is considered as a large-signal disturbance because DG2, which forms 40% of the total MG power capacity, is reconnected without any synchronization process. Note that any considerable difference between voltage angle of DG2 and the MG at the point of connection is considered as a large disturbance and results in severe transients. The power waveforms with and without the supplementary nonlinear controller are shown in Fig. 4.13. The effectiveness of the nonlinear controller in this case is obviously pronounced and the system with the supplementary nonlinear controller offers much better transient performance as compared to the linear system. Actually, the

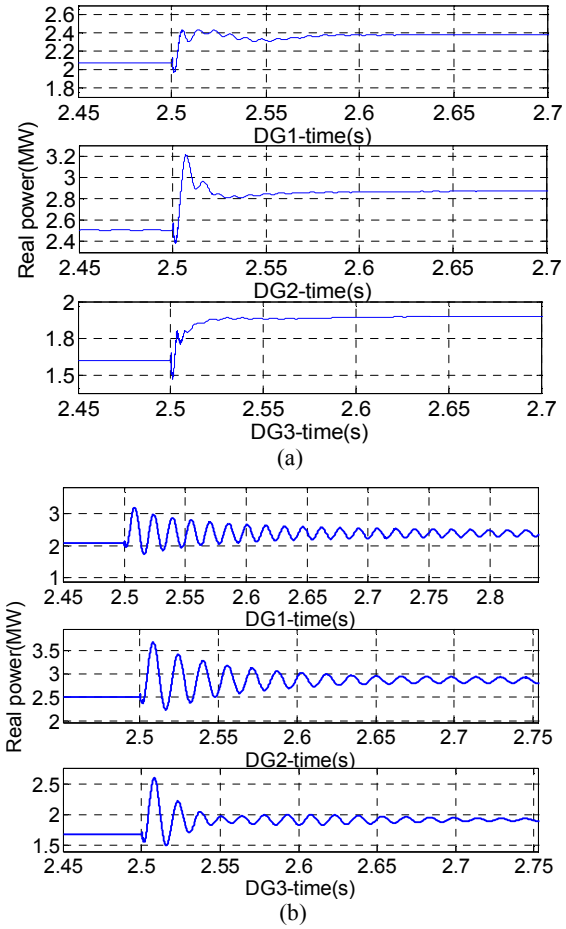

Figure 4-14. Power waveforms of case B3, (a) with, and (b) without the supplementary controller.

nonlinear controller adjusts VSC voltage such that it damps angle, frequency and power fluctuations.

B3. Case3: Grid Restoration with Out-of-Phase Reclosing

In the grid connected mode, DG units are required to inject their preset real powers and there is no need for sharing power. Thus, the output powers of DG units are abruptly changed subsequent to connection to the grid to their reference values. During grid connection, DG1, DG2 and DG3 generate 2.38 MW, 2.86 MW and 1.9 MW, respectively. In this scenario, the static switch at the PCC is suddenly closed and the utility grid is restored. The power waveforms are illustrated in Fig. 4.14. Note that no synchronization process is applied and

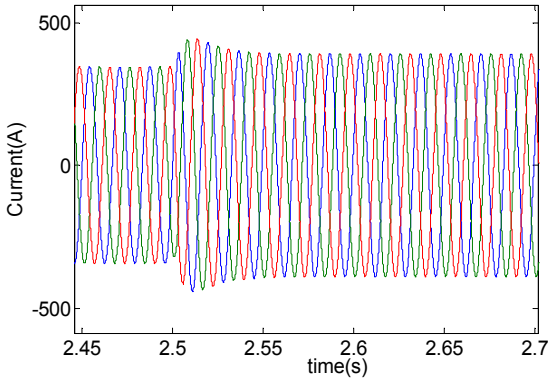

Figure 4-15. Current waveforms of DG3 during grid connection using supplementary nonlinear controller.

connection is abrupt without any information from the grid voltage. In fact, to connect the MG to the main grid seamlessly, the angle and voltage mismatch between two sides of the static switch should be near to zero. Any considerable error between phase, frequency and amplitude of the MG and the utility grid voltages at PCC may cause severe oscillations, high currents and even instability. High current may flow to the circuit subsequent to grid connection. This scenario is similar to the out-of-phase reclosing event that might take place when a DG unit (or a micro-grid) is not disconnected upon a temporary fault in a feeder equipped with an auto-recloser. Nevertheless, by proper adjustment of voltages of the DG units during grid connection using the supplementary controller, power, frequency, angle and current are kept within acceptable limits. Fig. 4.15 shows the current waveforms of DG3 during grid connection, which clearly confirms that no considerable current overshoot occurred; only for one cycle some minor overshoot in the phase current is observed. On the contrary, any instability in the load angle and frequency may result in high current flowing to the circuit.

In fact, the duty of the nonlinear controller is to adjust the voltage amplitude such that the load angle and frequency stability is preserved, which automatically results in smooth current waveforms during grid connection. In other words, the "plug-and-play" concept is achieved via the proposed nonlinear cooperative control. Otherwise, grid connection without verifying the synchronization process and without using the nonlinear controller may cause severe overshoot in power

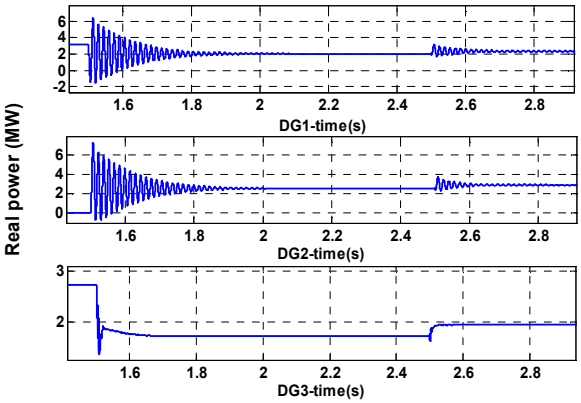

Figure 4-16. Power waveforms of case B4. DG1 and DG2 without nonlinear controller and DG3 with the supplementary nonlinear controller.

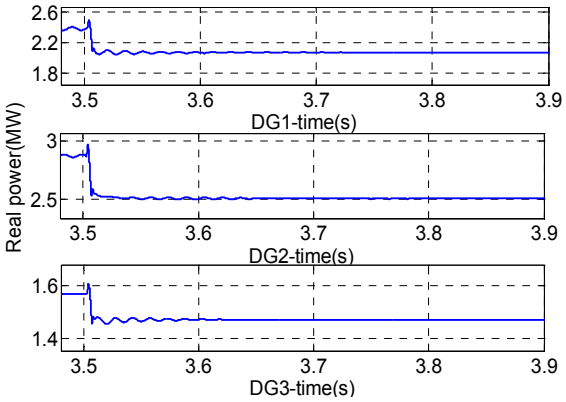

Figure 4-17. Power waveforms subsequent to islanding.

and current. The same problem also exists in Case2, where voltage angle and amplitude mismatch between DG2 and the MG at the point of their connection generates severe transients. Similar to case 2, nonlinear-controlled DGs have smooth and well damped performance during grid connection while the linear controller-based MG exhibits poor transient behavior. Again, in this case, the nonlinear controller adjusts the DG voltage reference such that angle, frequency and power fluctuations are minimized. It should be noted that frequency and angle oscillations depend on damping and synchronizing powers, respectively. According to (4.6) and (4.7), the damping and synchronizing powers are proportional to K_f and K_d, respectively. By increasing these constants, more damped power and frequency with faster convergence can be obtained at the cost of poor static performance and power sharing. However, the nonlinear

supplementary controller provides the necessary damping under wide range of operating conditions and droop parameters without loss of stability. The synchronization and out-of-phase reclosing problems are typical issues that can exist in MGs and they demand a nonlinear controller because any large difference in angle and frequency between two sides of switch at the moment of connection is a large-signal disturbance and leads to severe transients.

B4. Case4: DG2 Reconnection and Grid Restoration- DG1 and DG2 Without andDG3 with Nonlinear Controller

In this section, the ability of the nonlinear controller to overcome interactions between DG units is investigated. Toward this, a scenario is taken into account in which DG 1 and DG2 use the linear angle-frequency droop whereas DG3 uses the nonlinear supplementary controller. Similar to case 2 and 3, at t=1.5 s DG2 is connected to the MG and at t=2.5 s, the static switch is closed. It is evident from Fig. 4.16 that at the moment of reconnection of DG2, its output power starts to oscillate and due to its interaction with DG1, the output power of DG1 also fluctuates. That is to say that instability and oscillations propagate within the MG. On the contrary, DG3 has smooth operation in both scenarios. This case shows the ability of the nonlinear supplementary control to mitigate instabilities due to interaction between DG units which is one of its remarkable features.

B5. Case5: Islanding

Another scenario that frequently occurs in an MG system is transition from grid connection to islanding mode. When a fault occurs in the grid, it is necessary to disconnect the MG from the main grid. The proposed angle-frequency droop control has the ability to work in both modes without change in the controller structure. Consequently, the problems due to islanding detection are inherently eliminated. The power sharing is automatically achieved by drooping constants of K_f and K_d, whereas these constants are employed as damper and synchronizer during the grid connection. The power waveforms of DG units subsequent to islanding are presented in Fig. 4.17. In this case, the transition to islanding is

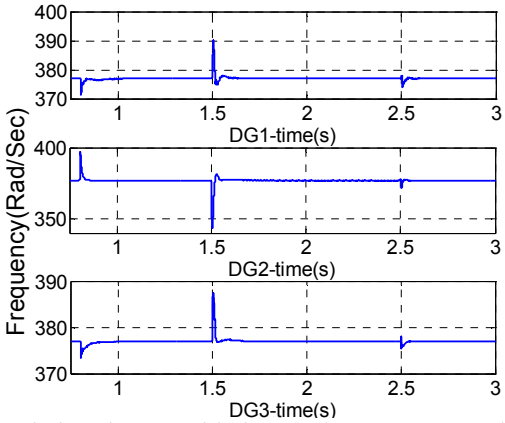

Figure 4-18. Frequency variations in MG with the supplementary control.

seamless with minimum fluctuation, which proves the effectiveness of the combined droop controller. Frequency waveforms of different DG units between t=0.75 s and 3.0 s in the system with the nonlinear controller are shown in Fig. 4.18, which shows fixed nominal-frequency steady-state operation of the MG in both modes, which is one of the main benefits of the proposed hybrid controller.

Chapter 5 Enhanced Micro-Grid Stability Using Nonlinear Micro-Grid Stabilizer[4]

It was discussed in the previous chapter the linear controllers fall short to guarantee stability of the system in all operating points and especially when the operating moves rapidly in a wide range. Required features such plug-and-play and also PLL-less grid synchronization capability make large-signal stability of the system a mandatory requirement in smart grids. This chapter aims at developing a supplementary nonlinear to enhance the DG stability during severe disturbances and guarantee large signal stability of the MG while the main motivation is the highly-nonlinear behaviour of power sharing dynamics in a typical MG system with a different approach of chapter 4. The adaptive back-stepping (AB) method is employed to design the nonlinear controller which is one of the most rigorous nonlinear control design tools [82-86].

5.1 Inverter Model

Fig. 5.1 depicts the basic concept of the converter control topology. The basic idea is to mimic back-EMF generation principle and rotor dynamic of a synchronous generator, including its rotor momentum of inertia (J) and friction (m). The utilization of emulated rotor dynamics improves the converter dynamics and it yields a control structure that is more suitable for the MG operation [29], [18]. In this VSC model, the virtual rotor plays this role of controlling the frequency dynamics, which is not accessible in the conventional current/voltage control topology of VSC. The virtual friction (m) is responsible to damp VSC frequency oscillations in grid-connected mode. However, it is proposed in this chapter to use it as a droop control for power sharing in islanded mode.

The voltage generation principle is like back-EMF generation in a typical SG, given by: [50]

$$\tilde{e} = \psi_f \omega_v \sin\tilde{\theta} \tag{5.1}$$

where $\tilde{e}$ stands for a balanced three-phase voltage. This equation emulates

[4] The chapter is published in *IEEE Transactions on Smart Grid [107].*

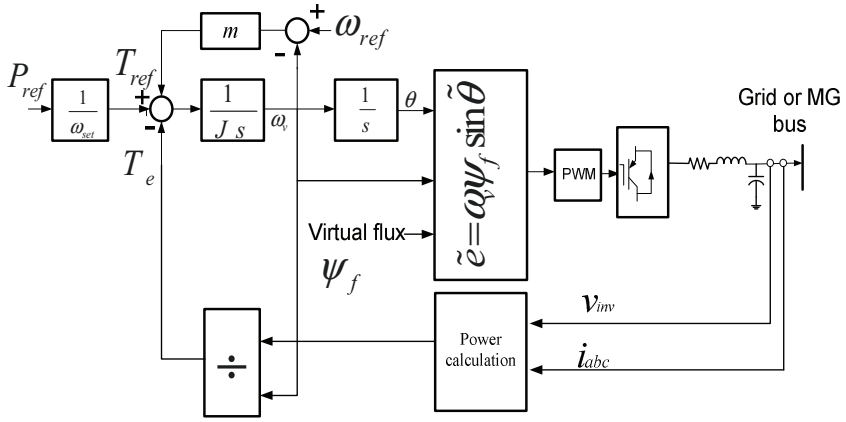

Figure 5-1. The synchronverter model.

rotational back-EMF generation in an SG.

The frequency dynamic of the VSC is given by:

$$J\frac{d\omega_v}{dt} = T_{ref} - T_e - m(\omega_v - \omega_{ref}) \tag{5.2}$$

which is directly obtained from Fig. 5.1. Similar to every multi-phase electrical system, output power is calculated by inner product of three-phase voltages and currents:

$$P_e = \langle \tilde{i}, \tilde{e} \rangle = \omega_v \psi_f \langle \tilde{i}, \sin\tilde{\theta} \rangle \tag{5.3}$$

where

$$\tilde{i} = \left\langle i\cos\varphi, i\cos(\varphi - \frac{2\pi}{3}), i\cos(\varphi + \frac{2\pi}{3}) \right\rangle. \tag{5.4}$$

Thus, (5.3) is simplified to

$$P_e = \frac{3}{2}\omega_v \psi_f i\cos(\theta - \varphi) = \frac{3}{2}\omega_v \psi_f i\cos\delta \tag{5.5}$$

where

$$\alpha = \theta - \varphi = \int (\omega_v - \omega_i)dt. \tag{5.6}$$

The virtual electrical torque is given by:

$$T_e = \frac{P_e}{\omega_v} = \frac{3}{2}\psi_f i\cos\alpha. \tag{5.7}$$

It is worth noticing that unlike electrical machines, there is no real electrical torque and it is just defined for the sake of the control design of a VSC-based DG

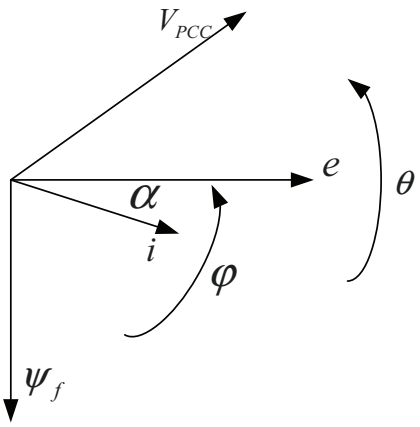

Figure 5-2. Phasor diagram of the system.

unit.

Similarly, the reactive power equation is obtained as:

$$Q_e = \frac{3}{2}\omega_v \psi_f i \sin(\alpha). \tag{5.8}$$

Fig. 5.2 exhibits the phasor diagram of a VSC connected to the grid. One of the most attractive features of this VSC topology is the existence of friction coefficient of (m), which acts like a damper in grid connected mode and is used as a frequency-power droop control for power sharing among DG units in islanding. In other words, the term $m(\omega_{ref} - \omega)$ provides a power sharing tool for DG units. Moreover, the values of m and J can be selected arbitrarily as a function of design requirements and they can have values which are not feasible in a real SG.

The torque-frequency droop function to realize the real power sharing in islanding mode is given by:

$$\omega_v - \omega_{ref} = \frac{1}{m}(T_{ref} - T_e) \tag{5.9}$$

which can be rewritten in the form of

$$\omega_v - \omega^* = -\frac{1}{m}T_e \tag{5.10}$$

$$\omega^* = \omega_{ref} + \frac{1}{m}T_{ref} \tag{5.11}$$

The value of static droop gain (m) is calculated as a function of the DG maximum

torque ($T_{e\_\max}$):

$$m = \frac{T_{e\_\max}}{\omega^* - \omega_{ref}} \tag{5.12}$$

Accordingly, the virtual rotor momentum of inertia is obtained by:

$$J = m\tau_f \tag{5.13}$$

where τ_f is the time constant of power-frequency droop loop determined by designer according to acceptable frequency dynamics.

Two different topologies for virtual rotor flux control are proposed as shown in Fig. 5.3, namely they are Model 1, which adopts a low-pass filter to generate the virtual rotor flux; and Model 2, which adopts a pure integrator. In the first topology, the reference voltage is again generated by a voltage droop function. Processed by the low-pass filter emulating rotor flux decay dynamic of an SG, the rotor flux is obtained. In the latter, the voltage command, which is generated by a reactive power-voltage droop, is compared to the actual voltage and the error is fed into the integrator resulting in the reference rotor flux. It is noticeable that in Model 2, the low-pass filter behaves like the flux decay equation [108] of a real SG, so in Model 2 the VSC acts just the same as an SG. This helps embedding numerous DG units in a large power system where VSCs and the conventional power plants are seen the same by the power system. The flux decay equation of synchronous generators is due to the fact that applied DC voltage to the rotor excitation appears with a delay in the stator side as a result of rotor winding inductance. In this case, the controller transfer-function (G_{flux}) is as follow:

$$G_{flux}(s) = \frac{k_a}{\tau_a s + 1} \tag{5.14}$$

where τ_a is the flux loop time constant. By tuning τ_a appropriate voltage transient response can be fulfilled. The voltage droop function is as follow:

$$E = E^* - nQ_e \tag{5.15}$$

where E^* is the no load voltage and Q_e is DG reactive power. This droop control is used in both modes of operation to share reactive power among DG units. In

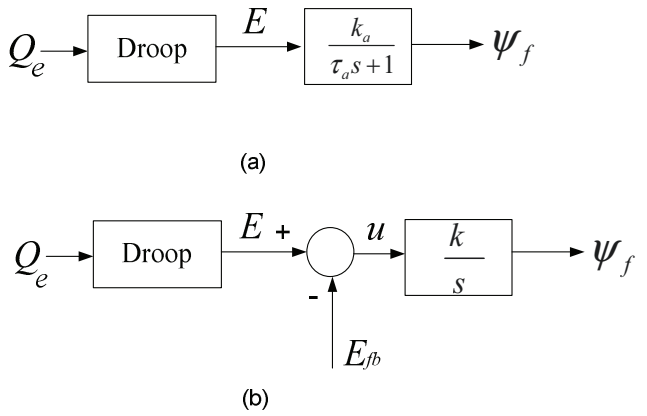

Figure 5-3. Flux control loops: (a) Model 1 with low-pass filter and (b) Model 2 with integrator.

fact, in ideal case, total reactive power demand is distributed according to static droops constants (n). It should be noted that the in grid connected mode, the droop control cannot regulate the injected reactive power to the grid and it is just a tool to share the reactive power demand proportional to reactive power capacity of various DG units. That is to say that DG buses are *P-V* buses instead of *P-Q* buses. To manage the generated reactive powers of DG units in grid connected mode an additional reactive power control loop is required. However, this reactive control loop cannot be applied in islanding mode and causes instability [29]; consequently subsequent to islanding detection the reactive power control loop must be removed.

5.2 Proposed Control Topologies and Design Process

To overcome the aforesaid problems, a novel control topology suitable for nonlinear control design is presented in this chapter.

5.2.1 Controller Topology

Fig. 5.4 shows the proposed control topologies. The controller uses power angle, frequency and power as control variables instead of conventional current and voltage control loops. As it is seen, the controller has three control loops, namely angle loop, frequency loop and torque loop which is afterward called microgrid stabilizer. There are two possibilities to realize the nonlinear controller

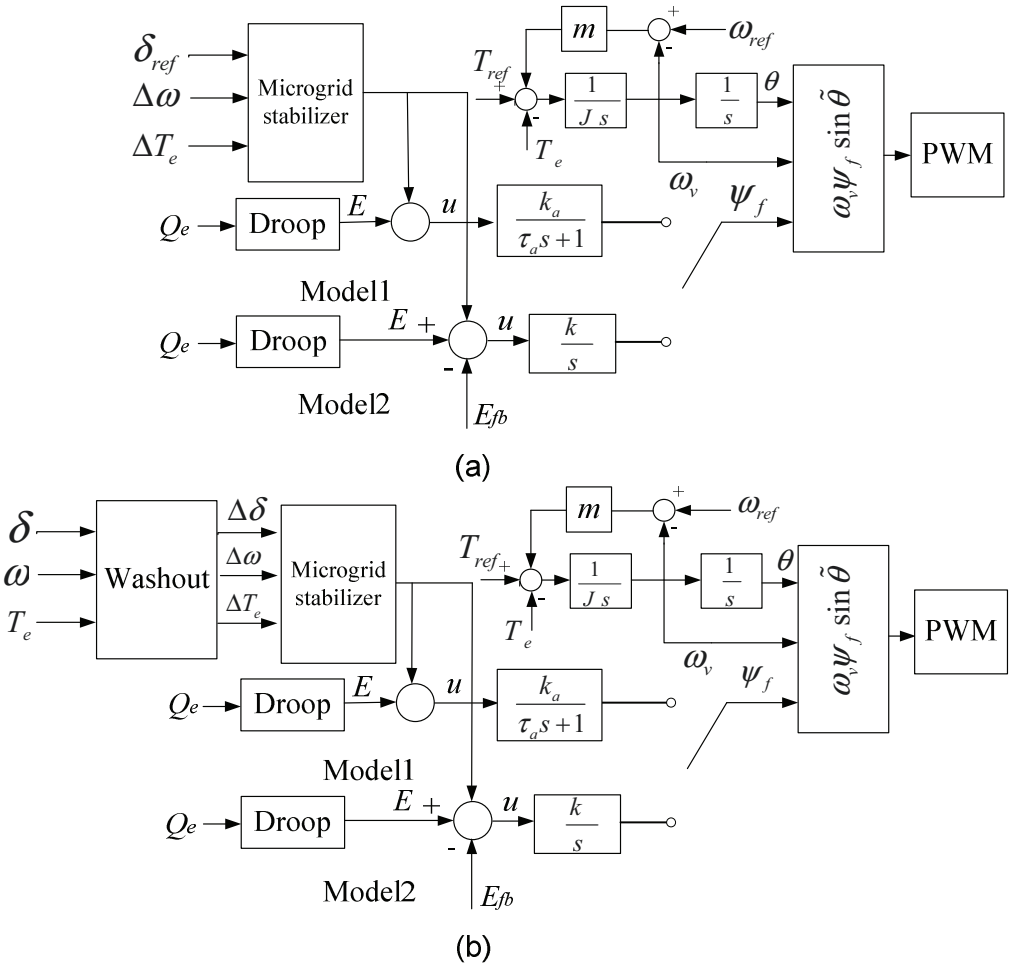

Figure 5-4. Controller topology.

shown Figs. 5.4 (a) and (b), respectively. The first is a power angle tracker in which the controller aims at tracking the desirable power angle (δ_{ref}) by proper frequency and power setting whereas the latter just tries to damp angle oscillations while there is no defined angle reference. In fact in Fig. 5.4 (b) the perturbations of signals are obtained by a washout filter without knowledge of their set values. The angle controller generates the reference frequency deviation ($\Delta\omega_{ref}$) and the frequency loop is responsible to determine the required torque (ΔT_{e-ref}) as a function of angle error and frequency error. The nonlinear microgrid stabilizer which can be considered as torque controller attempts to set torque error

equal to zero using a supplementary voltage control. Simply speaking, in contrast to the conventional current-voltage control, the power is directly controlled by varying power angle and voltage amplitude. That is to say that amplitude of current can be controlled by adjusting power angle (δ) and frequency (ω_v) via a direct power control strategy.

The proposed control method for the MG converter offers many advantages over the conventional VSC control applied in the DG control. First, the controller is universal and flexible for all operational modes as there is no need for reconfiguration of the controller. This means there is no need for changing the control strategy after islanding; therefore stability issues associated with islanding detection delays are inherently mitigated. It can also realize a seamless transition to islanding mode with the assisted nonlinear controller.

Moreover, the frequency droop loop provides a tool for power sharing among DG units in a microgrid. Another interesting feature of this controller is reactive power control in grid connected mode via setting the angle reference. As mentioned earlier, the controller is in angle-frequency domain and the nonlinear controller sets the power angle equal to its reference by adjusting output voltage. Thus, the desirable power factor of VSC in grid-connected mode is achieved by proper selection of reference power angle (α). Furthermore, the controller only depends on local information. The smooth stable performance of the MG during severe transitions like islanding, grid restoration and sudden load power variations is fulfilled by the proposed nonlinear MG stabilizer. The overall control system is synthesized in the large-signal sense.

5.2.2 State Space Model

In this section the VSC presented in section 5.1 is considered. Under some standard assumptions, the proposed VSC can be described by a classical model. To design a nonlinear control, first of all the state space model of the system must be obtained. Every state space model is written in the form:

$$\dot{X} = AX + BU \tag{5.16}$$

where X is the vector of state space variables and U is the vector of control

inputs. In the proposed VSC control structure, power angle δ, frequency (ω_v) and virtual torque (T_e) are state space variables.

To obtain the power angle (α) dynamics, it is assumed that voltage angle dynamics is much faster than the current angle dynamics. This means that the rate of change of δ is proportional voltage frequency deviation from its rated value. The frequency dynamics is governed by frequency droop and virtual rotor loops shown in Fig. 5.4 Accordingly, the angle and frequency dynamics are written in the form:

$$\Delta\dot{\alpha} = \Delta\omega \tag{5.17}$$

$$\Delta\dot{\omega} = -\frac{m}{J}\Delta\omega + \frac{1}{J}(-T_e + T_{ref}) \tag{5.18}$$

where $\Delta\omega$ and $\Delta\alpha$ represent the variation of frequency and angle from their equilibrium points. The torque dynamic equation is calculated from (5.7):

$$\dot{T}_e = \frac{3}{2}\dot{\psi}_f i\cos\alpha + \frac{3}{2}\psi_f \dot{i}\cos\alpha - \frac{3}{2}\psi_f i\Delta\omega\sin\alpha \tag{5.19}$$

The derivative of flux is determined by the voltage loop dynamic depicted in Fig. 5.3. As explained in section 5.1, two different schemes for voltage loop are available. The general model of these two controllers can be written in the form of:

$$G_c(s) = \frac{k_a}{\tau_a s + c} \tag{5.20}$$

where $c = 1$ for Model 1 with low-pass filter controller and $c = 0$ for Model 2 with integrator controller. From (5.20) one has:

$$\dot{\psi}_f = \frac{k_a}{\tau_a}u - \frac{c}{\tau_a}\psi_f \tag{5.21}$$

By Replacing (5.21) in (5.19), (5.22) is followed:

$$\dot{T}_e = \frac{3}{2}[\frac{k_a}{\tau_a}u - \frac{c}{\tau_a}\psi_f]i\cos\alpha + \frac{3}{2}\psi_f \dot{i}\cos\alpha - \frac{3}{2}\psi_f i\Delta\omega\sin\alpha \tag{5.22}$$

Considering (5.7), (5.22) is simplified to:

$$\dot{T}_e = \frac{3}{2}\frac{k_a}{\tau_a}u\cos\alpha - \frac{c}{\tau_a}T_e + \frac{3}{2}\psi_f \dot{i}\cos\alpha - \frac{3}{2}\psi_f i\Delta\omega\sin\alpha \tag{5.23}$$

Since (5.17) and (5.18) are in perturbed form, we need to rewrite (5.22) in the

perturbed form using similar approach given in [86],[108] as follow:

$$\Delta\dot{T}_e = \frac{3}{2}\frac{k_a}{\tau_a}u\cos\Delta\alpha - \frac{c}{\tau_a}\Delta T_e + \frac{3}{2}\psi_f \dot{i}\cos\Delta\alpha - \frac{3}{2}\psi_f i\Delta\omega\sin\Delta\alpha \tag{5.24}$$

Finally, the VSC model is compensated into perturbed form of:

$$\dot{x}_1 = x_2 \tag{5.25}$$

$$\dot{x}_2 = a_2 x_2 + a_3 x_3 \tag{5.26}$$

$$\dot{x}_3 = u_f - \frac{c}{\tau_a}x_3 + \frac{3}{2}\{\psi_f \dot{i}\cos x_1 - \psi_f i x_2 \sin x_1\} + \gamma \tag{5.27}$$

where $a_2 = -m/J, a_3 = -1/J$ and $u_f = 3k_a/2\tau_a\, u\cos x_1$, and $[x_1, x_2, x_3] = [\Delta\alpha, \Delta\omega, \Delta T_e]$.

The term "γ" is added to (5.27) as a lump-sum of system uncertainties and includes local converter and converter-MG interaction uncertainties. The origins of these uncertainties can be disturbances, system parameters changes and inaccurate measurement. All these uncertainties are accumulated in one term [85]. The uncertain term "γ" is estimated through adaptive disturbance estimation technique. The application of this adaptive term makes system more robust against measurement and modeling errors, and system disturbances.

5.2.3 Design Process

In this section, based on adaptive back-stepping method, the design procedure for system (5.25)-(5.27) is followed. The design aims at minimizing the error between the desired reference signal x_{iref} and its actual value x_i, so that state variables steer their desired values. The error of reference signal x_{iref} and its actual value x_i is defined as:

$$e_i = x_i - x_{iref}. \tag{5.28}$$

The procedure has three steps:

Step1: to stabilize power angle (α), the following Lyapunov function error is selected as an index of angle:

$$V_1 = 1/2\, e_1^2. \tag{5.29}$$

The derivative of (5.29) along its trajectory is

$$\dot{V}_1 = e_1\dot{e}_1 \tag{5.30}$$

If we make $\dot{V}_1$ negative definite, the system (5.25) becomes asymptotically stable. Now choose

$$x_{2ref} = -k_1 e_1 \quad k_1 > 0 \tag{5.31}$$

then

$$\dot{V}_1 = -k_1 e_1^2 + e_1 e_2. \tag{5.32}$$

As it is seen from (5.32), there is no guarantee that $\dot{V}_1 < 0$. In the next steps x_{3ref} and u are selected such that this condition is established [85].

Step2: Design x_{3ref} according to Lyapunov function

$$V_2 = \tfrac{1}{2} e_1^2 + \tfrac{1}{2} e_2^2. \tag{5.33}$$

The derivative of V_2 along its trajectory is:

$$\dot{V}_2 = \dot{V}_1 + e_2\dot{e}_2 \tag{5.34}$$

where $\dot{e}_2 = \dot{x}_2 - \dot{x}_{2ref}$. Using equations (5.26) and (5.31), it follows that:

$$\dot{e}_2 = [1 - k_1(a_2 + k_1)]e_1 + (a_2 + k_1)e_2 + a_3 e_3 + a_3 x_{3ref} \tag{5.35}$$

Thus $\dot{V}_2$ is simplified to:

$$\begin{aligned}\dot{V}_2 = {} & -k_1 e_1^2 + [a_3 x_{3ref} - (k_1^2 + k_1 a_2 - 1)e_1 + (a_2 + k_1)e_2]e_2 \\ & + a_3 e_2 e_3\end{aligned} \tag{5.36}$$

If

$$x_{3ref} = b_1 e_1 + b_2 e_2 \tag{5.37}$$

where

$$b_1 = -\frac{(1 - k_1(a_2 + k_1))}{a_3} \tag{5.38}$$

$$b_2 = -\frac{(k_1 + k_2 + a_2)}{a_3} \tag{5.39}$$

then, $\dot{V}_2$ is obtained as

$$\dot{V}_2 = -k_1 e_1^2 - k_2 e_2^2 + a_3 e_2 e_3 \tag{5.40}$$

From (5.40), it is concluded that system (5.25)-(5.27) still is not fully stabilized and hence we need to choose u_f in the next step to make $\dot{V}_2$ negative definite.

Step3: similar to the previous steps, here the Lyapunov function is defined as:

$$V_3 = 1/2\, e_1^2 + 1/2\, e_2^2 + 1/2\, e_3^2 + 1/2\, \rho(\gamma - \hat{\gamma})^2 \tag{5.41}$$

where $\hat{\gamma}$ is estimated uncertainty function (γ), and ρ is the adaptation law gain. Since V_3 involves V_2 and V_1, its stabilization automatically guarantees stability of the first and second loops. Now, consider the dynamics of $e_3 = x_{3ref} - x_3$ which is given by (5.27) and (5.37):

$$\begin{aligned} \dot{e}_3 &= \dot{x}_3 - \dot{x}_{3ref} \\ &= u_f - \frac{c}{\tau_a} x_3 + \frac{3}{2}\{\psi_f \dot{i} \cos x_1 - \psi_f i x_2 \sin x_1\} + \gamma - \dot{x}_{3ref} \end{aligned} \tag{5.42}$$

$\dot{x}_{3ref}$ is calculated by (5.26), (5.27), (5.31), and (5.37)

$$\dot{x}_{3ref} = b_1 \dot{e}_1 + b_2 \dot{e}_2 \tag{5.43}$$

where

$$\begin{aligned} \dot{e}_2 &= \dot{x}_2 - \dot{x}_{2ref} = a_2 x_2 + a_3 x_3 + k_1 \dot{e}_1 \\ &= a_2 x_2 + a_3 x_3 + k_1 x_2 \end{aligned} \tag{5.44}$$

Finally, $\dot{x}_{3ref}$ becomes:

$$\dot{x}_{3ref} = A e_1 + B e_2 + a_3 b_2 e_3 \tag{5.45}$$

$$A = (b_1 b_2 a_3) - k_1 (b_1 + k_1 b_2 + a_2 b_2) \tag{5.46}$$

$$B = (b_1 + a_3 b_2^2 + a_2 b_2 + k_1 b_2) \tag{5.47}$$

Thus, $\dot{V}_3$ is given by:

$$\begin{aligned} \dot{V}_3 = & -k_1 e_1^2 - k_2 e_2^2 + \\ & [u_f + \frac{3}{2}\psi_f \dot{i} \cos x_1 \\ & - (\frac{c}{\tau_a} b_1 + A - \frac{3}{2} k_1 \psi_f i \sin x_1) e_1 \\ & - (-a_3 + B + \frac{c}{\tau_a} b_2 + \frac{3}{2}\psi_f i \sin x_1) e_2 \\ & - (\frac{c}{\tau_a} + a_3 b_2) e_3 + \gamma] e_3 \\ & - (\gamma - \hat{\gamma}) \rho \dot{\hat{\gamma}}. \end{aligned} \tag{5.48}$$

If the adaptation law is chosen as:

$$\dot{\hat{\gamma}} = \frac{1}{\rho} e_3 \tag{5.49}$$

then

$$\begin{aligned} \dot{V}_3 = & -k_1 e_1^2 - k_2 e_2^2 + \\ & [u_f + \frac{3}{2}\psi_f \dot{i} \cos x_1 \\ & -(\frac{c}{\tau_a} b_1 + A - \frac{3}{2} k_1 \psi_f i \sin x_1) e_1 \\ & -(-a_3 + B + \frac{c}{\tau_a} b_2 + \frac{3}{2}\psi_f i \sin x_1) e_2 \\ & -(\frac{c}{\tau_a} + a_3 b_2) e_3 + \hat{\gamma}] e_3 \end{aligned} \tag{5.50}$$

Consequently, if the control input is selected equal to

$$\begin{aligned} u_f = & -\frac{3}{2}\psi_f \dot{i} \cos x_1 \\ & + (\frac{c}{\tau_a} b_1 + A - \frac{3}{2} k_1 \psi_f i \sin x_1) e_1 \\ & + (-a_3 + B + \frac{c}{\tau_a} b_2 + \frac{3}{2}\psi_f i \sin x_1) e_2 \\ & + (\frac{c}{\tau_a} + a_3 b_2 - k_3) e_3 - \hat{\gamma} \qquad\qquad k_3 > 0 \end{aligned} \tag{5.51}$$

then by replacing (5.51) in (5.50), the derivation of the Lyapunov equation V_3 is expressed as:

$$\dot{V}_3 = -k_1 e_1^2 - k_2 e_2^2 - k_3 e_3^2 \tag{5.52}$$

Thus, the global stability of converter model (5.25)-(5.27) is confirmed. If equation (5.51) is satisfied, the state space model of (5.25)-(5.27) becomes asymptotically globally stable or equivalently large-signal stable. In other words, it guarantees the stability of power angle, frequency and power at the whole loading trajectory of MG generators.

The control parameters are the set $[k_1, k_2, k_3, \rho]$. The system performance is highly related to these coefficients and the designer has high degree of freedom to find the best combination of these system constants to realize the optimum tradeoff among system performance objectives.

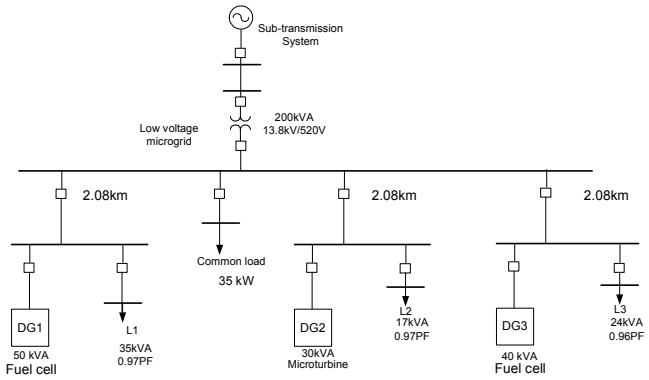

Figure 5-5.The simulated system.

5.3 Results and Evaluations

Several simulations are carried out in MATLAB/SIMULINK environment to study the effectiveness of the proposed control topology. The scenarios include DG startup and grid synchronization, transition to islanding mode and grid reconnection. Without loss of generality, DG units are considered as dispatchable one [24] with enough power and inertia-less dc-link [16]. The simulated system is depicted in Fig. 5.5 has three DG units connected in parallel to the main grid through connecting cables and static switch. Each DG unit has a local load and the microgrid supplies one common load connected at PCC. The system parameters are given in Table 5.1.

As mentioned in section 5.1, the voltage controller can be either a low-pass filter (Model 1) or an integrator (Model 2). The characteristics of both topologies in various transients using proposed nonlinear controller are investigated to select best solution. The uncontrolled *synchronverter* with integrator is similar to that presented in [50]. However, the *synchronverter* with a low-pass filter is a fully new topology and shows some benefits over the Model 1. The values of (J) and frequency droop (m) are selected according to (5.12) for the maximum frequency droop and (5.13) which determines the power loop time constant; the higher static

droop the more injected power in islanding mode. In this case, since the static droop for DG1 is higher than DG2 and DG3, it is expected that DG1 produces more power rather than DG1 and DG2. The voltage droop gain is chosen based on the maximum acceptable voltage regulation. The power loop time constants (τ_f) of three DG1, DG2 and DG3 are equal to 0.04 s. In Model 1, the voltage loop time constant (τ_a) is chosen equal to 0.01 s to introduce faster dynamic regarding the power loop.

5.3.1 Case 1: start up

In this case, DG units are connected to the grid at *t*=0. No PLL is used to detect grid 3-phase voltage phase angles. Only one current PLL is used to observe current phase angle. The angle set of three DG units are chosen equal 0.3, 0.2, and 0.2 rad., respectively. Fig. 5.6 exhibits the power waveforms of three DG units during startup. It is observed that a smooth starting operation is obtained using the proposed combined VSC-controller strategy. No severe power overshoot is observed and the transients are well damped and the VSCs can be synchronized with grid. To survey the angle tracking property of the controller, angle variations of the DG units are presented in Fig. 5.7. As expected, the power angles follow their references after sometime. This direct power angle control is an interesting point of the controller in grid connected mode because it can be used as an alternative method to control the generated reactive power and power factor of the DG can be controlled using the angle reference angle. If in grid connected mode reactive power is controlled through a reactive power control loop, this loop makes the system unstable during islanding mode [29] so it should be removed. Actually, the power factors of DG units, which is equal to $\cos\delta$, can be adjusted by proper selection of angle references. In this case, power angles of DG1, DG2 and DG3 are arbitrarily selected equal to 0.3, 0.2 and 0.2, respectively. In typical MG applications, a centralized MG energy management controller can tune these

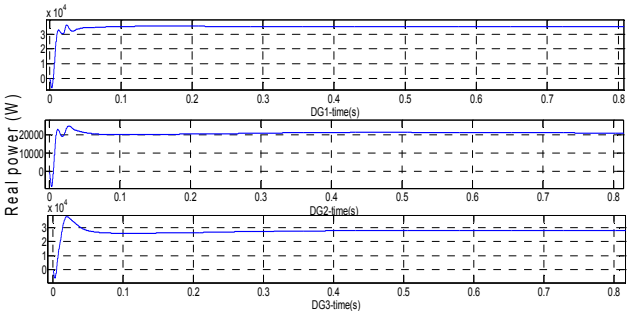

Figure 5-6. Power waveforms of DG units in startup (Model1).

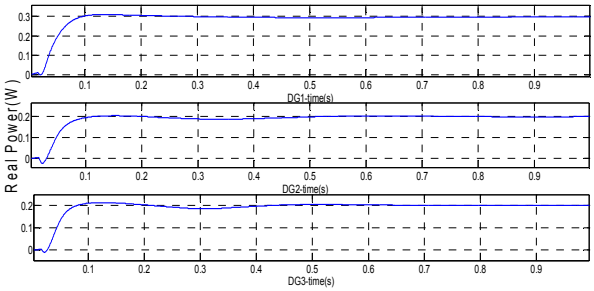

Figure 5-7. Angle tracking of three DG units (Model1).

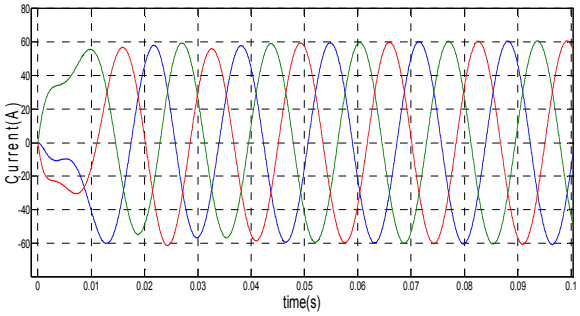

Figure 5-8. Variations of three-phase currents of DG1 during start up (Model1).

values to minimize system losses or improve power sharing. Through the nonlinear controller, the desirable power factor of DG units can be achieved, and accordingly the output reactive power can be adjusted in grid connected mode. As shown in Fig. 5.8, the DG currents waveforms during transients are kept within acceptable limits and no overshoot is observed. Fig. 5.9 exhibits the real power waveforms during startup of DG units using Model 2. Fig. 5.10 illustrates power angle variations of separate DG units whereas Fig. 5.11 shows current waveforms.

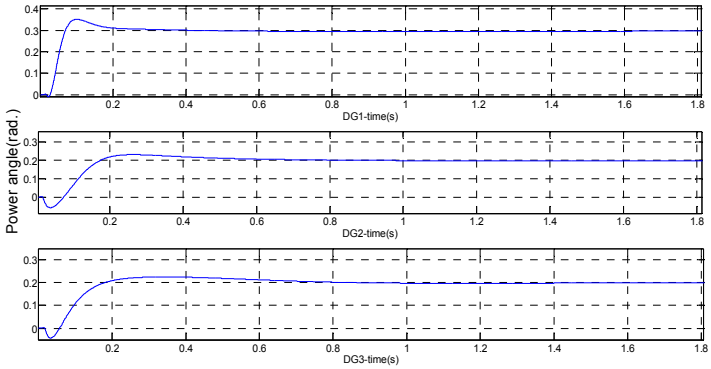

Figure 5-9. Power waveforms of DG units in start-up (Model 2).

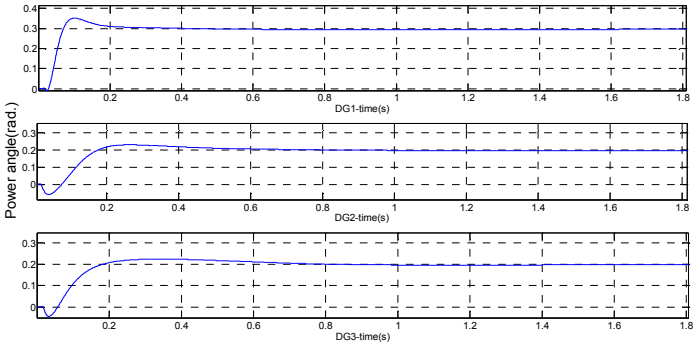

Figure 5-10. Angle tracking of DG units (Model 2).

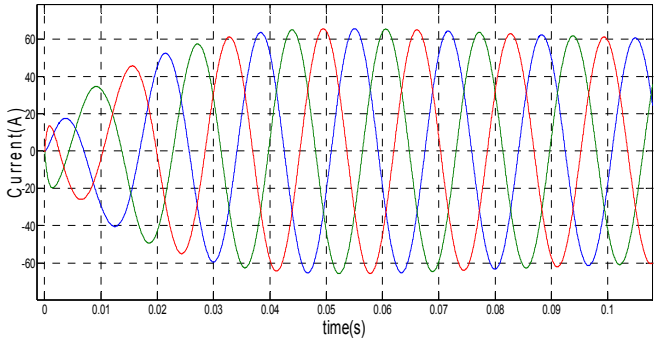

Figure 5-11. Variations of three-phase currents of DG1 during start up (Model 2).

Again a soft start is achieved in this case without any considerable overshoot in power and current. The angle tracking response is also slow. In both cases, the synchronization with the grid is successful which is due to existence of power loop and the nonlinear controller.

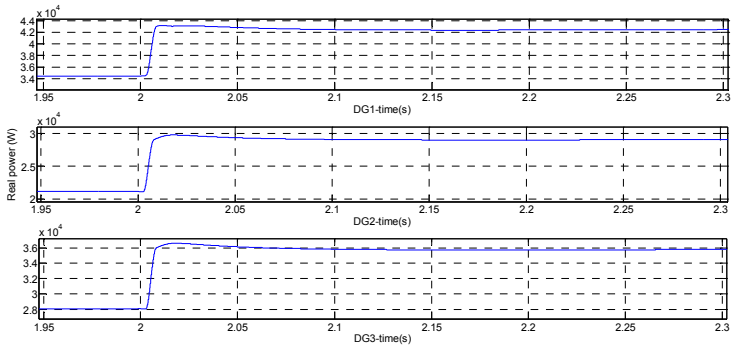

Figure 5-12. Real powers of DG units during transition to islanding (Model1).

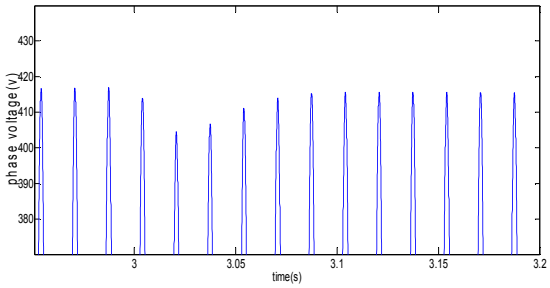

Figure 5-13. Variations of phase voltage amplitude of DG1 during transition to islanding (Model1).

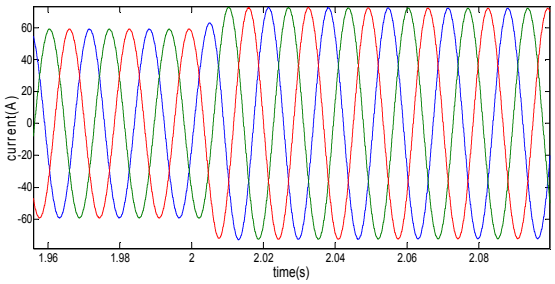

Figure 5-14. Variations of phase currents of DG1 during transition to islanding (Model1).

5.3.2 Case 2: islanding

At *t*=2 s, an islanding is occurred and the microgrid is disconnected from the grid. Figs. 5.12-5.14 show how the real powers, phase voltage and power angles behave during transition from grid connected mode to autonomous mode for Model 1. There is no islanding detection method and system configuration in autonomous operation is the same as that in grid connected mode. The islanding is

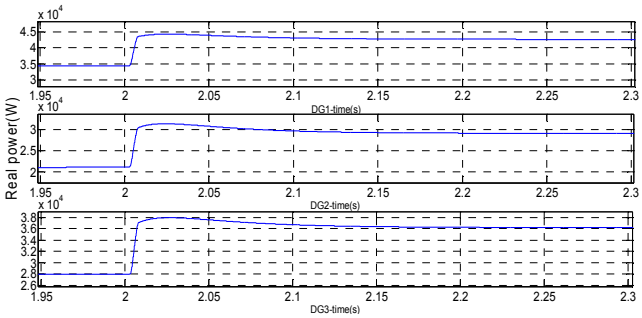

Figure 5-15. Real powers of DG units during transition to islanding (Model2).

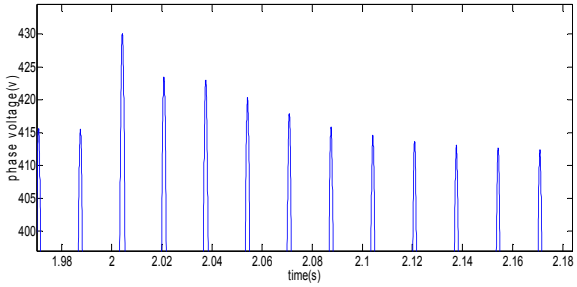

Figure 5-16. Variations of phase voltage amplitude of DG1 during transition to islanding (Model2).

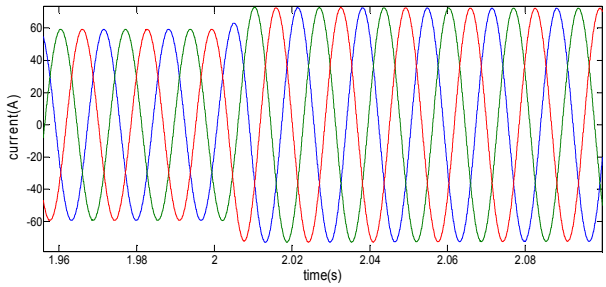

Figure 5-17. Variations of phase currents of DG1 during transition to islanding (Model2).

seen by the proposed controller as a large disturbance. Subsequent to islanding, the DG output powers are immediately increased to provide the local load power. Note that in this case the total local loads power is much higher than the preset DG powers in grid connected mode. This scenario is one of the worst scenarios can take place for a microgrid operation. Figs. 5.12-5.14 reveal that this transition is smooth with minimum overshoot in power and currents regarding their steady state values in islanding and the transients are not severe. The settling time is less

than 0.15 s. It is worth noticing that the existence of virtual rotor momentum of inertia and droop function is inherently beneficial and makes system more damped. To mitigate transients due to islanding and sudden microgrid power increment, the nonlinear controller boosts VSC output voltage to preserve system stability and attenuate power and angle oscillations. The results of power and current variations of Model 2 are given in Figs. 5.15-5.17. It is seen that this model also acts well within switching to islanding without any noticeable transient phenomenon. Another interesting point is the power sharing ratio among DG units. As it is observed, in both cases the generated power of DG units during islanding (45:28:35kW) is very close to the frequency droop constants (m_i=72:42:56).

5.3.3 Case 3: grid restoration

After fault condition is cleared in the grid, it is necessary that microgrid is reconnected to the grid. To investigate effectiveness of the controllers, the microgrid is reconnected to the main grid at t=3 s. Similar to the start up condition, the problem of grid synchronization exists here. The DG power presets are the same as those before islanding. In this case, despite transition to islanding, the DG output powers are suddenly reduced to their presets. Figs. 5.18-5.20 represent power, voltage and current variations subsequent to switching to grid connected mode using Model 1. As expected, the DG outputs powers are decreased and after some transients they converge to their presets values and the oscillations are not severe.

The nonlinear controller reduces VSC voltages during this transition to help DG units reduce their output powers and mitigate power and angle oscillations. However, it seems that Model1 is inherently stable with very good performance. The results of power, current and voltage of Model 2 are shown in Figs. 5.21-5.23.

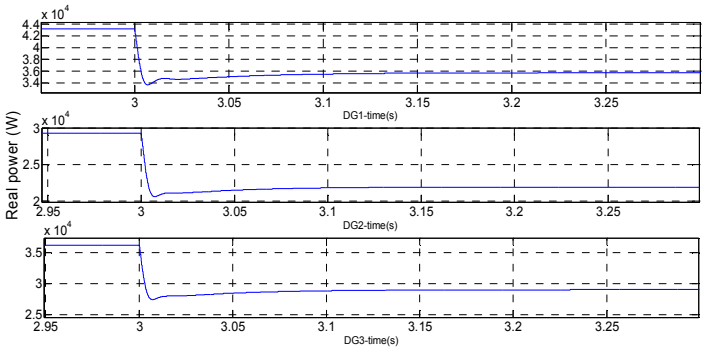

Figure 5-18. Real powers of DG units during grid reconnection (Model1).

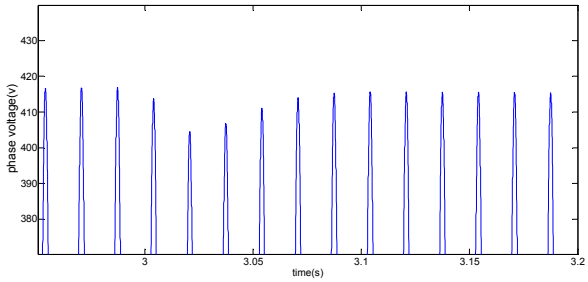

Figure 5-19. Variations of phase voltage amplitude of DG1 during grid reconnection (Model1).

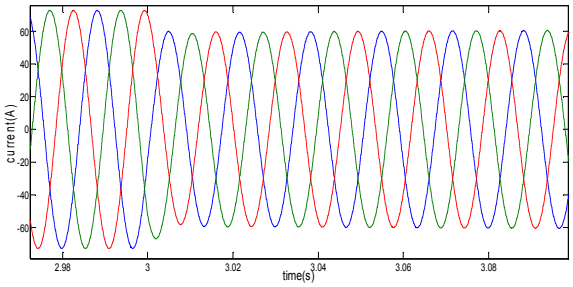

Figure 5-20. Variations of phase currents of DG1 during grid reconnection (Model1).

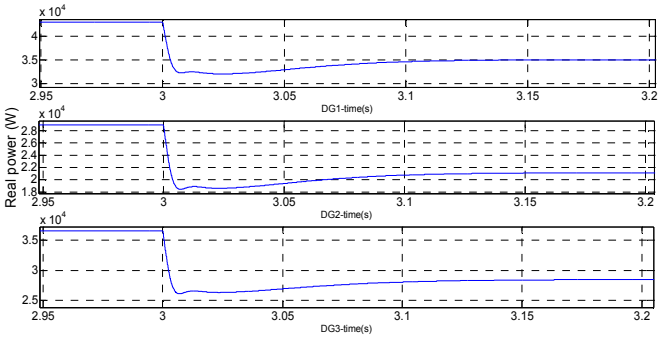

Figure 5-21. Real powers of DG units during grid reconnection (Model 2).

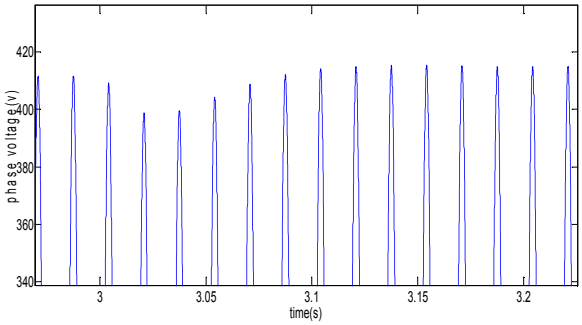

Figure 5-22. Variations of phase voltage amplitude of DG1 during grid reconnection (Model 2).

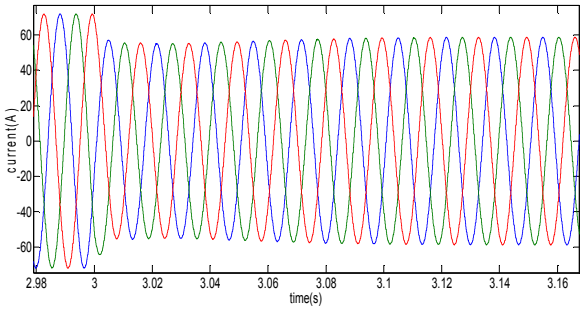

Figure 5-23. Variations of phase currents of DG1 during grid reconnection (Model 2).

Chapter 6 Integrating VSCs to Weak Grids by Nonlinear Power Damping Controller and Multivariable Synchronous Converter[5]

6.1 Background

Among challenging issues facing DG integration is the DG connection to very weak grids (high impedance grids). This objective gains its importance due to high and fast penetration level of off-shore wind turbines and remote PV generation units [55], [111]. In fact, the grid stiffness is a measure of the connecting line capacity to transfer power to a grid [55], [60]. In other words, weak ac grids encounter more difficulty for power flow transfer, thus the maximum amount of available power that can be injected to the grid is more limited. Moreover, the equivalent grid impedance is time-varying as a result of faults and load power variation. To represent the strength of ac systems, the short-circuit capacity ratio (*SCR*) is proposed as an index of an ac system strength relative to the power rating of a VSC. One of major drawbacks of vector control is its limited capability to transfer the rated power in weak grids. For example, in [56], it has been shown that in a weak grid with *SCR*=1, only 40% of the maximum power capacity of a VSC can be utilized. With significant tuning effort of the vector controller parameters and the PLL, this percentage can be increased to 60% [35],[56]. As an alternative, the concept of power synchronization control proposed in [35], [56] is also applicable to enable more power transmission by a VSC by emulating SGs. Basically, SGs do not have any limitations for connection to weak systems, consequently control methods, such as power synchronization which mimic SG's characteristics can effectively enable VSCs integration in very

[5] Part of this chapter is published in *IEEE Transactions on Power Systems* [109] and part is submitted to *IEEE Transactions on Smart Grid* for possible publication [110].

weak grids. It is a simple power loop aims at adjusting the load angle based on the real power error and the supplementary power synchronization controller acts like a virtual PLL by emulating the behaviour of synchronous generators. However, the developed techniques for weak grid integration are based on linearized models and lack the self-synchronization and plug-and-play ability. Also, it suffers from highly real and reactive powers coupling and large steady-state error. In fact, in weak grids, dq-axis components coupling result in poor disturbance rejection and noticeable steady-state error. In other words, in weak grids the single-input single-output (SISO) controllers doesn't offer satisfactory performance and multivariable control is necessary [94-98].

Motivated by the aforementioned challenges, a hybrid nonlinear control of VSCs in weak grids is proposed in this chapter. The controller adopts a power synchronization loop with additional cascaded damping and synchronizing loops. Moreover, a novel current management topology is developed in the second section which adopts a multivariable controller which gives real and reactive power, or equivalently *dq* current components, superior decoupling. The more decoupled behaviour results in better dynamic and static performance in weak grids where real and reactive powers are highly coupled. The current loop is used for current regulation during grid connected mode and it can realize current regulation and current sharing during islanding mode. Thus, current regulation, limitation and sharing are embedded in one compact and neat strategy. It presents some inertia and dynamics for the frequency and load angle similar to synchronous generators (SGs), thus it can be interpreted as virtual multivariable SG or *multivariable synchronous-converter*.

6.2 Power Damping Controller

This chapter focuses on the development of a nonlinear power damping control strategy for VSC units in weak grids with applicability to both grid-connected and

islanded modes of operation. The most critical issue for controller design is the complexity of the system due to nonlinear behaviour of the power transfer dynamics. Usually, linear controllers are developed based on small-signal linearization; however, the control performance inherently depends on specific operating points. In this chapter, a two-level topology with cooperative nonlinear and linear controllers is developed. The first level is a power synchronizing-damping controller. The second level is a nonlinear controller supporting the linear part to enhance system stability in weak grids or during self-synchronization where load angle is large and system works in the nonlinear region. The voltage generation principle is similar to an SG where the voltage frequency and load angle are tuned by power damping-synchronizing loop, whereas the voltage amplitude is given by voltage regulation loop similar to an automatic voltage regulator. The VSC's output real power is controlled directly by adjusting the load angle using the power-damping loop, whereas the reactive power (or alternating voltage) is controlled by adjusting the voltage magnitude. Since the VSC is voltage-controlled one, an inner current loop is not necessary except during large transients such as faults where the control strategy should be changed to current control mode to limit the current amplitude [59]. It should be noted that the proposed outer-loop controller can be also integrated with cascaded voltage-current control loops to ensure high power quality injection and inherent current limitation during faults. In this case, the synchronization angle for dq-frame transformation is obtained from the proposed outer-loop controller instead of a PLL as shown in Fig. 6.1.

6.2.1 Power Damping/Synchronization Control Concept

The base of power damping control of a grid-connected VSC is that the controller provides active damping and synchronization power to attenuate power, frequency and load angle oscillations, and synchronize the VSC with the grid

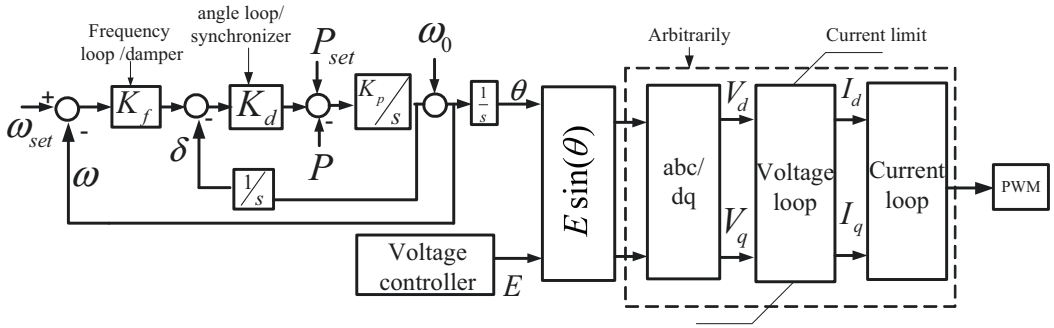

Figure 6-1. The proposed linear control scheme (figure is similar to model-a of figure 2.2 and is shown here for reader convenience).

during steady-state operation. By changing the control strategy of VSCs to comply with the power damping characteristics, VSCs can be integrated to weak grids and also cooperate with SGs in power grids. Fig. 6.1 demonstrates the basic principle of the proposed controller in the polar system. It has three cascaded loops, namely frequency, angle and power loops. Based on the frequency error, the reference of the load angle is determined and the real power reference is obtained as a function of the load angle error. Finally, the power synchronization loop adjusts VSC's instantaneous frequency and load angle. The angle and frequency loops generate synchronization and damping power components for the VSC, thus it can inherently track frequency and angle deviations of the grid and automatically synchronizes itself with the grid. The reference frequency (ω_{set}) in the frequency loop is set equal to the grid frequency, and in steady-state conditions, the VSC produces the reference power (P_{set}). This can be the case in dispatchable DG units or VSC-based HVDC transmission systems. In the case when the primary source falls short to supply the output power, short term energy storage can be added to the dc-link to compensate for the energy shortage during transients. To represent the strength of the connecting line, the *SCR* is defined as

$$SCR = \frac{short\ circuit\ capacity}{rated\ dc\ power} \tag{6.1}$$

where the short-circuit capacity of the ac system (S_{SC}) is given by

$$S_{SC} = \frac{E_0^2}{Z} \tag{6.2}$$

and Z is the circuit equivalent Thevenin impedance. This implies that the weaker the grid, the lower the power transfer capacity of the line. In a weak grid with *SCR*=1.0, the theoretical maximum power transfer capacity is 1.0 p.u. The power-damping control law for a VSC is proposed as

$$\frac{d\Delta\omega}{dt} = -K_p K_f K_d(\omega - \omega_{set}) - K_p K_f \delta - K_p(P - P_{set}) \tag{6.3}$$

As it can be seen, the controller presents controlled dynamics for angle and frequency. To eliminate the switching effect superimposed on the real power, a low-pass filter can be adopted and the filtered power (average power) is fed to the controller. This low-pass filter also gives more degrees of freedom in the control design and may introduce more damping for angle and frequency oscillations. The damping and synchronization power components are given by

$$Damping\ power = \Delta P_{damp} = -K_f K_d \Delta\omega \tag{6.4}$$

$$Synchronizing\ power = \Delta P_{synch} = -K_d \Delta\delta \tag{6.5}$$

The synchronization and damping powers attenuate load angle and frequency fluctuations around equilibrium point and synchronize the VSC with the grid. Beside the inherent synchronization with the grid in steady-state, it is important to take into account that the VSC's frequency and angle are internally available; therefore, there is no need for a PLL in steady-state operation.

6.2.2 Voltage Amplitude Controller

The reactive power of a DG unit can be controlled to 1) regulate the terminal voltage (PV bus) or 2) achieve a specific output reactive power (PQ bus). Fig. 6.2 shows these two different variants. In the first, the voltage reference is compared

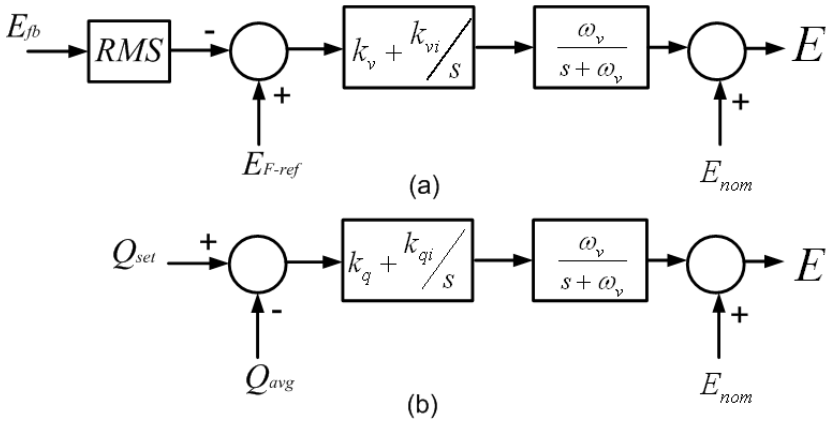

Figure 6-2. Control topologies for output voltage control, (a) P-V bus control and (b) P-Q bus control strategy (the controller is similar to figure 3.3 and is shown here for reader convenience).

to the actual output voltage. In order to track the reference voltage, a proportional-integral (PI) controller is employed aiming at compensating the input error by proper adjustment of VSC's output voltage. The output of the PI controller is processed by a low-pass filter and finally the VSC's voltage amplitude reference is obtained. The low-pass filter plays two different roles; first, it offers more degrees of freedom to tune the low-pass filter cut-off frequency and PI controller parameters such that satisfactory transient and steady-state performances are achieved. In weak grids, usually it is essential to regulate the grid-voltage at the point of common coupling, thus PV bus is the common approach in weak grids [112].

An alternative to the voltage control is reactive power regulation as shown in Fig. 6.2 (b). However, this is not the common case in weak grids. This is due to the fact that the P-Q control strategy significantly degrades DG stability in weak grids as compared to the P-V control [112]. Similar to Fig. 6.2 (a), a low-pass filter exists after the PI controller to mimic the flux decay behaviour of an SG. This low-pass filter allows the suppression of voltage oscillations while voltage tracking time-response and steady-state error are still kept within acceptable

limits. The inner current and voltage loops can be arbitrarily added to the controller for the sake of voltage and current regulation and limiting the current amplitude subsequent to faults as shown in Fig. 6.1.

6.3 System Modeling

To evaluate system dynamic performance in a weak grid, a small-signal stability analysis of a grid-connected VSC is presented in this section. The three-phase power system involves a converter and its controller, RL filter, connecting line and infinite grid. Assuming an ideal VSC, the VSC local voltage is equal to the controller command, thus it is possible to model the VSC and PWM block by an average voltage approach [113]. Therefore, the augmented model of the VSC and its controller can be developed as follows. First, the load angle dynamics equation is given by

$$\Delta\dot{\delta} = \Delta\omega \tag{6.6}$$

The frequency dynamic equation is expressed by (6.3) where ΔP is given by

$$\Delta P = \frac{\partial P}{\partial \delta}\Delta\delta + \frac{\partial P}{\partial E_F}\Delta E_F \tag{6.7}$$

The voltage loop dynamic equation is given by

$$\Delta\dot{E} = -\omega_v \Delta E + \omega_v \Delta v - \omega_v K_v \Delta E_F \tag{6.8}$$

$$\Delta\dot{v} = -K_{vi}\Delta E_F \tag{6.9}$$

where v is the output of the integrator K_{vi}, and E_F is the filter voltage amplitude expressed by

$$\Delta E_F = \frac{E_{Fd0}\Delta E_{Fd} + E_{Fq0}\Delta E_{Fq}}{E_{F0}} \tag{6.10}$$

$$\Delta E_{Fd} = L_c \frac{d\Delta i_d}{dt} + R_c \Delta i_d - \omega_0 L_c \Delta i_q \tag{6.11}$$

$$\Delta E_{Fq} = L_c \frac{d\Delta i_q}{dt} + R_c \Delta i_q + \omega_0 L_c \Delta i_d \tag{6.12}$$

The currents dynamics in the *dq* reference-frame are given by

$$\frac{d\Delta i_d}{dt} = \frac{1}{L}(-E_0 \sin\delta_0 \Delta\delta + \Delta E \cos\delta_0 - R\Delta i_d + \omega_0 L \Delta i_q) \tag{6.13}$$

$$\frac{d\Delta i_q}{dt} = \frac{1}{L}(E_0 \cos\delta_0 \Delta\delta + \Delta E \sin\delta_0 - R\Delta i_q - \omega_0 L \Delta i_d) \tag{6.14}$$

Equations (6.3) and (6.6)-(6.14) represent a sixth-order system and involve all the eigenvalues of the multivariable multi-input multi-output controller and the related power system. Figs. 6.3 and 6.4 show the loci of the eigenvalues as a function of the real power control loop parameters K_f and K_d, respectively. The sixth eigenvalue is not shown here because it appears far away from the imaginary axis. The dominant poles are highly dependent on these parameters. Equations (6.13) and (6.14) introduce two eigenvalues (eigens 4 and 5) which are contributed to the electric circuit and are independent of controller parameters. The right-most eigenvalue is mainly dependent on K_f whereas K_d mainly affects eigenvalue 3. As shown in Fig. 6.4, the position of eigenvalue 2 basically depends on K_{vi}/K_v. During the design process, it should be noted that although lower values of K_f and higher values of K_{vi}/K_v result in higher stability margin and faster response, they may adversely increase the steady-state error especially in weak grids where load angle is large. In other words, in weak grids, acceptable steady-error is achieved at the cost of lower stability margin, thus instability can be yielded during contingencies where load angle swings become large.

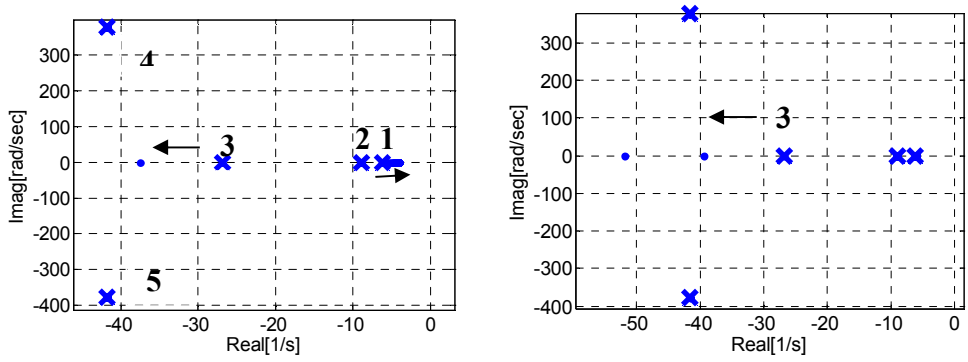

(a) (b)

Figure 6-3. The loci of the eigenvalues as a function of the real power control loop parameters, (a) $0.5 < K_f < 10$, $K_d = 1e5$. (b) $0.5e5 < K_d < 5e5$.

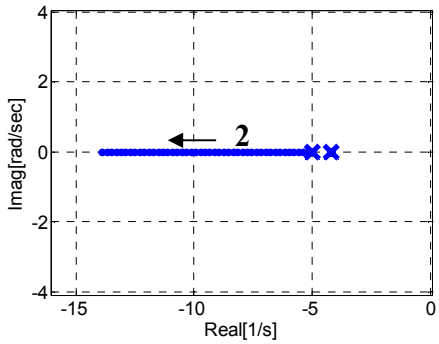

Figure 6-4. The loci of the eigenvalues as a function of the voltage amplitude control loop parameters $0.5 < K_{vi}/K_v < 5$.

6.4 Nonlinear Power Damping Controller

In weak grids with *SCR* less than 4, the load angle is usually large and approaches the steady-state stability limit; accordingly, in the case that a DG unit is required to supply its rated power, power stability may be significantly degraded. The proposed cooperative angle-frequency droop control can enable higher load angles. However, as a linear controller, it cannot guarantee large-signal stability in all operating conditions especially when system dynamics drifts to the nonlinear region. This is more pronounced in sudden large transients such as self-synchronization where any large mismatch between frequency and angle of both sides across the connecting breaker (or re-closer) may contribute to poor

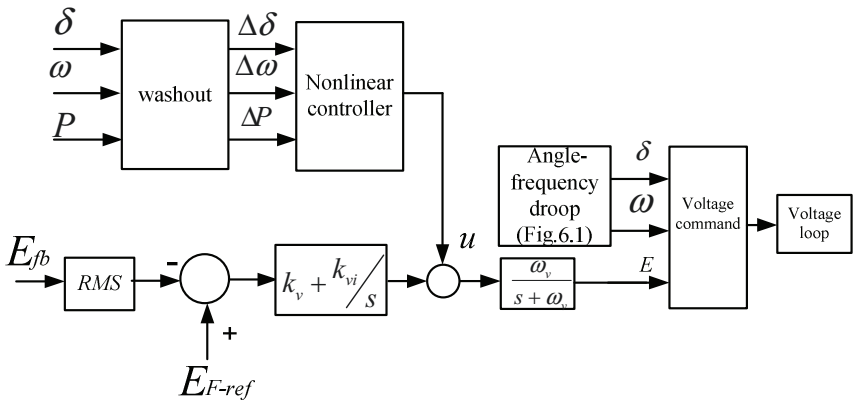

Figure 6-5. Nonlinear supplementary control structure.

performance and even instability. To overcome this issue, a nonlinear back-stepping power damping controller is proposed and augmented with the linear controller as shown in Fig. 6.5.

The overall system model is

$$\dot{x}_1 = x_2 \tag{6.15}$$

$$\dot{x}_2 = a_1 x_1 + a_2 x_2 + a_3 x_3 \tag{6.16}$$

$$\dot{x}_3 = u_f + E\frac{V_L}{X} x_2 \cos x_1 - \omega_v x_3 \tag{6.17}$$

where $a_1 = -K_p K_d$, $a_2 = -K_p K_d K_f$ and $a_3 = -K_p$, and $[x_1, x_2, x_3] = [\Delta\delta, \Delta\omega, \Delta P]$. u_f is defined as $u_f = (u\omega_c V_L \sin x_1)/X$, where u is the control input.

The control objective is to ensure the convergence of the error $e_i = x_i - x_{iref}$ to zero. The first step is to stabilize δ, thus the Lyapunov function

$$V_1 = \frac{1}{2} x_1^2 \tag{6.18}$$

is defined and the reference of frequency deviation value and $\dot{V}_1$ are given by

$$x_{2ref} = -k_1 x_1 \quad k_1 > 0 \tag{6.19}$$

$$\dot{V}_1 = -k_1 x_1^2 + x_1 e_2 \tag{6.20}$$

In the next step, the Lyapunov function is defined as $V_2 = V_1 + \frac{1}{2}e_2^2$ and x_{3ref} is chosen to stabilize V_1 and V_2

$$x_{3ref} = c_1 x_1 + c_2 e_2 \tag{6.21}$$

where

$$c_1 = \frac{(1 - k_1(-a_2 + k_1) + a_1)}{a_3} \tag{6.22}$$

$$c_2 = -\frac{(k_1 + k_2 + a_2)}{a_3}, \quad k_2 > 0 \tag{6.23}$$

Finally, by defining

$$V_3 = V_2 + \frac{1}{2}e_3^2 \tag{6.24}$$

and following the approach presented in chapter 4, it can be shown that the stability of the overall system is confirmed if

$$\begin{aligned} u_f = {} & (A + k_1 \frac{EV_L}{X}\cos x_1)x_1 \\ & + (B - \frac{EV_L}{X}\cos x_1 - a_3)e_2 \\ & + (C - k_3)e_3 \qquad\qquad k_3 > 0 \end{aligned} \tag{6.25}$$

where

$$A = K_f - k_1^2 K_f + k_1 K_d K_f - 2k_1 K_p + \frac{k_1^3}{K_p} - \frac{k_2}{K_p} \tag{6.26}$$

$$B = (k_1 + k_2 - K_d)K_f + \frac{1 - k_1^2 - k_2^2 - k_1 k_2}{K_p} \tag{6.27}$$

$$C = -k_1 - k_2 + K_p K_f \tag{6.28}$$

and V_3 is simplified to

$$\dot{V}_3 = -k_1 x_1^2 - k_2 e_2^2 - k_3 e_3^2 \tag{6.29}$$

Since the nonlinear controller is a supplementary one providing an additional signal for the linear controller, the designs of the controllers are decoupled. The practicability of the nonlinear controller is also discussed in chapter 4.

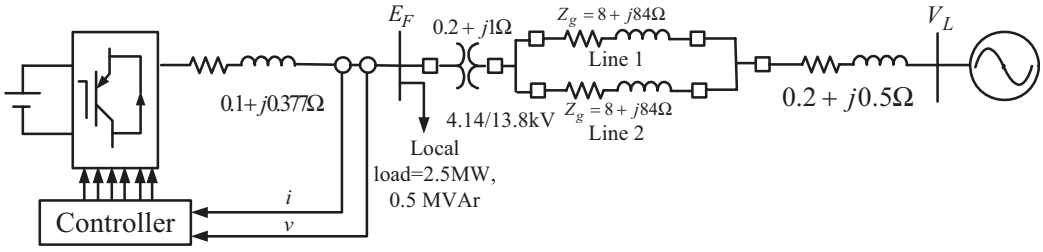

Figure 6-6. The simulated system for nonlinear power damping controller.

TABLE 6-1 PARAMETERS OF THE NONLINEAR POWER DAMPING CONTROLLER

Parameter	Value (SI units)
VSC maximum power capacity	7 MW
VSC voltage (*L-L* rms)	4160 V
E_{f-ref} (*phase maximum voltage*)	3400 V
K_f	5
K_d	1e5
K_p	0.1
K_v	200
K_{vi}	100
ω_v	500

6.5 Evaluation Results for the Nonlinear Power Damping Controller in Weak Grids

Fig. 6.6 shows the configuration of the simulated system. The system is composed of a 7.0 MW VSC, filter, local load, transformer and an interface line connecting the VSC to a grid. It is worth to mention that the impedance $0.2 + j0.5\Omega$ is the equivalent impedance of the stiff source referred to the distribution level. The simulation study was conducted in MATLAB/SIMULINK environment. The controller parameters are presented in Table 6.1. The DG supplies the local load at its output terminal and is connected to a stiff grid through a very weak interface with total impedance of $|Z| = |R + jX| = |4.4 + j43.5| = 43.7\Omega$. Since the connecting line is almost inductive, the power capacity of the interface line is approximated by

$$P \approx \frac{E_F V_L}{X} \sin \delta_{DG} \tag{6.30}$$

where X is the total reactance of the transformer, line and stiff grid ($X = 42 + 1 + 0.5 = 43.5\Omega$). Therefore, the maximum real power transfer capacity of the connecting line is equal $P_{\max} = \frac{13880^2}{43.5} \approx 4.44\,\text{MW}$. Since the local load power at the rated voltage is 2.5 MW, thus the VSC's maximum power capacity is about 7 MW.

The DG works as a PV bus aiming at keeping the filter output voltage (E_F) constant during grid connection. A wide variety of scenarios have been applied to verify the effectiveness of the proposed hybrid nonlinear controller. System performance at low- and high-power references, transition to islanding, self-synchronization, sudden deviation in grid angle and three-phase fault is studied. The advantage of the proposed controller is its flexibility to work in different conditions, i.e. grid-connected and islanded modes without reconfiguration while the nonlinear grid synchronizer enables the plug-and-play feature. The following results can be retained from the simulation results: from sections 6.2 and 6.3 it is drawn that the controller is able to function in both low-power and high-power levels in very weak grids. The SCR of the system is equal to one and as it will be shown that the VSC can easily inject 0.85 p.u. real power to the grid while it has well-damped transient performance. This is in contrast with conventional vector control which can only exchange 0.6 p.u. real power with a grid; otherwise it might face instability [35]. As will be shown in subsection *C*, the controller presents very smooth transition to the islanded mode although there is no any islanding detection process and the controller's configuration and parameters are not changed. The self-synchronization ability of the controller will be presented in subsection 6.5.4 where the re-closer is suddenly closed and the VSC is connected to the grid without a pre-synchronization process which is mandatory in common

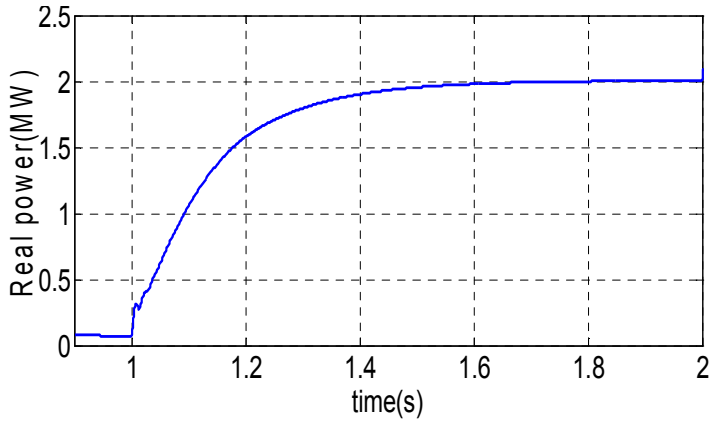

Figure 6-7. Controller performance in low-power injection.

controllers. In this case, the supplementary nonlinear controller preserves the self-synchronization capability with large-signal stability. The controller without supplementary nonlinear control cannot offer self-synchronization capability under large-signal disturbances. Fault-ride-thorough is another advantage of the proposed controller and it will be shown that although the VSC works as a P-V bus, the current flowing in the power circuit during a three-phase fault is limited because of proper load angle adjustment. Moreover, because of its damping and synchronizing powers, it has the ability to work as a virtual PLL and tracks grid's angle and frequency variation as presented in subsection 6.5.5.

6.5.1 Low-Power Injection

To study the behaviour of the controller in a wide range of operating points, it assumed that system initially supplies 80 kW, and at t=1 s, the power reference is increased to 2.0 MW. The real power response is shown in Fig. 8, which shows very smooth transition. The rise-time is about 0.6 s and the system yields accurate reference tracking without any overshoot.

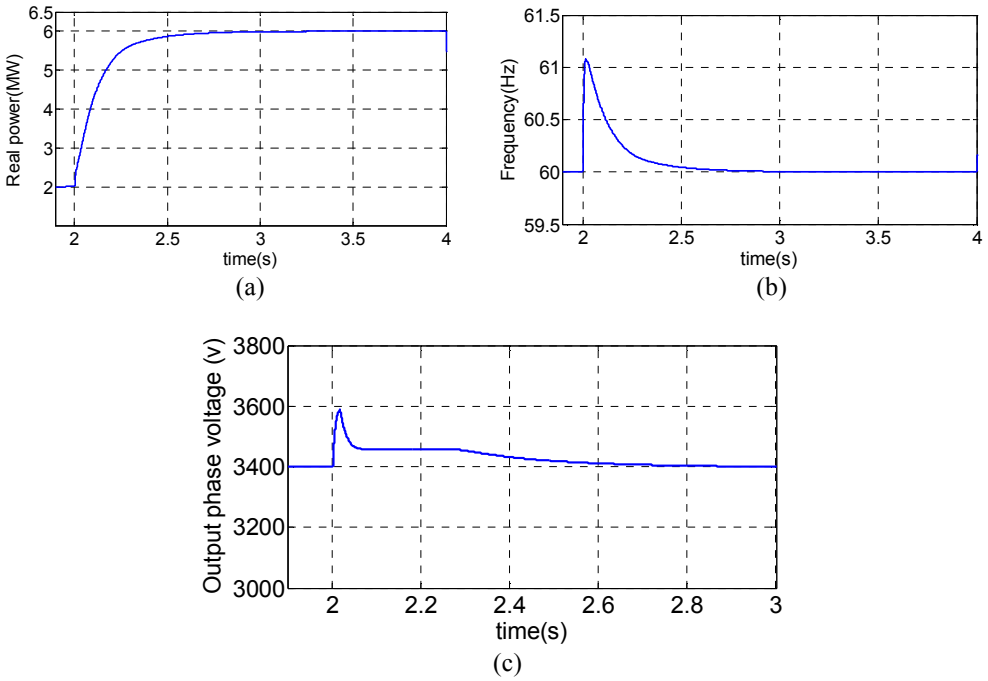

Figure 6-8. Controller performance in high-power injection. (a) Real power and (b) Frequency and (c) Phase-voltage amplitude.

6.5.2 High-Power Injection with High Load Angles

At t=2 s, the reference power is varied from 2.0 MW to 6.0 MW (0.86 p.u.) which is close to the VSC's maximum power capacity at constant voltage operation and a load angle more than 1.03 rad is expected. Fig. 9 (a) shows the real power waveform and Figs. 6.8 (b) and (c) show the frequency and phase voltage amplitude variation, respectively. As it is observed, the response is smooth but with larger rise-time; however, it is still stable with damped response and the output power easily reaches 6.0 MW. The output voltage amplitude of the VSC during this transient is shown Fig. 6.8 (c) presenting the controller action to boost VSC's voltage during load angle variation to enable high real power injection. This is in contrast with the natural behavior of the system which yields voltage sag subsequent to output power increment and consequently higher voltage drop.

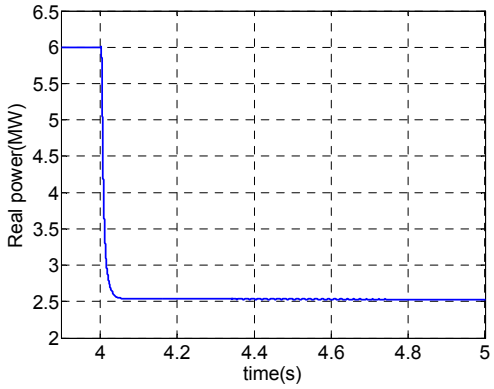

Figure 6-9. Real power waveform during transition to islanding.

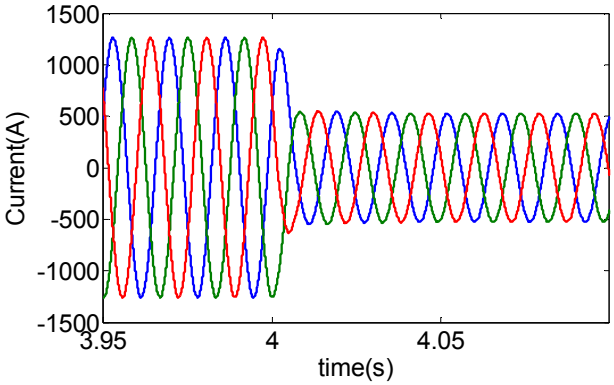

Figure 6-10. Current waveforms subsequent to islanding.

6.5.3 Transition to Islanded Mode

Islanded operation is another scenario that may occur in DG applications to supply local critical load. At t=4 s, the VSC is switched to the islanded mode due to a fault in the grid. No controller-mode switching action or reconfiguration is required. The transition is again seamless without any instability as shown in Fig. 6.9. To achieve faster response, K_f should be reduced; nevertheless, it may cause larger steady-state error in the grid-connected mode. The corresponding current waveforms are shown in Fig. 6.10, which shows smooth and fast transition because of the generality of the controller in both modes.

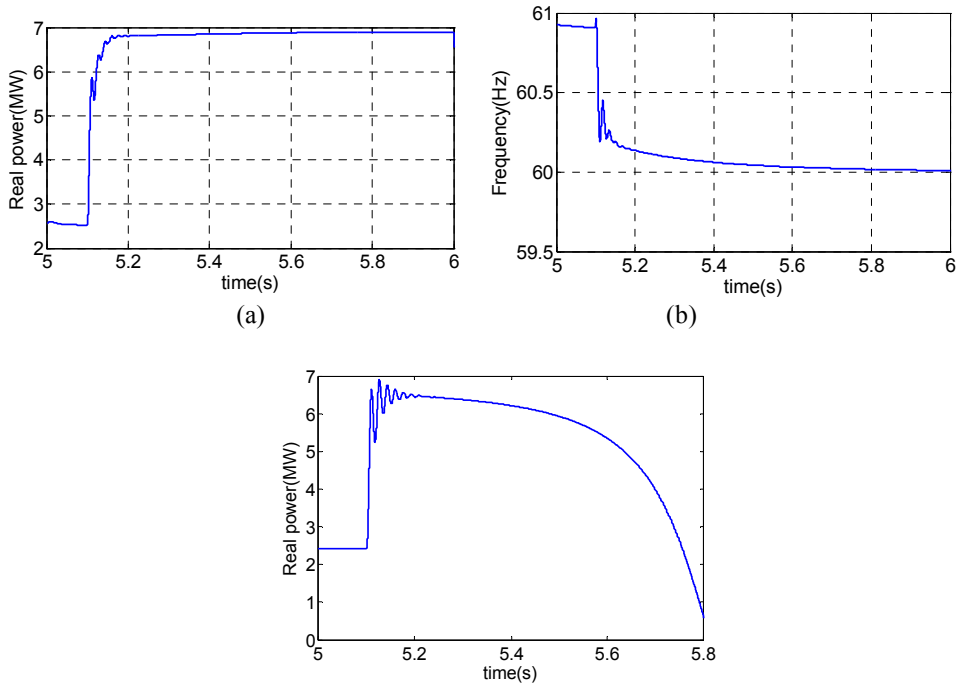

Figure 6-11. System performance during grid restoration, (a) Real power with nonlinear supplementary controller, (b) Frequency, and (c) Real power without the supplementary controller.

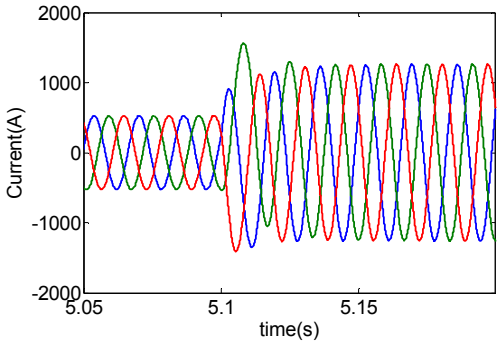

Figure 6-12. Current waveforms subsequent to self-synchronization with supplementary control.

6.5.4 Self-Synchronized Grid Restoration

It is common that a re-closer automatically reconnects a DG unit to the main grid after a special time period (usually 1 s). This is due to the fact that most of faults are cleared after few cycles. In this case, connection occurs without synchronization which may lead to severe transients as a result of frequency and

angle mismatch of both sides of the re-closer at the moment of connection. Weak grids suffer more from the resynchronization transients due to the fact that load angle is inherently large and after grid restoration it may easily move to the nonlinear region and even pass 90° where instability is expected. Figs. 6.11 (a) and (b) show the corresponding waveforms and clearly show that the system with nonlinear controller provides smooth and fast grid connection. This excellent performance occurs under the fact that there is about 0.9 Hz frequency mismatch between the grid and VSC, and the reference power is equal to 6.8 MW corresponding to the load angle1.32 rad. The system response without using the supplementary controller is demonstrated in Fig. 6.11 (c), which shows that the weak grid conditions cause instability. The current waveform of the system with supplementary control is presented in Fig. 6.16, which shows the system well-damped behaviour even in the out-of-phase reclosing scenarios, and verifies the plug-and-play feature of the proposed controller.

6.5.5 Fault-Ride-Through Capability: Disturbance in the Grid Angle

In addition to the high connecting impedance, weak grids may be characterized by sudden deviations in the voltage angle and frequency. Therefore, it is assumed that at t=7.5 s, the power reference is reduced to 4.0 MW, which is not shown here, and at t=7.5 s the angle of grid voltage is abruptly reduced by 0.87 rad. The resulting waveforms of the load angle and phase voltage amplitude are shown in Figs. 6.13 (a) and (b), respectively which verify that the VSC easily catches the angle deviations even in large disturbances without loss of stability and/or poor performance. It causes an overshoot in the output power and the load angle that is damped within 0.5 s. This is a very potentially interesting feature of the controller where it acts as a virtual PLL, and automatically tracks grid frequency and angle deviations. In this case, as shown in Fig. 6.13 (b), the output voltage amplitude is suddenly reduced to keep the output power limited. This is due to

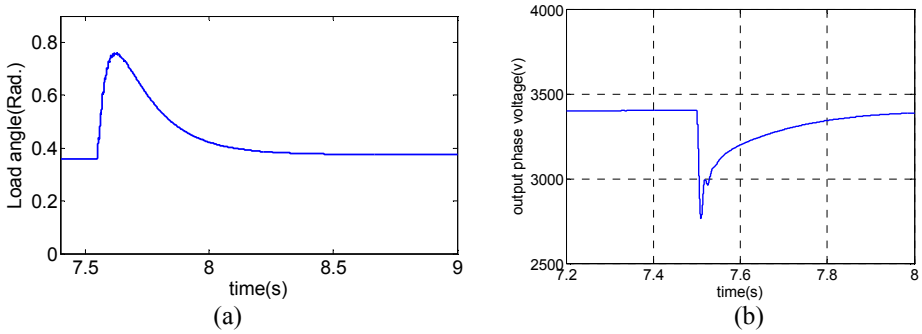

Figure 6-13. Load angle variation subsequent to disturbance in the grid angle.

the fact that a lag in the grid voltage angle results in sudden output power increment, thus the output voltage must be reduced to preserve real power stability.

6.5.6 Fault-Ride-Through Capability: Three-Phase Fault

Fig. 6.14 shows the VSC's fault-ride-through performance when a three-phase bolted fault occurs near to the end of connecting line 2. The fault starts at t=9 s and after 0.16 s, line two is disconnected from the rest of the grid by the protection system. Fig. 6.14 (a) shows the real power variation, and reveals that the output real power is limited to 2.9 MW. Note that about 2.5 MW of this power is absorbed by the local load. Figs. 6.14 (b) and (c) show the waveforms of VSC's instantaneous output current and amplitude of the output voltage, respectively. As it is seen, the converter's current is limited to 1420 A which is within the acceptable limits and less than the nominal current; therefore, the VSC is not subjected to over-current during three-phase fault. It should be noted since the VSC acts as a P-V bus, during the fault it aims at keeping the output voltage constant while the current amplitude is limited by proper adjustment of the load angle and inner current limiter. In fact, power damping/synchronization loops aim at limiting the real power and consequently the current flowing in the VSC circuit by proper adjustment of the load angle, whereas the voltage regulation loop tries

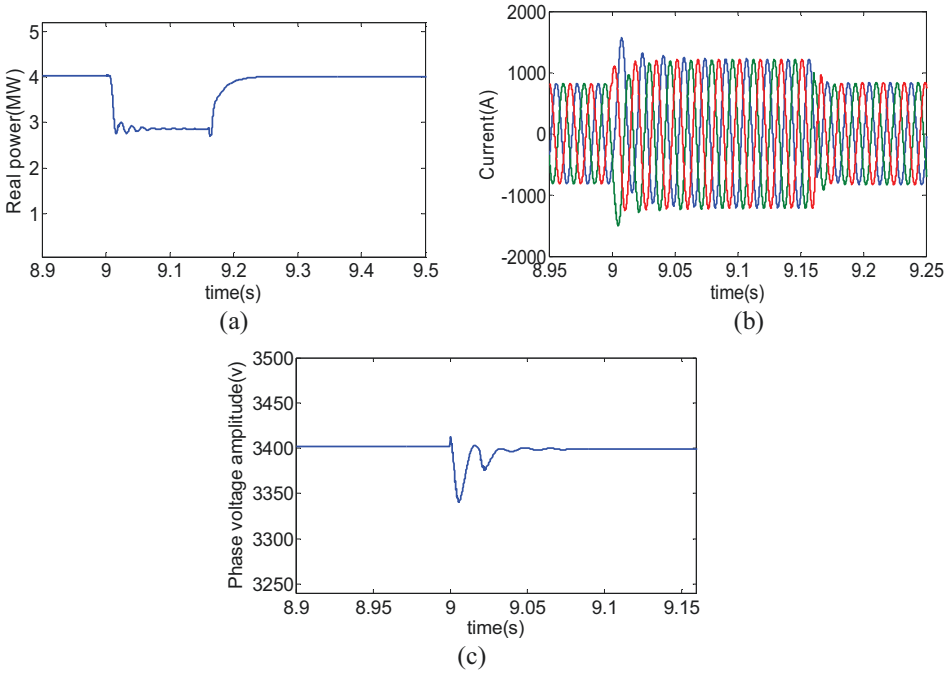

Figure 6-14. System waveforms subsequent to a three-phase fault, (a) Real power, (b) Instantaneous current waveforms and (c) amplitude of the phase-voltage.

to keep the local bus voltage constant. The nonlinear supplementary controller also helps the power damping/ synchronization loops to undergo the load angle and real power deviations. The real power waveform is smooth and confined during the fault. During the fault, the voltage drops and reactive power increases. At t=9.16 s, the breakers of both sides of the connecting line 2 act and the line is decoupled from the rest of the grid. Accordingly, fault is cleared and the line impedance is increased to $8 + j84\Omega$, which is twice the initial value representing very weak system. This separation event is another large-signal transient occurring in the system. Upon disconnection of line 2 at t=9.16 s, voltage, real power and current return to their initial conditions before the fault but in a different operating point since total interfacing impedance is doubled as compared to the pre-fault condition. It should be noted that in these scenarios, the reference real power is kept constant at 4.0 MW. This scenario verifies the robustness of the

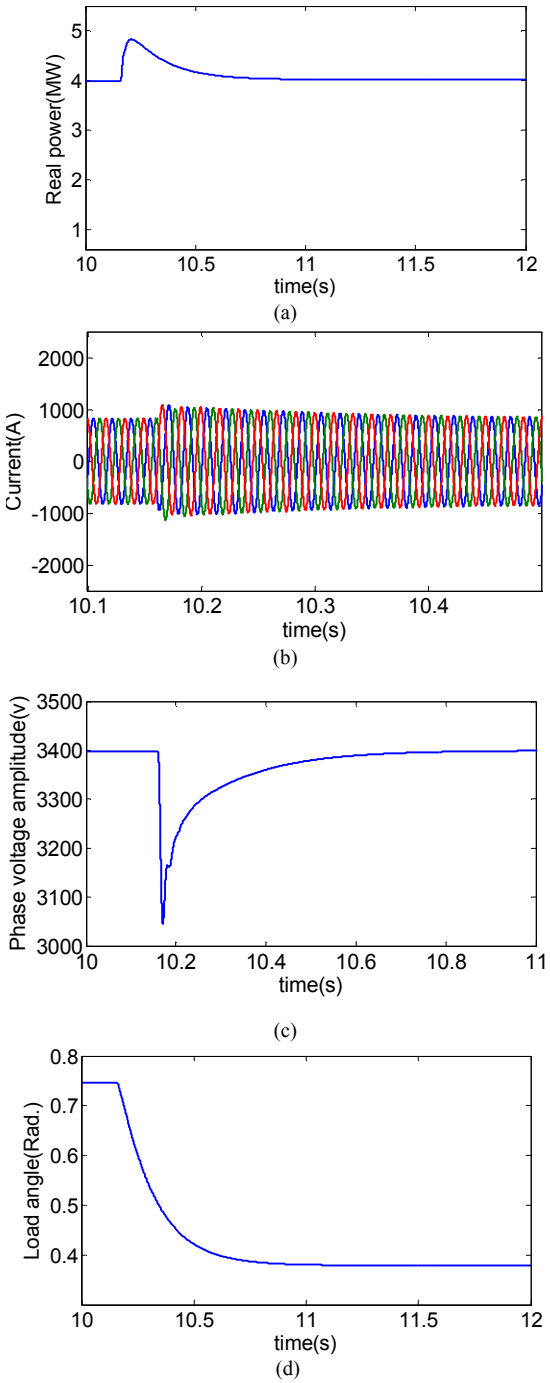

Figure 6-15. System waveforms subsequent to reconnection of line 2, (a) Real power, (b) Instantaneous current, (c) Amplitude of the output phase-voltage and (d) Load angle.

proposed controller against network system uncertainties because it introduces sudden large variation in total line impedance. It is supposed the fault is cleared at t=10.16 s when line 2 is again switched into the circuit. The corresponding waveforms subsequent to reconnection of line 2, such as real power, current, amplitude of the phase-voltage and load angle are presented in Fig. 6.15. It should be noted that this case is different from the mal-synchronization case presented in subsection 6.5.4, because only one line is out and system has kept its synchronization with the main grid during all contingencies reported in subsection 6.5.6. After the re-closer of line 2 is activated at t=10.16 s, the overall system settles down in less than 0.7s. After reconnection of line 2, the VSC's real power jumps to 4.8 MW, which is due to sudden line impedance reduction but it recovers its steady state value within 0.5 s. The voltage amplitude is reduced during this disturbance to prevent high current and power flow to the line due to immediate line impedance reduction. The reconnection of connecting line 2 is smooth and all the waveforms present well-damped characteristics. Due to proper voltage regulation, the overshoot in the real power and current is very limited although the impedance variation is large. The load angle is reduced from 0.75 rad to 0.38 rad which is equal to its pre-fault value.

6.6 Proposed Current Management of Weak Microgrids with Multivariable Droop-Based Synchronous Converter

As mentioned in chapter 2, as a variant to the frequency and voltage droop versus the active and reactive powers, it is possible to control direct (i_d) and quadrant (i_q) currents for load sharing in MGs. This due to the fact that in the steady state the real power is proportional to i_d and the reactive power is controllable through i_q. The characteristic equations in this case are compensated to (2.11-2.14).

One of major drawbacks of frequency drooping is the permanent frequency offset which may significantly degrade the power quality. As mentioned in chapter 4, another alternative for the load sharing is angle drooping in which the load angle is directly adjusted according to the output power without a need for frequency change. Although this method realizes constant frequency operation, there are serious disadvantages associated with this method such as need for a general clock to synchronize different VSCs which necessitates communication infrastructure and also it suffers from poor power sharing and there is no systematic approach to tune the load angle references [41],[75]. This chapter strives to present a neat and compact multivariable controller-manager for weak microgrids which integrates current regulation, limitation and sharing with steady state constant frequency operation and dynamics similar to SGs. The main benefit of controller is ability to work in very weak MGs with d- and q-axis decoupling capability because of its multivariable structure.

In the following, the design procedure of the proposed multivariable controller is proposed. The controller is developed in the polar framework, via the loop shaping technique; therefore its outputs are as voltage amplitude, frequency and angle of the VSC, which can be easily synthesized via a pulse-with modulator. Accordingly, using the load-angle and voltage amplitude as the electric system input, the main power circuit can be linearized in the following input-output form

$$\begin{bmatrix} \Delta i_d \\ \Delta i_q \end{bmatrix} = \begin{bmatrix} G_{id\delta} & G_{idE} \\ G_{iq\delta} & G_{iqE} \end{bmatrix} \begin{bmatrix} \Delta\delta \\ \Delta E \end{bmatrix} \tag{6.31}$$

The transfer matrix G_{id-iq} can be named the Jacobian matrix transfer function. In the power circuit, it is assumed that there is no capacitor in the output filter which is common in high power applications and the main focus of this chapter. To obtain the elements of the Jacobian matrix transfer function, the governing equation in space-phasor format is

$$L\frac{di}{dt} = E - V - Ri - j\omega Li \tag{6.32}$$

This can be written in *dq* frame as

$$L\frac{di_d}{dt} = E\cos\delta - V - Ri_d + \omega_0 Li_q \tag{6.33}$$

$$L\frac{di_q}{dt} = E\sin\delta - Ri_q - \omega_0 Li_d \tag{6.34}$$

Linearization of (6.33) and (6.34) yields

$$L\frac{d\Delta i_d}{dt} = -E_0\sin\delta_0\Delta\delta + \cos\delta_0\Delta E - R\Delta i_d + \omega_0 L\Delta i_q \tag{6.35}$$

$$L\frac{d\Delta i_q}{dt} = E_0\cos\delta_0\Delta\delta + \sin\delta_0\Delta E - R\Delta i_q - \omega_0 L\Delta i_d \tag{6.36}$$

where the operating point is denoted by subscript "0" and deviations around the operating point are demonstrated by the prefix "Δ". By some simplification and applying Laplace transform, the transfer functions of Δi_d versus $\Delta\delta$ and ΔE, and Δi_q versus $\Delta\delta$ and ΔE are obtained as

$$\Delta i_d = E_0\frac{\omega_0 L\cos\delta_0 - \sin\delta_0(Ls+R)}{(Ls+R)^2 + (\omega_0 L)^2}\Delta\delta + \frac{\omega_0 L\sin\delta_0 + cos\delta_0(Ls+R)}{(Ls+R)^2 + (\omega_0 L)^2}\Delta E \tag{6.37}$$

$$\Delta i_q = E_0\frac{\omega_0 L\sin\delta_0 + \cos\delta_0(Ls+R)}{(Ls+R)^2 + (\omega_0 L)^2}\Delta\delta + \frac{-\omega_0 L\cos\delta_0 + \sin\delta_0(Ls+R)}{(Ls+R)^2 + (\omega_0 L)^2}\Delta E \tag{6.38}$$

Therefore, the transfer function $G_{id\delta}$, G_{idE}, $G_{iq\delta}$ and G_{iqE} are obtained by (6.37) and (6.38).

In this chapter, the concept of multivariable damping and synchronizing current is developed. In the multivariable damping-synchronizing current control i_d and

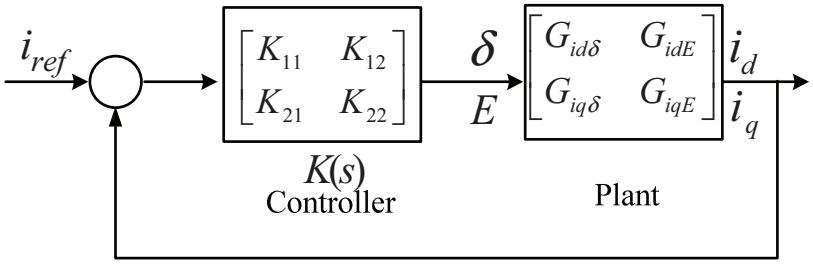

Figure 6-16. Interconnection of the controller and the plant.

are adjustable through the load angle and voltage amplitude (E) via a multivariable controller $K(s)$

$$K(s)=\begin{bmatrix} K_{11}(s) & K_{12}(s) \\ K_{21}(s) & K_{22}(s) \end{bmatrix} \tag{6.39}$$

Fig. 6.16 presents the basic schematic view of the multivariable feedback current control method. The main goal of the mutual terms K_{12} and K_{21} is providing decoupled performance in weak MGs whereas K_{11} is responsible for producing damping and synchronizing currents, *d*-axis current regulation and introducing some inertia and dynamics for frequency in both grid connected and islanding modes. It also generates the preset *d*-axis current in grid connected mode and shares it among DG units in islanding. Moreover, K_{22} aims at regulating *q*-axis current in both operational modes and *q*-axis current sharing during islanding. Adopting (6.35) and (6.36), the state-space model of the system can be given by

$$\begin{pmatrix} d\Delta i_d/dt \\ d\Delta i_q/dt \end{pmatrix} = A\begin{pmatrix} \Delta i_d \\ \Delta i_q \end{pmatrix} + B\begin{pmatrix} \Delta\delta \\ \Delta E \end{pmatrix} \tag{6.40}$$

where

$$A=\begin{pmatrix} -R/L & +\omega_0 \\ -\omega_0 & -R/L \end{pmatrix},\ B=\begin{pmatrix} -E_0\sin\delta_0 & \cos\delta_0 \\ E_0\cos\delta_0 & \sin\delta_0 \end{pmatrix} \tag{6.41}$$

By applying Laplace transform, the plant transfer function is deduced by

$$G(s)=(sI-A)^{-1}B \tag{6.42}$$

Now, the desirable shape of overall system open loop transfer functions are

defined as

$$K(s)G(s)=\begin{pmatrix}\dfrac{-K_p}{s^2+2\xi\omega_n s+\omega_n^2} & 0\\ 0 & \dfrac{-K_q}{s+\omega_q}\end{pmatrix} \tag{6.43}$$

The mutual terms of the overall system, i.e. the controller and the plant, are set equal to zero for the sake of decoupling between i_d and i_q. In this case, i_d is just controllable through the load angle and i_q is just affected by VSC's voltage amplitude. By proper selection of ξ and ω_n, the transient responses of i_d and frequency are tuned while ω_q mainly influences the stability and transient performance of the voltage loop. Substituting $G(s)$ in (6.43) yields the desirable controller shape as follows

$$K(s)=\begin{pmatrix}\dfrac{-K_p}{s^2+2\xi\omega_n s+\omega_n^2} & 0\\ 0 & \dfrac{-K_q}{s+\omega_q}\end{pmatrix}B^{-1}(sI-A) \tag{6.44}$$

Substituting B and A from (6.41) in (6.44) results in

$$K(s)=\begin{pmatrix}\dfrac{-K_p(a_{11}s+b_{11})}{s^2+2\xi\omega_n s+\omega_n^2} & \dfrac{-K_p(a_{12}s+b_{12})}{s^2+2\xi\omega_n s+\omega_n^2}\\ \dfrac{-K_q(a_{21}s+b_{21})}{s+\omega_q} & \dfrac{-K_q(a_{22}s+b_{22})}{s+\omega_q}\end{pmatrix} \tag{6.45}$$

where

$$a_{11}=-\sin\delta_0/E_0 \tag{6.46.a}$$
$$b_{11}=(-R\sin\delta_0/L\,E_0)+\cos\delta_0\omega_0/E_0 \tag{6.46.b}$$
$$a_{21}=\cos\delta_0/E_0 \tag{6.46.c}$$
$$b_{21}=(R\cos\delta_0/L\,E_0)+\sin\delta_0\omega_0/E_0 \tag{6.46.d}$$
$$a_{12}=\cos\delta_0 \tag{6.46.e}$$
$$b_{12}=(R\cos\delta_0/L)+\sin\delta_0\omega_0 \tag{6.46.f}$$
$$a_{12}=\sin\delta_0 \tag{6.46.g}$$
$$b_{12}=(R\sin\delta_0/L)-\cos\delta_0\omega_0$$

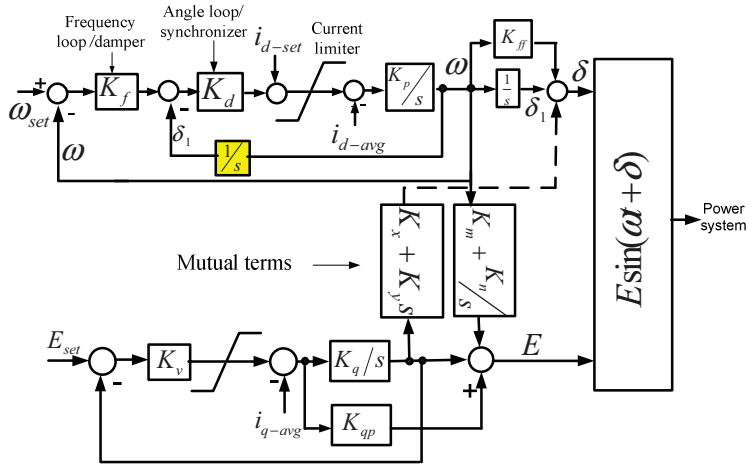

(a)

(b)

Figure 6-17. Realization of synchronous-converter topologies, (a) complete multivariable controller with mutual terms, (b) the basic core controller.

6.6.1 D-axis Current Control

Fig. 6.17 exhibits the realization of the proposed controller and its basic core controller. As it is seen, there are two individual control channels with mutual controllers connecting two individual controllers aiming at decoupling d- and q-axis currents and two channels. In the first channel, which is used for load angle control, there is second order controllers whereas in the second channel called voltage amplitude control a low-pass filter is adopted as the controller.

The load-angle controller has three cascaded control loops, namely frequency,

angle and current loops. The frequency and angle loops determine the current reference for the current loop and the current loop adjusts the frequency and load angle such that the VSC generates the reference current. There is saturation block to constraint the current reference and consequently current flowing to the electric circuit, thus an inherent current limitation mechanism is embedded within the controller. With some simplification the transfer function $\Delta\delta_1$ versus Δi_d is calculated as

$$\frac{\Delta\delta_1}{\Delta i_d} = \frac{-K_p}{s^2 + K_p K_d K_f s + K_p K_d} \tag{6.47}$$

which is similar to the frequency dynamics of an SG:

$$J\frac{d^2\Delta\delta}{dt^2} + K_m\frac{d\Delta\delta}{dt} + K_s\Delta\delta = -\Delta P_{load} \tag{6.48}$$

where K_m and K_s are damping and synchronizing constants, respectively. Also i_d in the synchronous-converter is replaced with P_{load} in the SG and K_p μ $1/J$, $K_f K_d$ μ K_m and K_d μ K_s.

The d-axis current deviation is written as a function of the frequency deviation:

$$\frac{\Delta i_{dref}}{\Delta\omega} = -K_d\left(\frac{1}{T_i s} + 1\right),\ \ T_i = \frac{1}{K_f}. \tag{6.49}$$

The integrator time constant (T_i) is designed according to the well-known phase margin criterion. To have faster response, it is recommended to reduce the size of K_f; however, it should be noted it results in higher steady-state error. For given values of ω_n, ξ and T_i, the controller parameters K_f, K_d and K_p can be easily calculated. A criterion is to choose ω_n much lower than the switching frequency ω_s. Therefore, K_p plays the role of inverse of rotor momentum of inertia of an SG. Equation (6.47) indicates the small-signal stability of the load angle control loop is tunable through constants where $\omega_n = \sqrt{K_p K_d}$ and $\zeta = 0.5K_f\sqrt{K_p K_d}$. The

open loop frequency response and also the small-signal stability of the load-angle control loop is tunable through constants K_p, K_d and K_f in equation (24) where $\omega_n = \sqrt{K_p K_d}$ and $\zeta = 0.5 K_f \sqrt{K_p K_d}$. In grid-connected mode, the VSC generates the *d*-axis preset current (i_{d-set}). Since VSC's frequency and load angle is internally available and also the controller produces some inherent synchronizing and damping current, it automatically synchronizes itself with the grid. The first aims at undergoing angle oscillations and the latter damps frequency oscillations. The synchronizing and damping currents are given by

$$Damping\,current = -K_f K_d \Delta\omega \tag{6.50}$$

$$Synchronizing\,current = -K_d \Delta\delta. \tag{6.51}$$

In this case, the controller presents damping and synchronizing current components instead of synchronizing power in the conventional SGs. During islanding, the first control channel plays the role of sharing d-axis current which proportional to the real power among DG units. To investigate this fact, it should be noted that input to the integrator K_p in steady state is zero, therefore

$$i_d = i_{d-set} + K_f K_d(\omega_{set} - \omega) - K_d \delta_1 = i^*_{d-set} - K_f K_d \omega - K_d \delta_1 \tag{6.52}$$

where $i^*_{d-set} = i_{d-set} + K_f K_d \omega_{ref}$. The interesting point here is the application of drooping both frequency and angle to realize current sharing which indicates hybrid droop for current sharing. Also, as it will be shown later, existence of an integrator the angle loop results in steady state constant frequency operation in an islanded MG. In fact, since

$$\Delta i_{dref} = -K_f K_d \Delta\omega - K_d \Delta\delta = -K_f K_d \Delta\omega - K_d \frac{\Delta\omega}{s} \tag{6.53}$$

$\Delta\omega$ becomes zero in steady state.

In Fig. 6.17 based on a given and predetermined K_p, the control parameters K_{ff}, K_m and K_n are determined as

$$K_{ff} = a_{11} / b_{11}, \tag{6.54.a}$$

$$K_m = a_{12} / b_{11}, \tag{6.54.b}$$

$$K_n = b_{12} / b_{11}. \tag{6.54.c}$$

If these coefficients are chosen according to (6.54), the controller shape of (6.45) is automatically realized. In other words, the parameters are adjusted using (6.54) such that the controller takes the form of (6.45).It should be noted that these control parameters are evaluated at a given operating point; however, the multivariable nature of the proposed controller gives the designer more degrees of freedom to determine the desirable values of these parameters to realize satisfactory performance at different operating conditions and line parameters as will be shown by simulation results. The feed-forward term (K_{ff}) is useful to improve transient performance since it directly adjusts the load-angle as a function of the *d*-axis current error without using frequency as a medium. The mutual terms K_m and K_n are employed for the sake of decoupling i_d from i_q.

6.6.2 Q-axis Current Control

The second control channel is devoted to control of voltage amplitude as a function of *q*-axis current i_q. The transfer function of ΔE_1 versus Δi_q is obtained based on Fig. 6.17 as

$$\frac{\Delta E_1}{\Delta i_q} = \frac{-K_q}{s + \omega_q}, \ \omega_q = K_q K_v. \tag{6.55}$$

similar to the *d*-axis loop, the transient response and its time constant can be adjusted by ω_q which is equal to multiplication of control constants K_q and K_v. The constant K_q provides q-axis current sharing and current regulation during islanding mode. This can be shown by the fact that in steady state, the input to the

integrator K_q is zero. Therefore,

$$i_q = K_v(E_{set} - E) \tag{6.56}$$

and consequently,

$$E_1 = E_1^0 - ni_q,\ E_1^0 = K_v E_{ref}\ \ and\ \ n = 1/K_v \tag{6.57}$$

As a rule of thumb, the size of K_v can be calculated according to the maximum allowable voltage drop:

$$K_v = \frac{\Delta i_{q-\max}}{\Delta E_{\max}} \tag{6.58}$$

After determining K_v, the size of K_q is calculated by desirable bandwidth (ω_q) using (6.55). Along with integrator gain K_q, there is a feed-forward term K_{qp}, which can be obtained as

$$K_{qp} = \frac{a_{22}}{b_{22}} K_q \tag{6.59}$$

Thus, after designing K_q, the feed-forward K_{qp} is automatically obtained at a given operating point. Furthermore, the decoupling terms in the *q*-channel are given by

$$K_x = \frac{b_{21}}{b_{22}} \tag{6.60.a}$$

$$K_y = \frac{a_{21}}{b_{22}} \tag{6.60.b}$$

Similar to the *d*-axis current loop shaping, the coefficients in (6.59) and (6.60) are adjusted in such a way that controller of (6.45) is fulfilled.

6.7 Evaluation Results for the Multivariable Synchronous Converter

This section presents a set of simulation results which verify the performance and effectiveness of the multivariable controller. The simulations are conducted in MATLAB/SIMULINK environment. The simulated system is shown in Fig. 6.18, which represents a grid- connected MG system composed of two VSCs connected

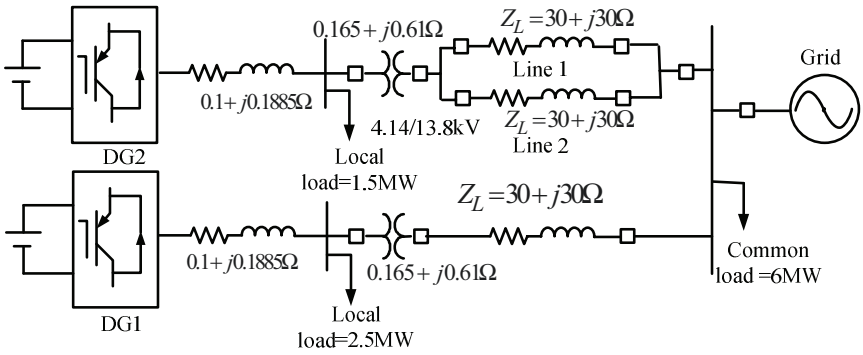

Figure 6-18. The simulated system.

Table 6-2 Parameters of multivariable controller

Parameter	DG1	DG2
VSC maximum power capacity	7 MW	7MW
VSC voltage (*L-L* rms)	4140 v	4140v
E_{set}	3450 v	3450v
K_f	1	1
K_d	30	30
K_p	1	1
K_v	30	30
K_q	20	20
K_{qp}	12	12

to local and common loads via long lines. The MG can work in the isolated mode as well. In should be noted that no PLL is used after initial synchronization and VSC automatically synchronizes itself with the grid. The VSCs' parameters and controllers are presented in Table 6.2. The connecting line of DG 1 represents is a very weak grid with $Z_{L1} = 30 + j30\Omega$ indicating equal reactance and resistance. The connecting interface of DG2 involves two similar parallel lines; therefore the total connecting impedance is $Z_{L2} = 15 + j15\Omega$. To gauge the grid strength, the *SCR* is used which was defined in (6.1) and (6.2). Accordingly, the *SCR* of DG1's connecting line is obtained as $S_{SC1} = \frac{13800^2}{42.4} \approx 4.5 MVA$ and considering that the local load power is 2.5 *MW*, the maximum power capacity of DG1 is 7 *MW*

corresponding to $i_d \approx 1400\,A$ and SCR =1. Using similar approach the power capacity of DG2 is $S_{SC2} = \frac{13800^2}{21.2} \approx 9\,MVA$, with addition of 1.5 MW of the local load the total power capacity becomes 10.5 MW and consequently SCR=1.5. The controller topologies shown in Fig. 6.17 are employed to generate the preset d-axis currents in the grid-connected mode and share it during islanding equally. The voltage drop versus i_q is adopted for both operational modes. A sequence of several events is conducted to test system dynamics under wide and typical set of contingencies. It should be noted that no PLL is used during simulations and controller automatically synchronizes itself with grid due to synchronizing and damping currents.

6.7.1 High- and Medium-Power Applications

To investigate system performance in high- and medium-power applications, the set-point currents (i_{dset}) of both units are increased from 350 A to 1300 A at t=0.5 s and at t=1 s it is reduced to 1000 A. The corresponding waveforms of i_d of both the core decoupled controller and the multivariable controller is shown in Fig. 6.19, which shows very smooth transition in all the waveforms for the multivariable controller. The steady state error for the case $i_{dset1} = i_{dset2} = 1300$ A is about 0.3% while in the basic core controller the steady-state error arises to 3.3%. The considerable steady state error is due to high coupling between i_d and i_q or equivalently real and reactive power in the weak grids where load angle is large. This problem is more pronounced in the resistive lines. With a strong coupling of i_d and i_q, they cannot be regulated independently with the load angle and voltage amplitude, therefore in the system with multivariable controller. The rising time is less than 0.2 s and no overshoot is observed in the current. On the contrary, in the system with the core controller, the transient response is extremely oscillatory

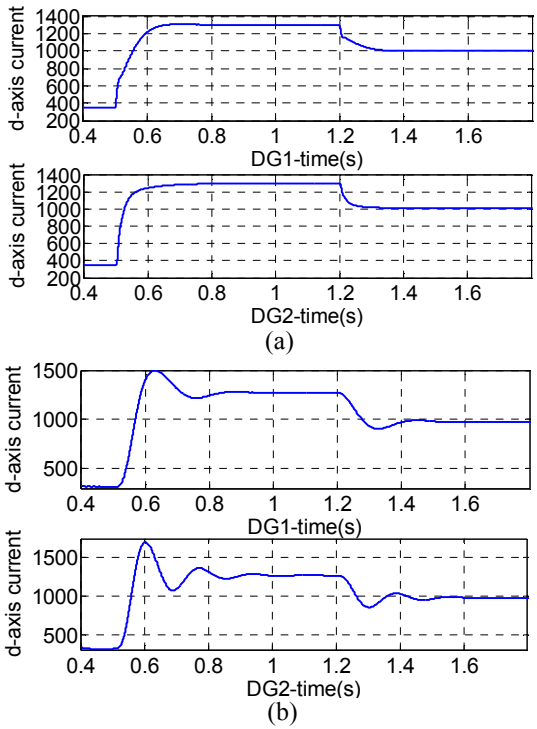

Figure 6-19. The simulation results for high and medium power applications, (a) the results for the multivariable synchronous-converter and (b) the results for the basic core controller.

with considerable overshoot. The overshoot in the system with core controller is increased to about 200 A. Also in the case $i_{dset1} = i_{dset2} = 1000\,\text{A}$ the steady state error is reduced from 2% in the core controller to 0.5% in the multivariable controller. Moreover, as it is seen the overshoot in the DG2 is significantly reduced which proves the ability of the multivariable controller to improve both transient and static performance.

6.7.2 Fault-Ride-Through-Capability: Line-to-Ground Fault

A line to ground fault occurs at the end of connecting line 2 of DG2 at t= 2.84 s and after 0.16 s the line is disconnected from the rest of the grid by action of breakers at its both ends. Since fault is cleared in less than 0.16 s the system is kept within ride-trough capability of the MG and there is no need for transition to

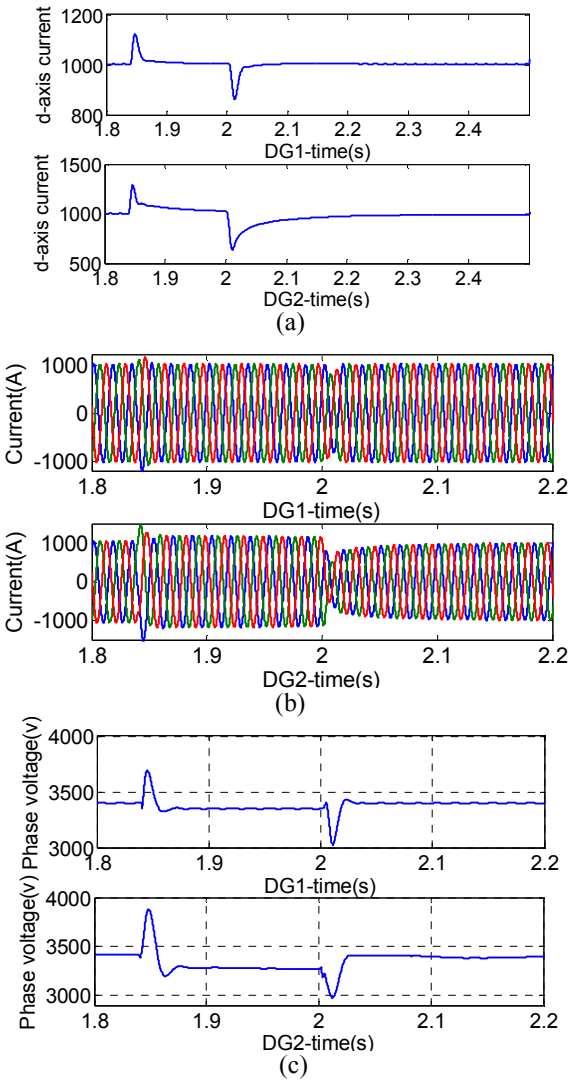

Figure 6-20. Fault ride through capability of the controller, (a) i_d (b) instantaneous current and (c) VSC phase voltage amplitude.

islanding. Fig. 6.20 shows the waveforms of i_d, phase voltage amplitude and current during these two transients. The current waveform reveals that the imposed current control limit restricts the current amplitude to the nominal value and after the disconnection of line 2, DG currents return to their initial values before the fault but in different operating point, i.e. different load angle. It should

be noted that subsequent to line disconnection, the grid strength becomes equal to the rated power of DG1 because the equivalent line impedance is doubled as a result of losing one line. The instantaneous current, i_d and voltage waveforms are fast and very smooth during both the contingencies and they settle down to their equilibrium points within 0.15 s. The local load voltage of DG2 amplitude undergoes a relatively large variation and is reduced from 3410 v to 3260 V subsequent to the fault which is still within the acceptable limits (less than 5%). Upon clearing the fault, the controller action returns the voltage to its normal range. The system performance in this case clearly confirms its robustness against large variation of connecting impedance and operating point.

6.7.3 Disturbance in the Grid and Faulted Line Restoration

To evaluate controller ability to track variations and disturbances in the grid, it is assumed that grid's angle is abruptly reduced by 20^o. From the waveforms of i_d, i_q and frequency shown in Fig. 6.21, it is concluded the controller is capable to synchronize itself with the gird without a need for a PLL. This is a result of the existence of synchronizing and damping current produced by the controller and in fact, the controller acts like a virtual PLL. The disturbance causes that i_{d2} undergoes a sudden jump of 205 A and a maximum of 3.5 rad/s angular frequency sag occurs. The plot of i_q in the interval of 1.5 to 4 s is shown in Fig. 6.21 (b). It is observed that effect of grid angle disturbance, which occurred at t= 2.5 s, on i_q is almost negligible which confirms good decoupling between d- and q-axis currents. However, at t=3 s, i_q encounters a large variation due to line impedance variation. Also, during the fault the amplitude of i_q is significantly increased. After 1 s of disconnection of line 2, the re-closer attempts to reconnect it to the grid. It is assumed that the fault has been cleared before the line reconnection, thus the reclosing is successful. In this case, system encounters a sudden change

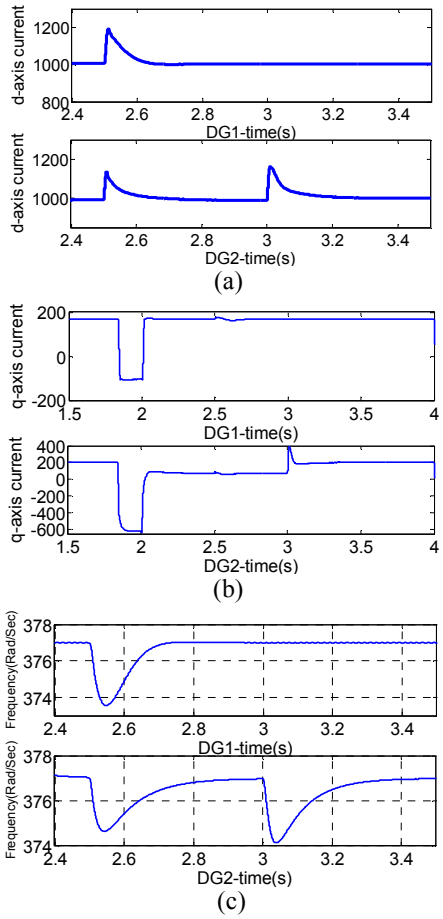

Figure 6-21. Results for the case of disturbance in the grid, (a) i_d (b) i_q and (c) frequency.

in the grid impedance; however, the proposed controller shows robust performance with damped transient response that settles down in less than 0.3 s.

6.7.4 Transition to Islanding and Islanded Operation

For this scenario, it is assumed that the MG is separated from the utility grid at t=4 s accidentally and an islanded MG is formed. Fig, 6.22 shows the performance of the system in terms of transition from grid connected mode to islanding mode. In grid connected mode, the DG units generates their preset d-axis currents whereas subsequent to islanding they are responsible to supply the

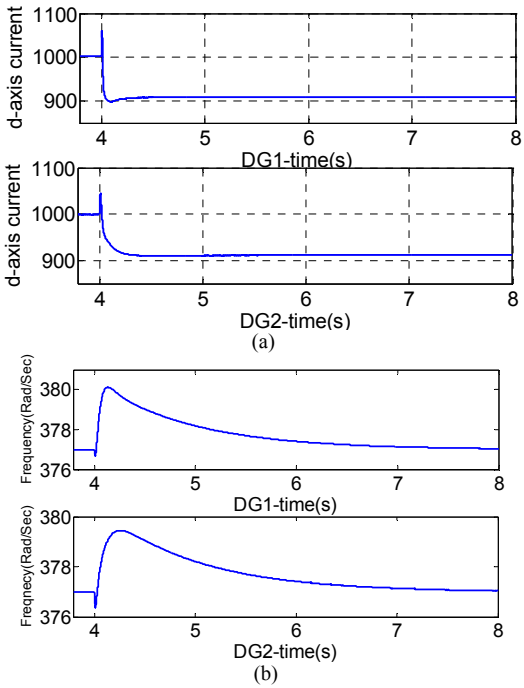

Figure 6-22. Transition to islanding, (a) i_d and (b) frequency.

local and common loads power and share the total MG current demand among themselves according to their capacities. There is no islanding detection process and since the topology is the same for both islanding and grid connected modes, the need for controller reconfiguration is eliminated. The current sharing capability is inherently embedded within the controller according to (6.59) and (6.64). Fig 6.22 shows that the proposed current control strategy, due to its fast response, results in satisfactory stability and transient performance during switching to islanding and permits a transition without load shedding. The generated d-axis currents of DG1 and DG2 are equal to 890 A and 885 A representing an error in current sharing of less than 0.4%, therefore both static and dynamic performance in islanded mode are satisfactory. This is in spite of the facts that connecting lines of DG units have unequal impedances, and both are very weak and resistive which is the worst scenario for current sharing. The

frequencies of the two DGs experience a frequency jump of 0.5 Hz in the interval of transition to islanding while the settling time is about 2 s. As shown, the steady state frequency in islanded mode is 60 Hz which is one of the main benefits of the controller. Actually, the controller presents accurate current sharing with steady state constant frequency operation resulting in high power and frequency quality.

Chapter 7 Conclusions and Future Work

7.1 Thesis Conclusions

Smart power grids are facing severe challenging problems in terms of control, management, stability and regulation. One of major origins of instabilities is fast development of voltage source converters (VSCs) due to deep penetration of renewable energy resources and their interactions with conventional synchronous generators (SGs) and loads which may significantly degrade smart power system performance. One approach to manage smart grids and attenuate negative effects of VSCs is to group a cluster of distributed generation (DG) units and renewable energy resources as some microgrids and coordinate them to achieve grid's supervisory objectives. This thesis has addressed these challenges by introducing a comprehensive new family of control and management strategies which establish the foundations for the control of future smart grids. The controllers realize many requirements of microgrids requirements in both operational modes without a need for reconfiguration, such as mimicking (SGs), seamless transition to islanding, grid self-synchronization, application to weak grids, large signal stability and superior decoupling.

In Chapter 2, a new family of power management controllers was proposed for grid connected and islanded MGs in the smart distribution system environment. The controllers are flexible for all operating conditions without need for reconfiguration which can realize the "plug-and-play" concept and overcome difficulties due to islanding detection. The power manager adopts cascaded hybrid frequency and angle droop loops so it benefits from advantages of both schemes. The angle and frequency loops realize power sharing in the autonomous mode

while they present damping and synchronizing power in a grid connected MG. There is an extra power loop within the controller emulating dynamic behaviour of a synchronous generator rotor and presents some dynamics for the frequency. Various topologies including power drooping voltage-controlled, power drooping current-controlled and current drooping voltage controlled are proposed and their characteristics have been investigated. It was shown that stable operation, accurate power sharing and steady-state rated frequency operation can be achieved by the proposed controller. Some structures for reactive power management and voltage control of DGs were also developed enabling DG units to either work as P-V bus or share reactive power. A theoretical analysis and simulation results validate the effectiveness of the proposed controllers under various operating conditions.

In Chapter 3, a novel control topology for VSCs has been developed in the frequency-angle domain to regulate the dc-link voltage while providing 1) synchronizing and damping power components; and 3) emulated inertia function to the VSC. These features are highly desirable in VSCs interfacing renewable energy resources, dc MGs and active converter-interfaced loads to weak ac systems. The proposed synchronous control topology offers the following advantages; 1) it is a new control topology implemented in the frequency-angle domain, which simplifies converter integration and analysis in grids with conventional SGs. 2) The controller introduces some inertia and dynamics for frequency. In fact, the power grid views the dc-link capacitor as a virtual rotor with virtual inertia. The stored energy in the dc-link is employed to damp frequency oscillations during contingencies. 3) Since the controller presents damping and synchronizing power dynamics, similar to SMs, it can automatically synchronize itself with the grid and tracks its variations, thus there is no need for a PLL after initial synchronization. 5) During modeling and design process, the dc-link voltage dynamics are taken into account which provides a more general and accurate control framework. 6)

The controller offers fault-ride-through capability which enhances the overall system reliability. Both simulation and experimental results have been provided to validate controller performance in a wide range of typical operating conditions.

In Chapter 4, a comprehensive and general power management/control strategy for both converter- and synchronous machines-based DG units in islanded and grid-connected MGs has been developed in this chapter. The proposed combined angle-frequency droop control can fulfill accurate power sharing, constant nominal-frequency operation at steady-state and stable performance in a wide range of operating conditions. However, in large sudden contingencies such as connection and disconnection of DG units and out-of-phase closing, using a linear controller cannot ensure stable MG operation. To overcome this problem and guarantee large-signal stability of the MG, a nonlinear supplementary controller has been developed for the linear droop control. The adaptive back-stepping technique has been employed to design the nonlinear controller and overcome modeling uncertainties. The effectiveness of the proposed controller is evaluated by simulation results under typical MG operating conditions.

In Chapter 5, a flexible control method for islanded and grid connected MGs with enhanced stability has been presented in this chapter. The control structure does not require reconfiguration upon islanding detection. Further, it involves a nonlinear MG stabilizer that guarantees large-signal stability of the MG system. The AB method has been adopted to design the augmented converter controller with MG stabilizer. The nonlinear MG stabilizer adds a supplementary signal to the voltage loop of the VSC so that the augmented system stability is guaranteed. The controller uses only local information where the need for communication is eliminated, and better reliability is yielded. The controller works in the angle, frequency and power domain instead of the conventional current-voltage controllers. It has been shown that using the proposed control scheme, the system is stable over a wide range of operation with minimum transients. Two different

virtual flux control strategies have been presented. Theoretical analysis and evaluation results have indicated that the proposed control strategy gives stable and flexible operation of DG MGs, and accordingly it contributes to increasing the safe penetration limit of DG in future smart power grids.

In Chapter 6, in the first section, a new control topology is presented to enable effective integration of VSCs to weak grids. The controller has two parts, namely a linear power damping controller and nonlinear supplementary controller. The linear part mimics SGs with extra power damping-synchronization capability providing self-synchronization with grid in steady-state which eliminates the need for a PLL. However, in grid restoration scenarios, any large mismatch between VSC and grid frequency and angle may cause poor performance and even instability. These cases are considered as large-signal disturbances, thus proposed nonlinear controller can enhance system performance in these cases. Moreover, the controller is able to work in very weak grids with $SCR<2$ and supplies the rated power because of its damping and synchronizing power characteristics. The design process for the linear and nonlinear parts has been presented and numerous simulation scenarios were presented to validate the controller effectiveness.

In the second section, a multivariable control topology for grid-connected and isolated weak MGs, using the concept of multivariable synchronous-converter, is presented. The controller provides universal strategy for both grid-connected and islanded MGs. DG units generates the reference current in grid-connected mode and share the total current demand during islanding. It is also a good candidate to interface converter-based DG units to very weak MGs and enables the operation of VSCs in grids with SCR less than 2. The multivariable controller decouples the d- and q-axis currents which in turn results in very high performance steady-state and transient operation with low steady-state error and fast response in weak grids where d- and q-axis currents are highly coupled due to operation at high-load angles. One of its salient features is that it mimics the behaviour of synchronous

generators and introduces some inertia for frequency dynamics; therefore it can be called a multivariable synchronous converter. Moreover, the current sharing is obtained with constant frequency operation. Another major advantage of the controller is eliminating the PLL during steady state because it produces internal synchronizing and damping currents and also the frequency is internally available; i.e., the VSC automatically synchronizes itself with the grid and track its variations.

Finally, a design guideline and benchmark is given to compare and select optimum controller topology for different applications. In chapter 2 a new family of controller topologies was developed. They are suitable for both operational modes with seamless transition to islanding. Both power droop and current droop methods are available. Also, the proposed family of controllers enables current controlled (model-b and model-c) and voltage controlled-VSC are applicable, where model-c enables current management, control and limitation in one compact structure with very fast response which makes it the best candidate for microgrid. However, *synchronous converter*s cannot fulfill dc-link regulation so they are not proper choices for rectifying mode and dc microgrids. Toward this, the synchronous-VSC strategy can be employed to regulate the dc-link voltage and have it constant. It is also possible to inject a specific power to the grid with regulated, but not constant, dc-link voltage. The main drawback is that ac side power sharing capability is missed during islanding therefore it is mainly for a grid connected VSC. The cooperative angle-frequency droop, presented in chapter 4, provides a plug-and-play MG with large signal stability in a wide range of operating points with self-synchronization capability. In large signal disturbances, the proposed linear controllers in chapter 2 fall short to guarantee system smooth performance. Weak grids are another challenging issue in smart grids. In weak grids, the load angle is large and drifts to the nonlinear region, so system is prone to instability. The nonlinear power damping controller is used to integrate VSCs

to very weak with *SCR*=1 grids with self-synchronization ability and guaranteed stability. Beside poor performance and low stability, weak MGs suffer from high coupling between d- and q-axis currents and also real and reactive powers. Although, the nonlinear power damping controller is successful in stable performance of weak grids, the superior decoupling is not achievable by this controller. Therefore, a multivariable droop synchronous converter is proposed which aims at reducing the steady state error and decoupling between d- and q-axis currents. However, it cannot realize large signal stability and self-synchronization. Therefore, if the goal is to achieve satisfactory static and dynamic performance with minimum steady state error and transients, multivariable droop synchronous converter is the optimal choice.

7.2 Suggestions for Future Works

Finally, the following directions are proposed to extend the work presented in this thesis:

- Although VSCs are the dominant technology for interfacing DG, HVDC and other electronically-interfaced (EI) units, current-source converters (CSCs) are becoming more and more important, especially for integration of PV systems, because of their ability to provide smooth current, short-circuit protection and fault-ride trough capability. Similar to VSCs, vector control is the common adopted control method for the CSCs which may cause serious instability issues due to interaction with SGs, VSCs, and EI-interfaced units. Toward this, concept of synchronous current converter (*synchronous-CSC*) can be developed in a continuation of the *synchronous-VSC* and *synchronous converter* to achieve a unified and seamless control and management strategy for SGs, VSCs and CSCs in smart grids. The concept of *synchronous-CSC* offers some advantages

over the *synchronous-VSC* as the dc-link inductor stores more energy as compared to a VSC with similar size.

- The focus of the thesis was on control and management of ac microgrids in both grid-connected and islanded modes. However, a major portion of EI-interfaced loads and generation units such as PV are dc type, therefore, dc and hybrid dc/ac microgrids are gaining high momentum n the context of smart grids. An interesting research area to work is the application of synchronous-VSC and synchronous converters to these microgrids and study their characteristics.

  With the developed controllers, future researches could study and characterize effect of nonlinear loads on the control performance and establish a general methodology for harmonic current sharing and elimination. Moreover, the impedance model of the proposed controllers can be investigated and some active damping techniques similar to the vector control can be developed to attenuate instabilities that may be resulted from interaction with static and dynamic loads and also output filter.

- In chapter 6 two separate controllers, namely nonlinear power damping and multivariable synchronous converter are proposed for the integration of VSCs to weak grids. However, they cannot fulfill superior decoupling and large-signal-stability simultaneously. For future work, it is possible to develop a combined multivariable nonlinear controller using adaptive back-stepping. Further, the controllers can be easily made robust against system uncertainties by techniques like singular values. Also, as shown in chapter 6, the design of the multivariable controller is highly dependent on a given operating point; therefore the controller cannot guarantee decoupling in a wide range of operating conditions. Thus, an adaptive

multivariable with variable parameters can be adopted to overcome this difficulty.

- The proposed controllers are feasible to both rectifiers and inverters. Therefore, application of synchronous-VSC and synchronous converter to back-to-back converters such as HVDC links and wind turbines is another appealing work especially when they are connected to weak grids.

Bibliography

[1] A. Molderink, V. Bakker, M.G.C. Bosman, J.L. Hurink, "Management and control of domestic smart grid technology," *IEEE Trans. Smart Grid*, vol. 1, no 2, pp.109-118, Sep. 2010.

[2] S. Stanley, A. G. Phadke and B. A. Renz, "The future of power transmission," *IEEE Power & Energy Magazine*, vol. 8, no. 2, pp.34-40, March/ April 2010.

[3] E. Santacana. G. Rackliffe, L. Tang and X. Feng, "Getting smart," *IEEE Power &Energy Magazine*, Vol. 8, No. 2, pp.41-48, March/ April 2010.

[4] J. Guerrero et al, "Distributed generation," *IEEE Ind. Electr. Mag.* , pp. 52-64, March 2010.

[5] Y.A.-R.I. Mohamed and E.F. El-Saadany, "Adaptive decentralized droop controller to preserve power sharing stability of paralleled inverters in distributed generation microgrids," *IEEE Trans. Power Electr.* , vol. 23, no. 26, pp. 2806-2816, Nov. 2008.

[6] B. Kroposki, R. DeBlasio, and M. Simoes, "Benefits of power electronic interfaces for distributed energy systems," *IEEE Trans. Energy Conv.,* Vol. 25, No. 3, pp. 901-908, Sep. 2010.

[7] S. Bifaretti, P. Zanchetta, A. Watson, L. Tarisciotti, J.C. Clare, "Advanced power electronic conversion and control system for universal and flexible power management," *IEEE Trans. Smart Grid*, vol.2, no 2, pp. 231-243, June, 2011.

[8] P. Tenti, H.K. M. Paredes and P. Matavvelli, "Conservative power theory, a framework to approach control and accountability issues in smart microgrids," *IEEE Trans. Power Electr*., vol. 26, no. 3, pp. 664- 673, March 2011.

[9] "IEEE guide for design, operation, and integration of distributed resource island systems with electric power Systems," *IEEE Std 1547.4-2011*, pp.1-54, July 20 2011.

[10] F. Katiraei, and M.R. Iravani, "Power management strategies for a microgrid with multiple distributed generation units," *IEEE Trans. Power Sys.* vol. 21, no. 4, pp. 1821-1831, Nov. 2006.

[11] J. A. P. Lopez, C. L. Moreira, and C. Marnay, "Defining control strategies for microgrids islanded operation," *IEEE Trans. Power Syst*., vol. 21, no. 2, pp. 916-924, May 2006.

[12] Il-Yop Chung, L. Wenxin, D.A. Cartes, E.G. Collins, "Control methods of inverter-interfaced distributed generators in a microgrid system," *IEEE Trans. Ind. Appli*., pp. 1078-1088, May/June, 2010.

[13] V. C. Gungor, B. Lu and G. P. Hancke, "Opportunities and challenges of wireless sensor networks in smart grid- a case study of link quality assessments in power distribution systems," *IEEE Trans. Ind. Electr*. vol. 57, no. 10, pp. 3557-3564, Oct. 2010.

[14] M. Prodanovic, and T.C. Green, "High-quality power generation through distributed control of a power park microgrid," *IEEE Trans. Ind. Electr*. vol. 53, no. 5, pp. 1471-1481, Oct. 2006.
[15] J.M. Guerrero, L. Garcia De Vicuna, J. Matas, M. Castilla, J. Miret, "A wireless controller to enhance dynamic performance of parallel inverters in distributed generation systems," *IEEE Trans. Power Electr*. vol. 19, no. 5, pp. 1205-1213, Sep. 2004.
[16] J. Guerrero, J. Matas, L. G. D. Vcuna and J. Miret, "Wireless-control strategy for parallel operation of distributed-generation inverters," *IEEE Trans. Ind. Electr*. Vol. 53, No. 5, pp.1461- 1470, Oct. 2006.
[17] K.D. Brabandes *et al*, "A voltage and frequency droop control method for parallel inverters," *IEEE Trans. Power Electr*. vol. 22, no. 4, pp.1107-1114, July, 2007.
[18] E. Barklund, N. Pogaku, M. Prodanovic, C. Hernandez-Aramburo, T.C. Green, "Energy management in autonomous microgrid using stability-constranted droop control of inverters," *IEEE Trans. Power Elecr*., vol. 23, no. 5, Sep. 2008.
[19] J.C. Vasquez, J.M. Guerrero, A. Luna, P. Rodriguez, R. Teodorescu, "Adaptive droop control applied to voltage-source inverters operation in grdi-connected and islanded modes," *IEEE Trans. Ind. Electr*. vol. 56, no.10, pp.4088-4096, Oct. 2009.
[20] Y.W. Li and C. Kao, "An accurate power control strategy for power-electronic-interfaced distributed generation units operation in a low-voltage multibus microgrid," *IEEE Trans. Power Electr*., vol. 24, no. 12, 2977-2988, Dec. 2009.
[21] Y.W. Li, "Power management of inverter interfaced autonomous microgrid based on virtual frequency-voltage frame," *IEEE Trans. Smart Grid*, vol. 2, no 1, pp.30-40, March 2011.
[22] E. Rokrok and M.E.H. Golshan, "Adaptive voltage droop for source converters in an islanded multibus microgrid," *IET Generation, Trans. & distr.*, vol. 4, no. 5, pp. 562-578, 2010.
[23] J. Guerrero, J.C. Vasquez, L.G. D. Vicuna, "Hierarchical control of droop-controlled AC and DC microgrids-A general approach toward standardization," *IEEE Trans. Ind. Electr*., vol. 58, no.1, pp.158-166, Jan. 2011.
[24] Seon-Ju Ahn, Jin-woo Park, Il-Yop Chung, Seung-Il Moon, Sang-Hee Kang, Soon-Ryul Nam , "Power-sharing method of multiple distributed generators considering modes and configurations of a microgrid," *IEEE Trans. Power Del.,* vol. 25, no. 3, pp.2007-2016, July 2010.
[25] D. De and V. Ramanarayanan, "Decentralized parallel operation of inverters sharing unbalanced and nonlinear loads," *IEEE Trans. Power Electr.,* vol. 25, no. 12, pp. 3015-3022, Dec. 2010.

[26] W. Yao, J. Matas, J. M. Guerrero and Z.M. Qian, "Design and analysis of the droop control method for inverters considering the impact of the complex impedance on the power sharing," *IEEE Trans. Ind. Electr*., vol. 58, no. 2, pp. 576-587, Feb. 2011.

[27] H. Nikkhajoei and R.H. Lasseter, "Distributed generation interface to the CERTS microgrid," *IEEE Trans. Power Del.,* vol. 24, no. 3, pp. 1598-1608, July 2009.

[28] R. Majumder, G. Ledwich, A. Ghosh, S. Chakrabarti, F. Zare, "Droop control of converter interfaced microsources in rural distributed generation," *IEEE Trans. Power Del.,* vol. 25, No. 4, pp.2768-1778, Oct. 2010.

[29] F. Gao and M.R. Iravani, "A control strategy for a distributed generation unit in grid-connected and autonomous modes of operation," *IEEE Trans. Power Del.*, vol. 23, no. 2, pp.850-858, Apr. 2008.

[30] I.J. Balaguer, L. Qin, Y. Shuitao, U. Supatti, Fang Zheng , "Control for grid-connected and intentional islanding operation of distributed power generation," *IEEE Trans. Ind. Electr*., vol. 58, no. 1, pp.147-156, Jan. 2011.

[31] F. Katiraei, M. R. Iravani and P.W. Lehn, "Micro-grid autonomous operation and subsequent to islanding process," *IEEE Trans. Power Del.*, vol. 20, no. 1, pp.248-257, Jan. 2005.

[32] H. Karimi, H. Nikkhajoei and M.R. Iravani, "Control of an electronically-coupled distributed resource unit subsequent to an islanding event," *IEEE Trans. Power Del.*, vol. 23, no. 1, pp.493-501, Jan. 2008.

[33] C. Linang Chen et al, "Design of parallel inverters for smooth mode transfer microgrid applications," *IEEE Trans. Power Electr.,* vol. 25, no. 1, pp.6-15, Jan. 2010.

[34] Y.A.-R. I. Mohamed and A.A. Radwan, "Hierarchical control system for robust microgrid operation and seamless mode transfer in active distribution systems," *IEEE Trans. Smart Grid*, vol. 2, no. 2, pp.352-362, June, 2010.

[35] L. Zang, L. Harnefors, and H.-P. Nee, "Power-synchronization control of grid-connected voltage source converters," *IEEE Trans. Power Sys.,* vol. 25, no. 2, pp. 809-820, May 2010.

[36] H. Harnefors, M. Bongiornos, and S. Lundberg, "Input-admittance calculation and shaping for controlled voltage source converters," *IEEE Trans. Ind. Electr.,* vol. 54, no. 6, pp.3323-3334, Dec. 2007.

[37] J. Rocabert, A. Luna, F. Blaabjerg, and P. Rodriguez, "Control of power converters in AC microgrids," *IEEE Trans. Power Electr*., vol. 27, no. 11, pp. 4734-47-49, Nov. 2012.

[38] A.A.A. Radwan and Y. A. –R. I. Mohamed, "Linear active stabilization of converter-dominated dc microgrids," *IEEE Trans. Smart Grid*, vol. 3, no. 1, pp. 203-216, March 2012.

[39] ECPE European Center for Power Electronics, "Strategic research agenda on intelligent power electronics for energy efficiency," Jan. 2008.

[40] R. Majumder *et al*, "Improvement of stability and load sharing in an autonomous microgrid using supplementary droop control loop," *IEEE Trans. Power Sys.*, vol. 25, no. 2, May 2010.

[41] R. Majumder, A. Ghosh, G. Ledwich, F. Zare, "Angle droop versus frequency droop in a voltage source converter based autonomous microgrid," *IEEE Power & Energy Society General Meeting*, 2009.

[42] A. Bidram and A. Davoudi, "Hierarchical structure of microgrids control systems," *IEEE Trans. Smart Grid*, vol. 3, no 4. pp. 1963-1976, Dec, 2012.

[43] Y. Li and Y. W. Li, "Power management of inverter interfaced autonomous microgrid based on virtual frequency-voltage frame," *IEEE Trans. Smart Grid*, vol. 2, no. 1, pp. 30–40, Mar. 2011.

[44] J. M. Guerrero *et al*, "Decentralized control for parallel operation of distributed generation inverters using resistive output impedance," *IEEE Trans. Ind. Elctr.*, vol. 54, no. 2, pp. 994-1004, Apr. 2007.

[45] K. D. Brabandere, B. Bolsens, J. V. D. Keybus, A. Woyte, and J. Driesen, "A voltage and frequency droop control method for parallel inverters," *IEEE Trans. Power Electron.*, vol. 22, pp. 1107–1115, Jul. 2007.

[46] J. Driesen and K. Visscher, "Virtual synchronous generators," *IEEE Power and Energy Society General Meeting-Conversion and Delivery of Electrical Energy in the 21st Century*, 2008.

[47] K. Vischer and S. W. H. De Haan, "Virtual synchronous machines (VSG's) for frequency stabilization in future grids with a significant share of decentralized generation," *in Proc. IET. CIRED, Smart Grid for Distribution, 2008.*

[48] M. F. M. Arani, and E. F. El-Saadani, "Implementing virtual inertia in DFIG-based wind power generation," *IEEE Trans. Power Sys.*, vol. 28, no. 2, pp. 1373-1384, 2013.

[49] J. Zhu, C. D. Booth, G. P. Adam, A. J. Roscoe, and C. G. Bright, "Inertia emulation control strategy for VSC-HVDC transmission systems," *IEEE Trans. Power Sys.*, vol. 28, no.2, pp. 1277-1287, 2013.

[50] Q. –C. Zhong and G. Weiss, "Synchronverters: inverters that mimic synchronous generators," *IEEE Trans. Ind. Electr.*, vol. 58, no. 4, pp. 1259-1267, Apr. 2011.

[51] M. Kayikci and J.V.Milanovic, "Dynamic contribution of DFIG-based wind plants to system frequency disturbances," *IEEE Trans. Power Syst.*, vol. 24, no. 2, pp. 859–867, May 2009.

[52] T. L.Vandoorn, B. Meersman, J.D.M De Kooning, and L.Vandevelde, "Analogy between conventional grid control and islanded microgrid control based on a global DC-link voltage droop," *IEEE Trans. Power Del*., vol. 27, no. 3, pp. 1405-1414, July 2012.

[53] T. L.Vandoorn, B. Meersman, J.D.M De Kooning, and L.Vandevelde, "Directly-coupled synchronous generators with converter behavior in islanded microgrids," *IEEE Trans. Power Syst.*, vol. 27, no. 3, pp.1395-1406, Aug. 2012.

[54] G. Beccuti, G. Popafotiou and L. Harnefors, "Multivariable optimal control of HVDC transmission links with network parameter estimation for weak grids," to appear in *IEEE Trans. Cont. Sys. Tech.* 2013.

[55] N. P. W. Strachan and D. Jovcic, "Stability of a variable-speed permanent magnet wind generator with weak AC grids," *IEEE Trans. Power Del*., vol. 25, no. 4, pp. 2779-2788, Oct. 2011.

[56] L. Zhang, L. Harnefors, and H.-P. Nee, "Interconnection of two very weak AC systems by VSC-HVDC links using power-synchronization control," *IEEE Trans. Power Sys*., vol. 26, no. 1, pp. 344-355, Feb. 2011.

[57] *IEEE Guide for planning DC Links Terminating at AC Locations Having Low Short-Circuit Capacities*, 1997, *IEEE Std. 1204-1997*, Tech. Rep.

[58] L. Zhang, L. Harnefors, and H. –P. Nee, "Power-synchronization control of grid-connected voltage-source converters," *IEEE Trans. Power Syst*., vol. 25, no. 2, pp. 809-819, May 2010.

[59] L. Zhang, L. Harnefors, and H.-P. Nee, "Modeling and control of VSC-HVDC links connected to island systems," *IEEE Trans. Power Syst*., vol. 26, no. 2, pp.783-793, May 2011.

[60] "*IEEE guide for design, operation, and integration of distributed resource island systems with electric power Systems*," *IEEE Std 1547.4-2011*, pp.1-54, July 20 2011.

[61] R. Majumder, A. Ghosh, G. Ledwich, F. Zare, "Power management and power flow control with back-to-back converters in a utility connected microgrid," *IEEE Trans. Power Syst*., vol. 25, no. 2, pp. 8821-834, 2010.

[62] T. L.Vandoorn, B. Meersman, J.D.M De Kooning, and L.Vandevelde, "Voltage-based control of a smart transformer in a microgrid," *IEEE Trans. Ind. Electron*., vol. 60, no. 4, pp. 1291-1305, Apr. 2013.

[63] M. P. Kazmierkowski and L. Malesani, "Current control techniques for three-phase voltage-source PWM converters: a survey," *IEEE Trans. Ind. Electr.*, vol. 45, no. 5, pp.691-703, Oct. 1998.

[64] H. Alatrash, A. Mensah, E. Mark, G. Haddad, and J. Enslin, "Generator emulation controls for photovoltaic inverters," *IEEE Trans. on Smart Grid*, vol.3, no.2, pp.996-1011, June 2012.

[65] N. Soni, S. Doolla and M. C. Chandorkar, "Improvement of transient response in microgrids using virtual inertia," *IEEE Trans. on Power Del.*, vol.28, no.3, pp.1830-1838, July 2013.

[66] M. Ashabani and Y. A. –R. I. Mohamed, "Novel comprehensive control framework for incorporating VSCs to smart power grids using bidirectional synchronous VSC," *IEEE Trans. Power Sys.*, vol. 29, no. 2, pp. 943-957, March 2014.

[67] C. H. Sao and P. Lehn, "Control and power management of converter fed microgrids," *IEEE Trans. Power Syst.*, vol. 23, pp. 1088-1098, Aug. 2008.

[68] C. K. Sao and W. Lehn, "Autonomous load sharing of voltage source converters," *IEEE Trans. Power Del.*, vol. 20, pp. 1009–1016, Apr. 2005.

[69] J. C. Vasquez, J. M. Guerrero, A. Luna, P. Rodriguez, and R. Teodorescu, "Adaptive droop control applied to voltage-source inverters operating in grid-connected and islanded modes," *IEEE Trans. Ind. Electron.*, vol. 56, pp. 4088–4096, Oct. 2009.

[70] W. Yao, M. Chen, J. Matas, J. M. Guerrero, and Z. Qian, "Design and analysis of the droop control method for parallel inverters considering the impact of the complex impedance on the power sharing," *IEEE Trans. Ind. Electron.*, vol. 58, pp. 576–588, Feb. 2011.

[71] J. M. Guerrero, L. G. D. Vicuna, J. Matas, M. Castilla, and J. Miret, "Output impedance design of parallel-connected UPS inverters with wireless load-sharing control," *IEEE Trans. Ind. Electron.*, vol. 52, pp. 1126–1135, Aug. 2005.

[72] J. M. Guerrero, L.Hang, J. Uceda, "Control of distributed uninterruptable power supply systems," *IEEE Trans. Ind. Electr*. Vol. 55, no. 8, pp. 2845-2859, Aug. 2008.

[73] M. B. Delghavi and A. Yazdani, "A unified control strategy for electronically interfaced distributed energy resources," *IEEE Power Del.*, vol. 27, no. 2, pp. 803-812, 2012.

[74] Q.-C. Zhong, "Robust droop controller for accurate proportional load sharing among inverters operated in parallel," *IEEE Trans. Ind. Electr.*, vol. 60, no.4, pp. 1281-1290, 2013.

[75] R. Majumder, "Power sharing and control in distributed generation with wireless sensor network," *IEEE Trans. Smart Grid*, vol. 3, no. 2, pp. 618-634, June 2012.

[76] P. H. Divshali, A. Alimardani, S. H. Hosseinian, and M. Abedi, "Decentralized cooperative control strategy of microsources for stabilizing autonomous VSC-based microgrids," *IEEE Trans. Power Syst*., vol. 27, no. 4, pp.1949-1959, Nov. 2012.

[77] R.S. Balog, W.W. Weaver, and P.T. Krein, "The load as an energy asset in a distributed DC smart grid architecture," *IEEE Trans. Smart Grid*, vol. 3, no. 1, pp. 253-260, Jan. 2012.

[78] N. R. Chaudhuri, R.Majumder, B. Chaudhuri, "System frequency support through multi-terminal DC (MTDC) grids," *IEEE Trans. Power Syst.*, vol. 28, no. 1, pp. 347-356, 2013.

[79] N. R. Chaudhuri, B. Chaudhuri, "Adaptive droop control for effective power sharing in multi-terminal DC (MTDC) grids," *IEEE Trans. Power Syst*., vol. 28, no. 1, pp. 21-29, 2013.

[80] Z. Ma, Q. –C. Zhong, and J.D. Yan, "Synchronverter-based control strategies for three-phase PWM rectifiers," *7th IEEE Conference on Industrial Electronics and Applications (ICIEA),* 2011, Singapore.

[81] N. Pogaku, M. Prodanovic, and T. C. Green, "Modeling, analysis and testing of autonomous operation of an inverter-based microgrid," *IEEE Trans. Power Electr.*, Vol. 22, No. 2, pp.613-625, Apr. 2007.

[82] M. A. Rahman, D. M. Vilathgamuwa, M.N. Uddin, K. Tseng, "Nonlinear control of interior permanent-magnet synchronous motor," *IEEE Trans. Ind. Appli*., vol. 39, no. 2, pp. 408-416, March/April, 2003.

[83] A. Karimi and A. Feliachi, "Decentralized extended-backstepping control of power systems," *2006 POWER ENG. SOC. GEN. MEETING*, pp.611-618, Montreal, CANADA.

[84] R. Yan et al, "Power system transient stability enhancement with an adaptive control scheme using backstepping design," *2007 IEEE POWER ENG. SOC. GEN. MEETING*, pp.1070-1077, Tampa, FL.

[85] A. Karimi and A. Feliachi, "Decentralized adaptive backstepping of electric power systems," *Elec. Power Sys. Res*., vol. 78, no. 3, pp.484-493, 2008.

[86] R. Yan, Z.Y. Dong, T.K. Saha and R. Majumder, "A power system nonlinear adaptive decentralized controller design," *Automatica*, vol. 46, no. 2, pp. 330-336, 2010.

[87] D.E. Kim and D. Lee, "Feedback linearization control of three-phase UPS inverter system," *IEEE Trans. Ind. Electr.*, vol. 57, no. 3, pp. 963-971, March 2010.

[88] S. Rahmani, N. Mendalek and K. Al-Haddad, "Experimental design of a nonlinear control technique for three-phase shunt active power filter," *IEEE Trans. Ind. Electr*., vol. 57, no. 10, pp.3364-3357, Oct. 2010.
[89] E. Song, A.F. Lynch, and V. Dinavahi, "Experimental Validation of Nonlinear Control for a Voltage Source Converter*," IEEE Trans. Cont. Sys. Tech.,* vol. 17, no. 5, pp.1135-1144, 2009.
[90] R. Yazdanpanah, J. Soltani, and G.R. A. Markadeh, "Nonlinear torque and stator flux controller for induction motor drive based on adaptive input–output feedback linearization and sliding mode control," *Enrergy Conv. And Manag*., vol. 49, no. 4, pp.541-550, Apr. 2008.
[91] B. Lu and B.T. Ooi, "Nonlinear control of voltage-source converter systems," *IEEE Trans. Power Electr*., vol. 22, no. 4, pp. 1186-1195, July, 2007.
[92] L. Yacoubi, K. Al-Haddad, L.A. Dessaint, F. Fnaiech, "Linear and nonlinear control techniques for a three-phase three-level NPC controller," *IEEE Trans. Ind. Electr*., vol. 53, no. 6, Dec. 2006.
[93] M. Zhixin, F. Lingling, D. Osborn, and S. Yuvarajan, "Wind farms with HVDC delivery in inertial response and primary frequency control," *IEEE Trans. Energy Convers*., vol. 25, no. 4, pp. 1171-1178, Dec. 2010.
[94] H. Karimi, E. J. Davison, and R. Iravani, "Multivariable servomechanism controller for autonomous operation of a distributed generation unit: design and performance evaluation," *IEEE Trans*. *Power Sys*., vol. 25, no. 2, pp. 853-865, May 2010.
[95] B. Bahrani, S. Kenzelman, and A. Rufer, "Multivariable-PI-based current control of voltage source converters with superior dq axis decoupling capability," *IEEE Trans. Ind. Elctr*., vol. 58, no.7, pp. 3016-3026, July 2011.
[96] B. Bahrani, A. Karimi, B. Ray, and A. Rufer, "Decoupled dq-current control of grid-tied voltage source converters using nonparametric models," to appear in *IEEE Trans. Ind. Electr.*, 2013.
[97] A. Tabesh and R. Iravani, "Multivariable dynamic model and robust control of a voltage-source converter for power system applications," *IEEE Trans. Power Del*., vol. 24, no. 1, pp. 462-471, Jan. 2009.
[98] L. Zhang, and Hans-Peter, "Multivariable feedback design of VSC-HVDC connected to weak AC systems," in *Proc. Power Tech. Conference*, 2009.
[99] F. Blaabjerg, R. Teodorescu, M. Liserre, and A. V. Timbus "Overview of control and grid synchronization for distributed power generation systems," *IEEE Trans. Ind. Electr*., vol. 53, no. 5, pp.1398-1408, Oct. 2006.
[100] Q. –C. Zhong, P. –L. Nguyen, Z. Ma, W. Sheng, "Self-synchronized synchronverters: inverters without a dedicated synchronization unit," *IEEE Trans. Power Elctr*., vol. 29, no. 2, pp. 617-630, 2014.
[101] M. Ashabani and Y. A. –R. I. Mohamed, "New family of microgrid control and management strategies in smart distributed grids- analysis,

comparison and testing," accepted for publication in *IEEE Trans. Power Syst*., 2014.

[102] Florian Dörf er and Francesco Bullo, "Kron reduction of graphs with applications to electrical networks," *IEEE Trans. Circ. and Syt.—I,* vol. 60, no. 1, pp. 150-163, Jan. 2013.

[103] P. Kundur, Power system stability and control, McGraw-Hill, 1994.

[104] S. M. Ashabani and Y. A. –R. I. Mohamed, "General interface for power management of micro-grids using cooperative droop control," *IEEE Trans. Power Syst*., vol. 28, no. 3, pp. 2929-2941, Aug. 2013.

[105] M. Hamzeh, H. Karimi, and H. Mokhtari, "A New Control Strategy for a Multi-Bus MV Microgrid Under Unbalanced Conditions," *IEEE Trans. Power Sys*., vol. 27, no. 4, pp.2225-2232, Nov. 2012.

[106] A. Mehrizi-Sani and R. Iravani, "Online Set Point Adjustment for Trajectory Shaping in Microgrid Applications," *IEEE Trans. Power Sys.,* vol. 27, no. 1, pp. 216-223, Feb. 2012.

[107] S. M. Ashabani and Y. A. -R. I. Mohamed, "A flexible control strategy for grid-connected and islanded microgrids with enhanced stability using nonlinear microgrid stabilizer," *IEEE Trans. Smart Grid*, vol. 3, no. 3, pp. 1291-1301, Sep. 2012.

[108] Y. Wang, G. Guo and D. J. Hill, "Robust decentralized nonlinear controller design for multimachine power systems," *Automatica*, vol. 33, no. 9, pp. 1725-1733, 1997.

[109] M. Ashabani and Y. A. –R. I. Mohamed, "Integrating VSCs to weak grids by nonlinear power damping controller with self-synchronization capability," *IEEE Trans. Power Syst*., vol. 29, no. 2, pp. 805-814, March, 2014.

[110] M. Ashabani and Y. A. –R. I. Mohamed, "Hybrid-variable droop control of synchronous converters in weak grids with decoupled dq-axis," submitted to *IEEE Trans. Smart Grid*, 2014.

[111] S. Zhen-Yin, Z. Xin, and W. Li-Ping, "The control algorithm for a photovoltaic inverter be applied in weak power grid," The 6th international conference on computer science & education (ICCSE 2011), Singapore.

[112] L. Zhang, L. Harnefors, and H.-P. Nee, "Analysis of stability limitations of a VSC–HVDC link using power-synchronization control," *IEEE Trans. Power Sys.,* vol. 26, no. 3, pp.1326-1336., Aug. 2011.

[113] G. Weiss, Q. –C. Zhong, T. C. Green, and Jun Liang, "H^{∞} repetitive control of DC-AC converters in microgrids," *IEEE Trans. Power Electr*., vol. 1, no. 1, pp. 219-224, Jan., 2004.